Dynamic Balance of Forces in Dusty (Complex) Plasmas

Dissertation
zur Erlangung des Doktorgrades
der Mathematisch-Naturwissenschaftlichen Fakultät
der Christian-Albrechts-Universität zu Kiel

vorgelegt von
Ciprian Zafiu

Kiel
September 2002

Contents

1 Introduction

Starting with the establishment of the laws of dynamics, the behavior of dynamical systems has been defined in terms of forces and force equilibria. In dusty plasmas, as systems where nanometer to micrometer-size particles interact with the plasma environment, the particle motion gives crucial information on the interactions of the dust particles with each other and with the surrounding plasma.

After the discovery of plasma crystals in 1994 [1, 2, 3, 4], dusty plasmas have exhibited a spectacular and explosive evolution among the other research fields in plasma physics. The progress in complex plasma research has exceeded the most optimistic expectations and estimations.

Until 1994 the dusty plasma research, introduced as concept by the study of astrophysical phenomena [5, 6, 7, 8, 9] like comet tails and Saturn rings, has experienced a mostly theoretical development. Later, technological applications in microelectronic industry [10, 11, 12, 12, 13, 14] have been developed, where particles unintentionally grown in the processing installations pose a serious problem of contamination. Further applications have been achieved in the new material technology, such as the production of ultra-fine ceramics [15, 16], amorphous silicon solar cells with a higher efficiency [17], or ultra-hard and self-lubricating thin films. Also in the astrophysics, they represent an important approach in understanding phenomena such as planet formation, planetary rings [18, 7, 19, 20], and noctilucent clouds in the summer polar mesosphere [21].

In the laboratory, micrometer-sized particles are trapped in the plasma sheath above an electrode where the gravitation force is balanced by the electric field force. Here, the particles form regular structures when a weak confinement force is applied. The most interesting are dusty plasmas in a strongly coupled regime, the so called "plasma crystals", which have been extensively studied.

The charge to mass ratio of the microparticles is much smaller than that of ions. Therefore all the dynamical processes occur at a very accessible time and space scale. Micrometer sized particles can be easily observed with videomicroscopy technique or even macrolenses. This allows the observation of individual particles using standard video technique. Therefore, the weak damping of processes in dusty plasmas makes them more suitable systems for the study of dynamic processes compared to similar systems like colloidal suspensions [22, 23, 24, 25, 26, 27, 28, 29, 30], and the diagnostic methods are much simpler than those for ions in Paul or Penning traps [31, 32, 33, 34, 35].

Dusty plasmas combine the properties of the microscopic plasma components

(electrons, ions and neutrals) with those of macroscopic matter particles. These exceptional properties allow the investigation of a multitude of dynamic phenomena such as phase transitions in plasma crystals [1, 36, 37, 38, 39], waves [40, 41, 42, 43, 44, 45, 46, 47, 48], Mach cones [43, 49, 50, 51, 52], and oscillations [53, 54, 55, 56, 57], [A.1]. All these phenomena are determined by the balance of various forces acting on the particles in these strongly coupled systems.

A novel experimental approach is the installation of experiments in space, onboard the MIR and ISS Space Station [58, 59, 60]. These experiments were originally intended to study full three-dimensional plasma crystals. At present these experiments have to overcome competing phenomena like "voids" [61, 62, 63], and particle vortices. The latter dynamic features have been assumed to be caused by forces like thermophoresis or ion drag, which are by far overcome by the dominance of the particle weight in terrestrial laboratory experiments, but play a very important role under microgravity conditions. One of the most challenging questions is the ambiguous strength of these forces. Experiments to verification of these forces are very rare and theoretical analysis and simulations give contradictory results.

The present thesis addresses the fundamental problem related to the force equilibria of dusty plasmas, which contribute to the current debate on nonlinear processes and weaker forces. Two different experiments under completely different plasma conditions have been carried out: first, oscillations of trapped particles in the plasma sheath, under the dominance of the gravitation force, and second, the observation of the motion of untrapped, falling particles in the plasma bulk.

In the sheath, the particles are levitated against gravity by the prevailing electric field [64, 65, 1, 66]. In previous experiments, the linear response of the particles to external periodical perturbations had been studied so far [4, 47, 57]. In the first experiment presented here, the nonlinear contributions of position dependent dust charges and the nonlinear electric fields to the unharmonicity of the confining potential well will be discussed. This allows to derive a quantitative model of the particle trapping and oscillation in the plasma sheath, and the undergoing sheath properties.

In the second experiment, in order to measure the weaker forces like ion drag [67, 68] and thermophoresis [69, 70, 68], the particles have been studied in free falling motion through a long plasma column. There the gravitation is balanced by the neutral drag force and the more subtle forces determine the radial particle motion. The behavior of the falling particles is observed here in the quasi-neutral plasma bulk. The radial dynamics of the particles allows the determination of forces from the analysis of the particle trajectories.

The study of the radially acting thermophoresis, ion drag, and electric field forces represent a novel laboratory experimental approach that contribute to the understanding of the "void" formation. The mechanism of the "void" formation in microgravity experiments is still an unsolved problem.

This work is a cumulative thesis and is structured as follows: in the second chapter the fundamentals of complex plasmas are presented, namely capacitive RF discharges, the charging process of dust particles, the forces acting on a dust

grain, and a brief theory of the vertical oscillations. The first experiment on nonlinear oscillations of particles in the plasma sheath will be described in the third chapter. The experiments carried out with free falling particles in a long plasma column will be presented in the fourth chapter, followed by a summary and conclusions. The submitted and published papers to peer-reviewed journals and the contributions to international conferences are attached in the Appendix.

2 Complex Plasmas. General Description

2.1 Fundamentals of RF discharges

In this section the basic properties of RF discharges will be presented. A short introduction will familiarize the reader with the range of application of RF discharges in processing technologies as well as in laboratory research in complex plasmas. Since the plasma sheath of an RF discharge is essential for particle trapping in laboratory experiments, the fundamental physics of the sheath will be presented, followed by the theoretical self-consistent sheath model of Lieberman and Lichtenberg. The operating regimes of RF discharges and the fundamental ideas of using the RF capacitive discharges in particle trapping will close this section.

2.1.1 Introduction

Due to the electric charge attained by the dust particles in plasmas, they can interact with the plasma electric fields or with electron and ion flows, as well as with each other via electric forces. The study of dusty plasmas cannot be carried out without a detailed analysis of the plasma and of these interactions, which are the source of all the phenomena in these systems. Our experiments have been carried out in capacitively coupled RF discharges, so this is the type of plasma which will be described in the following.

RF discharges became an important research topic in fundamental physics already in the early fifties of the 20th century [71, 72]. Later, theoretical approaches through simulations have been performed, among others, by Belenguer and Boeuf [73, 74], or by Surendra and Graves [75, 76], as well as by Godyak and coworkers [77, 78, 79, 80]. In the eighties and nineties Liebermann and Lichtenberg have released a theoretical self-consistent model of the RF discharges, focused especially on the study of the plasma sheath [81, 82].

The development of microelectronic technologies has extended the area of application of RF discharges from laboratory to industrial devices. The connection between this type of discharges and dusty plasmas has been set also during the early years of employing plasma processing technologies for microelectronic devices, with the rising of contamination problem posed by the particles in processing devices.

2.1.2 The Structure of an RF Discharge

RF discharges have been extensively described by a number of authors [82, 83, 84, 85, 86](see Fig. 2.1).

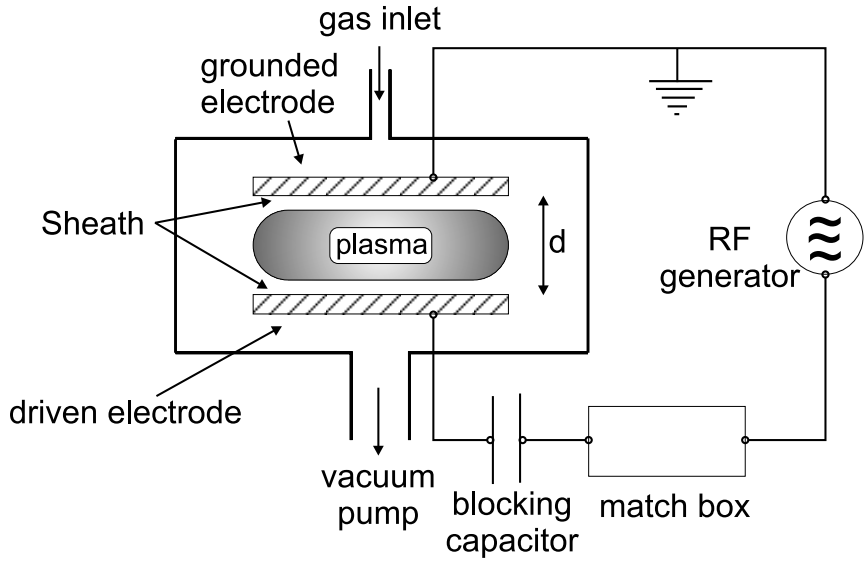

Figure 2.1: *Scheme of a capacitively coupled RF discharge driven in a parallel plate electrode configuration.*

The typical experimental setup of a capacitive RF discharge consists of a vacuum chamber with two parallel plate electrodes, one or both of them being driven at high frequency voltage. The second electrode can be either grounded, or driven in a push-push or push-pull regime with respect to the other. Due to the frequency ranges internationally allowed, the standard frequency used for driving RF discharges is f_{RF}=13.56 MHz, or higher harmonics. The applied power can vary within a wide range from a few mW up to several kW. The RF power is coupled from the RF generator with the standard 50 Ω output impedance to the plasma impedance using a match box, which is a tunable network consisting of capacitors and coils. Between the powered electrode and the match box, an additional capacitor can be mounted in some configurations in order to block any DC components.

2.1.3 The RF Plasma Sheath

One of the basic properties of any plasma and, consequently also of the RF plasma, is its quasi-neutrality

$$|n_e - n_i| \ll n_{e,i}, \tag{2.1}$$

where n_e and n_i are the electron and ion densities respectively. Thus the plasma bulk is almost free of electric fields.

The response time of the charge carriers is determined by the electron and ion plasma (Langmuir) frequencies

$$\omega_{pe,pi} = \sqrt{\frac{n_{e,i}e^2}{\varepsilon_0 m_{e,i}}}, \tag{2.2}$$

where $m_{e,i}$ are the mass of electrons and ions respectively, for which, under typical plasma conditions with $n_{i,e}$=10^9 cm^{-3}, the following relation is valid

$$\omega_{pi} \leq \omega_{RF} \ll \omega_{pe}, \tag{2.3}$$

with $\omega_{RF} = 2\pi f_{RF}$. This relation shows that the massive ions are usually not able to follow the fast oscillating RF electric field, thus they can only react to the time-averaged fields. On the other hand, the more mobile electrons can react instantaneously to the RF oscillation. The powered electrode is negatively self-biased with respect to the plasma most of the RF period due to the higher electron mobility, and the electrons are repelled from the electrodes, leaving the electrode vicinity filled only with ions (see Fig. 2.2). This region is called the plasma sheath. Only for a very short interval of the RF cycle the sheath is quasi-neutral, but the much higher mobility of electrons compensates the electron deficit and ensures the balance of electron and ion currents over the whole RF cycle.

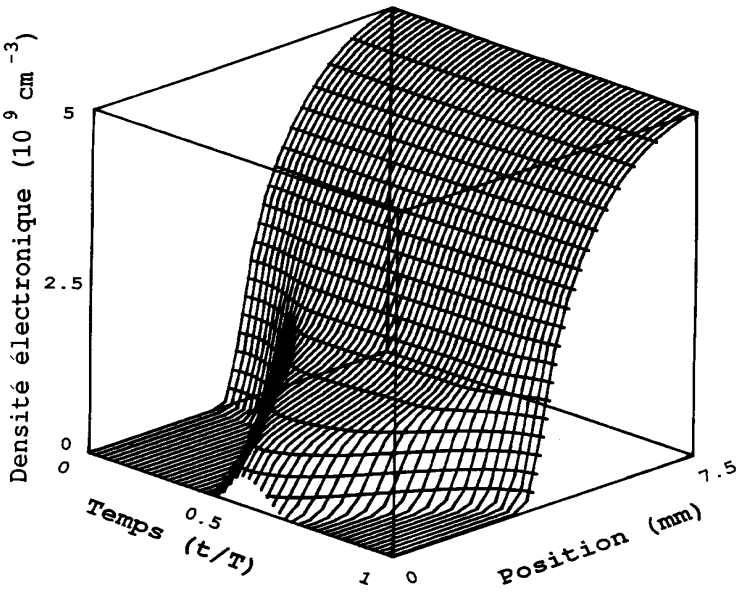

Figure 2.2: *Space-time variation of the electron density in the sheath of an RF discharge in Helium at 400 Pa. From [73].*

Very important for particle trapping is the strong electric field in the sheath which is used in dusty plasma experiments to balance the weight force of the dust particles. It ensures appropriate conditions for the existence of 2D particle clouds when particles of the same size are introduced into the sheath.

Between the plasma sheath and the quasi-neutral plasma a transition region, namely the presheath exists, where the quasi-neutrality is not very strongly perturbed. In the presheath the ions are accelerated towards the sheath to the so-called Bohm velocity [68]

$$v_{Bohm} = \sqrt{\frac{k_B T_e}{m_i}}, \tag{2.4}$$

with T_e being the electron temperature and k_B the Boltzmann's constant. In the electric field of the sheath the ions are further accelerated, leading to a decrease of the ion density with the depth inside the sheath due to continuity reasons.

The fraction α of the RF cycle when the sheath is quasi-neutral, averaged over the whole RF cycle, also describes the ratio of the time-averaged densities of electrons to ions.

Assuming a radial homogeneity, the Poisson's equation

$$\varepsilon_0 \vec{\nabla} \cdot \vec{E} = \varepsilon_0 \frac{\partial E(x)}{\partial x} = \rho(x) = e n_i(x)(1 - \alpha(x)), \tag{2.5}$$

yields for a constant charge density $\rho(x)$

$$E(x) = E_0 \left(1 - \frac{x}{\overline{x}_s}\right). \tag{2.6}$$

The electric field is found to increase linearly with depth in the sheath relative to the time-averaged position of the sheath edge $\overline{x}_s$. The electric potential is then derived to be parabolic, according to

$$\phi(x) = \int_{\overline{x}_s}^{x} E(\xi) d\xi = -\frac{\overline{x}_s}{2} E_0 \left(1 - \frac{x}{\overline{x}_s}\right)^2. \tag{2.7}$$

In the following subsection a more advanced model of the plasma sheath is presented. It gives information on the electric field distribution and the electron and ion densities in the plasma sheath and will be used in the analysis of the nonlinear oscillation experiments in Chapter 3.

2.1.4 The Lieberman-Lichtenberg Plasma Sheath Model

An analytical, self-consistent solution of the collisionless RF sheath driven by an RF current source is presented here [81, 82]. This model provides analytical expressions for the time-averaged densities of ions and electrons, as well as for the electric field and electric potential in the sheath, under the following assumptions: the ion motion in the plasma sheath is collisionless, and the electron Debye length λ_D is assumed to be much smaller then the sheath thickness s_m.

Fig. 2.3 shows a sketch of the time evolution of the electron density in the sheath, at a certain moment of the RF cycle. The electron sheath oscillates between a maximum thickness of a few Debye lengths above the electrode and the minimum thickness 0. The dotted line represents the electron density averaged over an RF period and the full line the ion density. The time varying electron

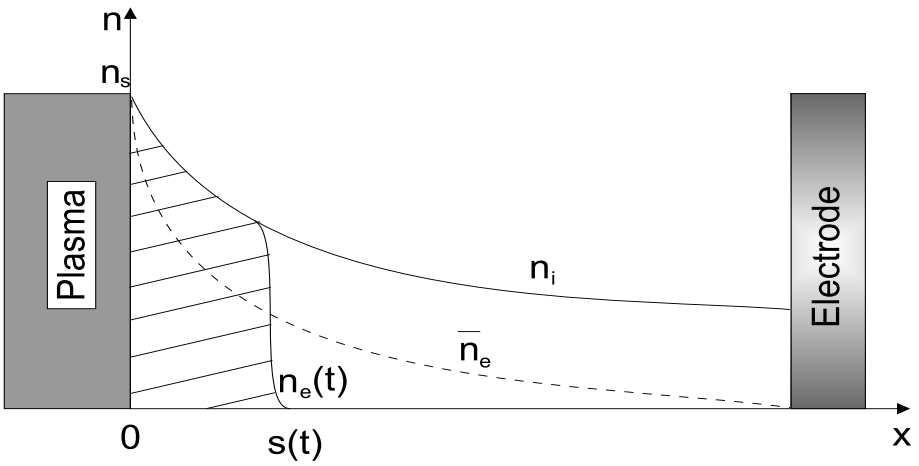

Figure 2.3: *Electron and ion density distribution in the capacitive RF sheath.*

density $n_e(t)$ is characterized by the moving edge $s(t)$. The time-averaged density $\overline{n}_e$ is smaller than n_i.

Without insisting on the calculation details, the results of this model are the following [81]: The nonlinear oscillation of the electron sheath is found to be described by

$$\frac{x}{\widetilde{s}_0} = (1-\cos\varphi) + \frac{H}{8}\left[\frac{3}{2}\sin\varphi + \frac{11}{18}\sin 3\varphi - 3\varphi\cos\varphi - \frac{1}{3}\varphi\cos 3\varphi\right], \tag{2.8}$$

where $2\varphi(x)$ is the phase interval during which $s(t) < x$,

$$H = \frac{1}{\pi}\frac{\widetilde{s}_0^2}{\lambda_D^2}, \tag{2.9}$$

defines the thickness of the sheath with respect to the electron Debye length $\lambda_D = (\varepsilon_0 T_e/en_{0,i})^{1/2}$ at $x = 0$, $\widetilde{s}_0 = \overline{J}_0/(e\omega n_{0,i})$ is an effective oscillation amplitude, $n_{0,i}$ is the plasma density at the sheath edge $x = 0$ and $\widetilde{J}_0$ and ω are the amplitude, respectively the frequency of the RF powering current. The ion density is found to be

$$\frac{n_i}{n_{0,i}} = \left[1 - H\left(\frac{3}{8}\sin 2\varphi - \frac{1}{4}\varphi\cos 2\varphi - \frac{1}{2}\varphi\right)\right]^{-1}, \tag{2.10}$$

and the time-averaged electron density is

$$\frac{\overline{n}_e}{n_{0,i}} = \left(1 - \frac{\varphi}{\pi}\right)\frac{n_i}{n_{0,i}}. \tag{2.11}$$

The time-averaged electric potential is determined by

$$\frac{\overline{\phi}}{T_e} = \frac{1}{2} - \frac{1}{2}\left[1 - H\left(\frac{3}{8}\sin 2\varphi - \frac{1}{4}\varphi\cos 2\varphi - \frac{1}{2}\varphi\right)\right]^2. \tag{2.12}$$

This self-consistent model of the plasma sheath is a very useful instrument in the estimation of plasma parameters in the sheath. In Chapter 3 for the study of

particle oscillations this model is used as theoretical reference in the analysis of the experimental data. As input data of the model, the neutral plasma density, the electron and ion temperature, and the parameter H are needed. At each instant of the RF cycle the ion and electron densities can be determined and then equated in the balance of currents on the dust particle to obtain the electric charge on the particle (see Section 2.2 and [A.1]). From the electric field in the sheath, the problem of static and dynamic equilibrium of the particle is solved when the electric field force is balanced by the particle weight.

2.1.5 Plasma Modi

At this point a short presentation of the mechanisms which ensure the existence and operating of RF discharges is necessary. Two operating regimes can be distinguished: the α-regime which is specific for low powers, and the γ-regime for high driving powers. They differ from each other by the way how the RF energy is transported to the electrons.

For relatively high pressures (a few tens of Pa) and low powers, the oscillating sheath edge pushes the electrons towards the bulk plasma, like surfers on a wave, thereby accelerating them. These electrons represent a small but energetic population of electrons (about 10 eV) which deliver their energy by collisions to the other plasma components. This energy compensates the losses to walls or electrodes. The corresponding plasma regime is called wave-rider-regime or α-mode [87].

When the plasma is driven at lower gas pressure the mean free path of the electrons is much larger than the distance between the electrodes, thus they oscillate several times between the sheaths before they suffer a collision. On average, the electron energy is increased due to reflections at the oscillating sheaths. This stochastic heating is sufficient to compensate the losses.

Another electron heating process is dominant when the potential drop in the sheath is so high that the ions accelerated in the sheath release secondary electrons when colliding with the electrode. Additionally, the fast ions, when colliding with neutral atoms are able to ionize them. The resulting secondary or ionization electrons form a very small population of high energy with high ionization efficiency. They produce a large number of electrons ($n_e > 10^{11}$ cm^{-3}) of low energy, under 1 eV. This is the so called γ-regime, which shows a lot of similarities with the DC glow discharges, where the electrons are accelerated within the cathode voltage drop.

The transition from α- to γ-regime occurs rapidly and can be observed in the change of plasma brightness [88, 89] as well as in the modification of the electron temperature and density [79, 80].

Due to the low powers used in our experiments, we assume that the discharges are running in the α-regime.

2.1.6 The Plasma Sheath as Particle Trap

Until now, the main properties and mechanisms of the RF plasmas have been presented. At this point it is clarified why especially this type of discharge has been chosen for the complex plasma experiments.

First of all, these plasmas ensure the necessary charge carriers for charging the dust grains (see Section 2.2 for details). The particles attain a high negative electric charge in the plasma sheath. Here, due to the strong linearly increasing electric field, the gravitation force acting on the particles can be balanced in almost all cases. The charge accumulated on the dust grains does not only ensure their levitation, but determines also the electrostatic particle-particle interaction. This mutual repulsion permits the particles to build regular structures, the so-called plasma crystals, under the presence of a weak horizontal confinement. The charging process as well as the balance of various forces acting on the particles determines their specific properties and will be discussed in the following chapters.

2.2 Particle Charging

2.2.1 Introduction

At the time when it was observed that the dust particles formed in processing devices for microelectronic chips are levitated above the electrodes, the search for an explanation led back to the early probe theory of Mott-Smith and Langmuir [90]. This was the starting point for a new field of research: charging of small particles in plasmas. Already in the early eighties, the charging process of particles in space has been studied in detail by Whipple [91]. The early probe theories have been further improved [92, 93] for new experimental conditions.

Small particles act like floating probes in the plasma. They collect charge carriers and thus attain a certain electric charge, negative or positive, depending on the dominant charging processes. The magnitude of this charge is of vital importance because it defines the strength of particle-particle or particle-plasma electrostatic interactions and is responsible for all the interesting phenomena and properties of complex plasmas. For example, the electrostatic repulsion between neighboring particles defines the strong coupling in 2D particle layers, where oscillations and waves can be generated. Therefore, an analysis of the charging process of dust grains in both the plasma bulk and the plasma sheath is desirable. Particle charging has been discussed in more detail by [94, 91].

2.2.2 The OML Probe Theory

The classical Orbital Motion Limited theory developed by Mott-Smith and Langmuir [90] in 1926 represented a reference in the probe diagnostic analysis for several decades. This model describes the way how the study of the currents collected by a small probe ($a \ll \lambda_D$ [95, 96]) leads to information on the plasma

parameters. The validity of this theory is limited to the ideal case when the electrons and ions are collisionless, and when the density and velocity distributions of charge carriers are isotropic.

The problem of the particle floating potential is the inverse problem (compared to the probe diagnostics), where the plasma parameters and thus the currents reaching the particles are known and the floating potential of the particle surface is to be determined.

Ion and Electron Currents

Since in the laboratory plasmas the positive ions belong usually to the species attracted by the charged particles, their dynamics will be presented in the following. According to the classical OML theory, the ions collide with the particle when they have an impact parameter smaller than a well-defined value b_c (see Fig. 2.4). If the impact parameter is larger than b_c the ions are deflected in the electrostatic field of the particle but are not collected on the particle surface. The above mentioned limit b_c corresponds to the case where the ions impact the particle tangentially and depends on the magnitude of the attractive central potential. This gives the name of the Orbital Motion Limit theory (OML).

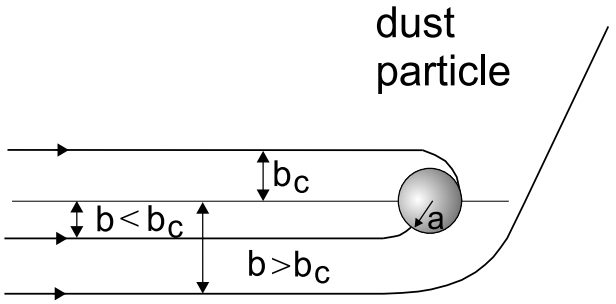

Figure 2.4: *Only ions with an impact parameter smaller than the limit b_c can contribute to the ion current on the dust grain. The other ones ($b > b_c$) are deflected in the electrostatic potential of the particle.*

When integrating over the contributions of all ions which hit the particle, the ion current is obtained as

$$I_i = \pi e n_i a^2 \sqrt{\frac{8k_B T_i}{\pi m_i}} \left(1 - \frac{e\phi_{fl}}{k_B T_i}\right), \tag{2.13}$$

where $\sigma_i = \pi b_c^2 = \pi a^2(1 - e\phi_{fl}/k_B T_i)$ is the ion collection area of the particle, $\sqrt{8k_B T_i/\pi m_i}$ is the ion thermal velocity, and ϕ_{fl} is the particle floating potential. The integration has been carried out under the assumption of a Maxwellian ion distribution. It can be observed that $\pi b_c^2 > \pi a^2$, since $\phi_{fl} < 0$, thus the ion collection area of a negative particle is larger than its geometric cross area.

For the electrons, the calculations are similar, with the only difference that the electron collection cross section is $\sigma_e = \pi b_{c,e}^2 = \pi a^2(1 + e\phi_{fl}/k_B T_e)$. The

electron current is

$$I_e = -\pi e n_e a^2 \sqrt{\frac{8k_B T_e}{\pi m_e}} \exp\left(\frac{e\phi_{fl}}{k_B T_e}\right). \tag{2.14}$$

It was considered here that only electrons with a higher energy than the particle repulsive potential $m_e v_e^2/2 > e\phi_{fl}$ are collected.

The ion and electron currents collected by a positively charged particle can be determined the same way when the roles of attracted/repelled species are changed. Nevertheless, due to the higher temperature and mobility of the electrons such a situation is quite seldom.

The results of the OML model have been proved to be valid when employed in the the case of small particles ($a \ll \lambda_D$) [95, 96]. Nevertheless, limitations of this model are to be regarded.

Limitations

The condition of collisionless ions and electrons is not fulfilled in typical experimental situations due to the short collision mean free paths of the charge carriers. For example in Helium, at pressures around 100 Pa, the mean free path for ions λ_{mfp} is of the same order, even smaller than the Debye length.

When ion or electron drifts are present in the plasma, the second condition of validity is infringed in the way that the populations of charge carriers are no longer Maxwellian when the drift velocity is comparable to the thermal velocity.

2.2.3 Ion and Electron Currents under Charge Carrier Drifts

When the particle is situated in a plasma region dominated by drifts of the charge carriers, the non-isotropic distribution of charging collision events have to be taken into account. Whipple derived the charging currents for repulsive potentials ($q\phi_{fl} > 0$ typically for electrons) [91]

$$\begin{aligned} I \;&= \tfrac{\pi a^2}{2} n e v_d \Bigg(\left(1 + \tfrac{v_{th}^2}{2v_d^2} - \tfrac{U^2}{v_d^2}\right) \left[\operatorname{erf}\left(\tfrac{v_d+U}{v_{th}}\right) + \operatorname{erf}\left(\tfrac{v_d-U}{v_{th}}\right) \right] + \tfrac{v_{th}}{\pi^{1/2} v_d} \cdot \\ &\cdot \left\{ \left(\tfrac{U}{v_d} + 1\right) \exp\left[-\left(\tfrac{v_d-U}{v_{th}}\right)^2 \right] - \left(\tfrac{U}{v_d} - 1\right) \exp\left[-\left(\tfrac{v_d+U}{v_{th}}\right)^2 \right] \right\} \Bigg), \end{aligned} \tag{2.15}$$

where n, m and v_{th} are the density, mass and thermal velocity of the analyzed species, v_d is the drift velocity of the plasma components and $U = (2e\phi_{fl}/m)^{1/2}$ is the additional velocity gained by the charge carrier in the electrostatic potential of the particle. In the limit of large drift velocities, this current reduces to the form $I = \pi a^2 n e v_d (1 - 2e\phi_{fl}/m v_d^2)$. This is the typical situation in the plasma sheath where the ions are accelerated in the strong electric field to supersonic velocities and thus the thermal agitation plays no dominant role.

For attractive potentials (typical for ions) an approximative expression for current is [91]

$$I = \pi a^2 n e v_d \left[\left(1 + \frac{v_{th}^2}{2v_d^2} + \frac{U^2}{v_d^2} \right) \mathrm{erf}\left(\frac{v_d}{v_{th}} \right) + \frac{v_{th}}{\pi^{1/2} v_d} \exp\left(- \frac{v_d}{v_{th}} \right)^2 \right]. \qquad (2.16)$$

The validity is limited to the case when the collection radius is smaller than the radius of the sheath around the particle.

These equations reduce to the OML expressions when the drift velocity is small compared to the thermal velocity. For example, for ions having a drift velocity of about 20% of the thermal velocity, the variation from the OML model of the ion current collected on a particle of 5 μm radius is less than 1%. Thus, this model is a very useful analysis instrument when the drift velocities are comparable to the thermal velocity. Otherwise, the OML theory provides sufficiently precise results and therefore is preferred.

2.2.4 Other Charging Processes

Apart from the above mentioned currents which represent the main source of electric charge on the dust particles, a few other processes like photoemission and secondary electron emission can be important, under circumstances which are mostly found in space [91]. Other processes like the thermionic emission or field emission of electrons, electrostatic disruption, radioactivity, impact ionization, enhanced ionization or enhanced collection of electrons are relevant only under extreme conditions, especially for dusty plasmas in space, and will therefore not be discussed.

Electrons colliding with a dust particle, can either enter the material or be reflected, releasing secondary electrons. This electron outflow can be considered as a positive current onto the particle [97, 98]. The electron secondary emission can be produced also by ion bombardment [99, 100, 101]. For plastic materials similar to the particles used in our experiments high electron or ion energies are necessary for producing secondaries, thus the contribution of secondary electron emission to the particle charging is considered negligible in our case [102].

In usual laboratory plasmas the UV emission is quite small, so the photoemission plays a negligible role among other charging processes and is commonly not to be accounted.

2.2.5 Dust Particles as Spherical Floating Probes

The particle charge is directly related to the floating potential. To obtain the floating potential, the particles can be considered as isolated, floating spherical probes which collect ion and electron currents under the influence of the plasma. Thus, the charging can be described as a process depending on the plasma parameters and floating potential of the particles.

The floating potential is the potential of the grain surface when the dynamic balance of the electron and ion currents to the particle is reached.

$$I_i + I_e = 0 \tag{2.17}$$

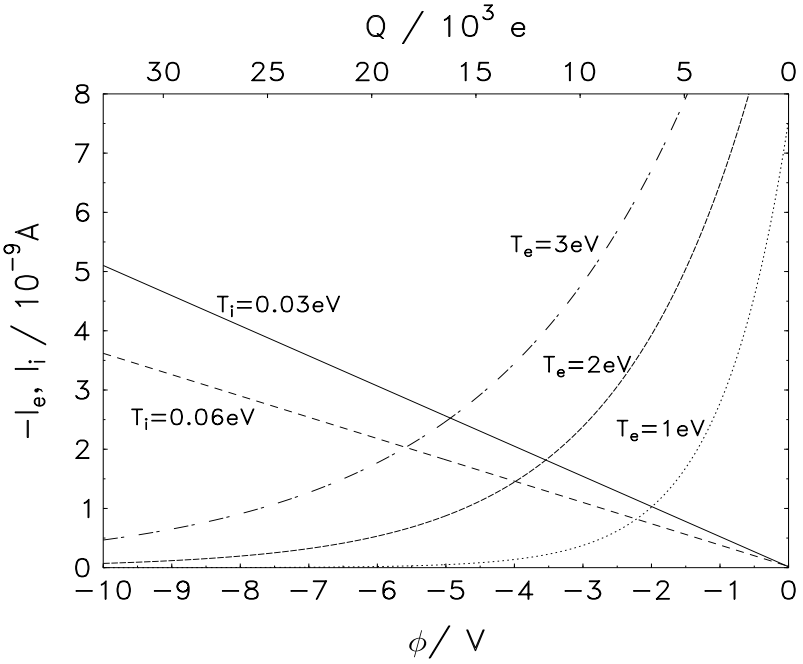

Figure 2.5: *Ion and electron currents to a spherical particle ($2a = 9.47\ \mu m$) in a Helium plasma ($n_{i,e} = 1 \cdot 10^{-9}\ cm^{-1}$) for various electron and ion temperatures T_e and T_i. On the horizontal top axis, the corresponding floating charge of the particle is indicated. (From [83])*

For the ideal case of an isotropic, Maxwellian plasma, the floating potential of the particle is obtained by balancing the OML electron and ion currents. Employing the notation $\eta = e\phi_{fl}/(k_B T_e)$, the transcendent equation

$$1 - \frac{T_e}{T_i} \cdot \eta = \frac{n_e}{n_i}\sqrt{\frac{m_i}{m_e}\frac{T_e}{T_i}} \cdot \exp(\eta), \tag{2.18}$$

can be solved numerically. Under typical discharge conditions with $n_e = n_i$ and $T_e \gg T_i$, $e\phi_{fl} \approx 2k_B T_e$.

Fig. 2.5 shows the ion and electron currents to the particle surface for various plasma parameters. The crossing points between ion and electron currents represent on the abscissa the corresponding floating potential. It can be observed that the negative floating potential of a dust grain increases with the electron temperature. This is caused by an increasing number of electrons that reach the particle surface with increasing electron temperature.

For evaluating the particle charge $Q_p = C\phi_{fl}$, the particle is treated as a spherical capacitor with the capacitance

$$C = 4\pi\varepsilon_0 a\left(1 + \frac{a}{\lambda_D}\right), \tag{2.19}$$

where the Debye shielding in plasma is accounted. For small particles $a \ll \lambda_D$ it reduces to $C = 4\pi\varepsilon_0 a$. For the given particle and plasma parameters, the floating charge can be extracted from Fig. 2.5, on the horizontal top axis. Thus, for an ion temperature of T_e=0.03 eV, the charge varies from approximately 6500 e at T_e=1 eV to 17000 e at T_e=3 eV.

When drifting ions are taken into account, as in the plasma sheath, the OML electron current is to be balanced with the ion current deduced by Whipple [91]

$$\pi a^2 n_e e \sqrt{\frac{8k_B T_e}{\pi m_e}} \exp\left(\frac{e\phi_{fl}}{k_B T_e}\right) = \pi a^2 n_i e v_{d,i} \left[\left(1 + \frac{v_{th,i}^2}{2v_{d,i}^2} + \frac{U^2}{v_{d,i}^2}\right)\mathrm{erf}\left(\frac{v_{d,i}}{v_{th,i}}\right) + \right.$$
$$\left. + \frac{v_{th,i}}{\pi^{1/2} v_{d,i}} \exp\left(-\frac{v_{d,i}}{v_{th,i}}\right)^2\right], \qquad (2.20)$$

where $U = (2e\phi_{fl}/m_i)$. Under the typical experimental conditions like in the experiments described in Chapter 4, the particle charge is changed by less than 1% compared to the OML results. This advanced model is suitable for strong drifts of plasma components, otherwise the OML model provides accurate enough results.

2.2.6 Particles in the Plasma Sheath

As shown in Section 2.1, the plasma sheath is usually quasi-neutral for a very short interval of the RF cycle (the fraction α), while for most of the time, the sheath is almost free of electrons. Thus, averaging over one RF cycle, the sheath is dominated by ions. Therefore, different densities are to be considered when analyzing the charging of particles in the plasma sheath

$$n_e \neq n_i \Leftrightarrow n_e = \alpha n_i. \qquad (2.21)$$

ϕ_{fl} can be calculated using (2.18) with different densities. For $\alpha = 1$ the quasi-neutral plasma case is reiterated, whereas the extreme case where $\alpha = 0$, no electrons are present anymore in the sheath, and the particles charge positively.

The temporal evolution of the particle charge in the plasma leads to the charging time parameter [103]

$$\tau_i = 4\pi\varepsilon_0 a \frac{k_B T_e}{e} \frac{1}{\pi a^2 e n_i v_{th,i}}, \qquad (2.22)$$

which can be considered as the characteristic time $\tau = CR$ necessary for discharging the initially charged spherical capacitor C represented by the particle, through the resistance $R = U/I$ of the surrounding plasma. Considering a typical plasma with T_e=3 eV, T_i=0.03 eV, and n_i=10^{15} m^{-3}, the charging time constant is of the order of τ_i=1 μs.

The finite charging time of the particles can play an important role especially at low pressures, where they can drive self-excited particle oscillations [104].

Besides these variations of the charge due to the RF voltage oscillation, stochastic charge variations can occur, which are produced by the discreetness of charge carriers [105, 106]. The stochastic fluctuations are of the order $\delta Z = 0.5\sqrt{Z}$ and thus negligible for particles with Z=10^4.

2.2.7 Influence of a Large Number of Particles

So far, the charging theory has been presented for single particles in a plasma environment. Nevertheless, a large number of particles are usually injected, thus the plasma parameters might be strongly modified by their presence.

The quasi-neutrality of the system plasma-particles can be written as

$$n_i e - n_e e - n_{part} C\phi_{fl} = 0, \tag{2.23}$$

considering the particles attaining all the same charge $C\phi_{fl}$. Here, n_{part} is the number density of the dust grains, thus $C\phi_{fl}$ represents the space charge density bound to the particles. This equation shows that a large number of particles in the plasma leads to a drastic decrease of the density of free electrons, when the particle space charge is a considerable part of the space charge of free electrons. Thus the charging process is perturbed and consequently, the individual charge of a single particle decreases. This charge depletion has been studied by Havnes et al. [107, 108] and by [106], and will be discussed in relation to our experiments on the falling dust particles in Chapter 4 and [A.2] .

2.3 Forces Acting on the Dust Particles

The forces acting on the dust particles determine the motion and/or local equilibrium of the dust grains, so their determination is a fundamental goal in the study of complex plasmas. In this section we give an overview over the forces acting on the dust particles in a plasma discharge. It is divided into two parts: the first one deals with the forces acting independently of the presence of plasma, and the second one concerning the interaction of particles with the surrounding plasma. A short analysis of the particle-particle interaction followed by discussions on the dominance of various forces under various experimental conditions close this chapter. Extended description of the forces acting on a dust particle can be found in [84]

2.3.1 Gravitation and Neutral Gas Friction Forces

This section deals with the forces which act on the dust particles independently of the presence of plasma, namely the gravitational force and the friction force.

Gravitation Force

Like all bodies present in the gravitational field of Earth, the dust grains feel the weight force

$$\vec{G} = m_p \vec{g} = \frac{4}{3}\pi a^3 \varrho \vec{g},$$

with a being the particle radius, g the gravitational acceleration and ϱ the mass density of the particle material. For example, a particle of radius a=4.75 μm made

of Melamine Formaldehyde (ϱ=1514 kg/m^3) has a mass of m_p=6.8×10^{-13} kg and correspondingly, the weight force is G=6.7×10^{-12} N. The dependence of this force on the third power of particle radius makes it very important for large particles (over 1 μm), but can be neglected for nanometer sized particles with respect to other forces like the electric field force.

A new field of investigations on complex plasmas has been opened by experiments on parabolic flights, or by experiments aboard the International Space Station (ISS) in order to reduce the dominant influence of the gravitation force on micron-sized particles. This made possible the observation of three dimensional particle structures which have not been observable so far [59].

Neutral Gas Friction

The neutral gas friction force is the result of momentum transfer from the neutral gas molecules/atoms to a dust particle when moving relatively to the gas [109]. For a single particle with a radius much smaller than the mean free path for neutral-neutral collisions, and a relative velocity smaller than the gas thermal velocity, so that the neutral gas velocity distribution is not perturbed by the presence of the dust particle, the friction force is described by

$$\vec{F}_{frict} = -\delta \frac{4}{3} \pi a^2 n_n m_n v_{th,n} \vec{v}_{rel}. \tag{2.24}$$

The Millikan coefficient δ describes various types of reflection of the neutrals (specular or diffuse) at the particle surface and can vary between 1 and 1+4/9. n_n, m_n and $v_{th,n}$ are the number density, mass and thermal velocity of the neutral gas. This equation has been developed to describe the neutral gas friction on the oil droplets in Millikan's experiment.

When normalized to the particle mass, this equation reads as

$$\vec{F}_{frict} = -m_p \beta \vec{v}_{rel}, \tag{2.25}$$

where

$$\beta = \frac{\delta n_n m_n v_{th,n}}{a \varrho} \tag{2.26}$$

is the normalized friction coefficient.

In the analysis of our experimental data, the second form of the neutral friction force will be used. For a spherical MF particle of radius a = 4.25 μm and a pressure of 100 Pa in Helium, β = 28.3 s^{-1}, which means that the given drifting particle will come to rest within a few milliseconds. If the particle falls freely through the neutral gas, a constant drop velocity regime is reached within the first few milliseconds. The situation where one of the initial assumptions is not satisfied, is studied by Vestner et al. [69, 70], or by [110].

In our experiments where the particle relative velocities are relatively small, the Epstein's formula has been used.

It is known that small dust particles have the tendency to form clusters due to adhesion, which will modify the force balance of gravity and neutral drag during

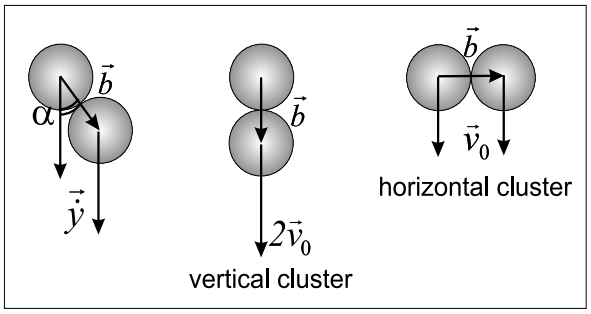

Figure 2.6: *The terminal velocity for a 2-particle cluster strongly depends on the cluster orientation.*

the free fall. For simplicity, the behavior of a free-falling two-particle cluster will be analyzed. The dynamic vertical equilibrium is approximatively described by

$$2m_p g - \kappa\tilde{\beta}a^2\dot{y} = 0, \tag{2.27}$$

with the orientation coefficient (see Fig. 2.6)

$$\kappa = 1 + |\sin\alpha|, \tag{2.28}$$

and

$$\tilde{\beta} = \delta\frac{4}{3}\pi m_n n_n v_{th,n}. \tag{2.29}$$

Here, α is the angle between the distance vector between the two particles $\vec{b}$ and the vertical velocity vector $\vec{y}$. It is evident that, if $\vec{b}$ is parallel to the velocity vector $\dot{\vec{y}}$, the cluster will fall with a constant velocity twice as high as the velocity of a single particle (see Fig. 2.6). If the distance vector is perpendicular to the velocity, the cluster velocity is the same as the velocity of a single particle. Between these two extreme situations, depending on the cluster orientation, the constant falling velocity continuously varies between once and twice the one-particle velocity. In reality, the high complexity of clusters and their eventual rotation involves a broad distribution of measured velocities, so it can be considered as a source of experimental errors in the drop experiments (Chapter 4). The higher the particle number in a cluster, the faster the cluster will fall, so that single particles will have the lowest velocity. In conclusion, it is usually desired that the particle clusters are separated into individuals. A method of cluster explosion is presented in Chapter 4 and [A.2].

2.3.2 Plasma Forces Acting on the Dust Particles

The plasma forces acting on the dust grains are the result of several effects like momentum transfer from the plasma components to the particle (ion drag and thermophoretic force), or electrostatic interactions of the charged particles with the plasma electric fields, as well as polarization effects which might occur in a plasma under the effect of considerable electric fields and particle flows (polarization forces).

Electric Field Force

The most important force which acts on the particles when injected in the plasma is the electric field force because it is able to balance the gravitation force in the plasma sheath

$$\vec{F}_{el} = Q_p \vec{E}. \tag{2.30}$$

As shown in the first section, the electric field is

$$E(z) = \frac{\rho}{\varepsilon_0}(\overline{z}_s - z), \tag{2.31}$$

where z is the local position in the sheath and $\overline{z}_s$ is the average sheath edge position. Due to the linear increase of the electric field in the plasma sheath, at a certain level, depending on the particle mass, the gravitation force is balanced, thus the particles can be levitated. The charge accumulated on the dust grain is linearly dependent on the particle radius (see Section 2.2). So even for small particles, the electric field force can reach high magnitudes when the acting electric field is strong enough. Nevertheless, since the plasma bulk is almost free of electric fields, the electric field force is very small there when compared to the gravitation force.

Considering the analysis of Hamaguchi et al. [111], the presence of the sheath has no influence on the particle dynamics if the sheath is unpolarized and spherically symmetric.

Polarization Forces

If the plasma polarizes as response to an external electric field, or the sheath around the particle brakes the spherical symmetry or polarizes, an additional action on the grain must be taken into account. This is the case of polarization forces.

For the study of the polarization effect, Daugherty et al. [112] have solved the Debye-Hückel equation in the case of a superimposed homogeneous electric field in the plasma assuming a spherical Debye sheath around the particle with the linearized radius defined by

$$\kappa_D = \frac{1}{\lambda_D} = \sqrt{\frac{e^2 N_\infty}{\varepsilon_0}\left(\frac{1}{k_B T_e} + \frac{\eta}{k_B T_i} + \right)} \approx \frac{1}{\lambda_i}, \quad \text{for} \quad T_i \ll T_e, \tag{2.32}$$

with N_∞ the unperturbed plasma density. The force acting on the particle due to the electric field is then

$$\vec{F}_E = -Q_p \underbrace{\left[\vec{E}\left(1 + \frac{(\kappa_D a^2)}{3(1+\kappa_D a)}\right)\right]}_{E_{eff}}. \tag{2.33}$$

This shows that the plasma polarization slightly increases the influence of the electric field. In this model the Debye sheath is assumed to remain unperturbed.

In most of the experimental cases, the particle radius is much smaller than the Debye radius, such as the total electric force reduces to the well-known form $\vec{F}_E = Q_p\vec{E}$.

The dipole moment of the system particle-polarized-plasma is then deduced

$$p_{eff} = 4\pi a^3 \varepsilon_0 \underbrace{\left[E\left(1 + \frac{(\kappa_D a)^2}{3(1+\kappa_D a)}\right)\right]}_{E_{eff}}. \tag{2.34}$$

In the usual limit $a\kappa_D \ll 1$, $p_{eff} = 4\pi a^3 \varepsilon_0 E$, which is the dipole moment induced on a sphere in vacuum by an external electric field. This model is violated if the sheath around the particle is significantly distorted by plasma flows, like for example in the plasma sheath of an RF discharge.

A more general model is presented by Hamaguchi and Farouki [113, 111], where the polarization of the Debye sheath around the dust particle is taken into account. The Debye-Hückel equation is solved in the linear approximation, for a shielding sheath characterized by

$$\kappa_D = \frac{1}{\lambda_D} = \sqrt{\frac{e^2}{\varepsilon_0 k_B}\left(\frac{n_i}{T_i} + \frac{n_e}{T_e}\right)}, \tag{2.35}$$

which becomes $1/\lambda_i$ in the limit of cold ions compared to electrons. With the assumption that the shielding cloud can be slightly perturbed by the external electric field and with accounting also for the pressure exerted by the flowing ions, the force acting on the grain is

$$\vec{F} = -Q_p\vec{E} - \frac{Q_p^2 \vec{\nabla}\lambda_D}{8\pi\varepsilon_0\lambda_D^2}. \tag{2.36}$$

The second term which describes the polarization force is always in the direction of decreasing Debye radius $\vec{\nabla}\lambda_D$, regardless of the sign of particle charge or of the electric field direction. For the limit of small ion drift velocities $v_i \ll v_{th,i}$, the average Debye length given by Eq. 2.35 is to be used. When $v_i \gg v_{th,i}$, the ion sheath is blown away from the particle vicinity, therefore the ions are not able anymore to contribute to the shielding process, and only electrons can form the sheath. Again the polarization force is negligible for small particles. Here only the pressure exerted by the ion flow on the particle sheath has been taken into account.

The Ion Drag Force

When the electrostatic interaction of the ions with the particles is taken into account, this interaction is described by the ion drag force. Both the ions directly collected by the particle and those deflected in the electric potential of the grain contribute to the ion drag force in the plasma [67, 114, 115, 116, 68].

Under the assumption that the ion mean free path for charge exchange or elastic collisions with the neutrals is larger than the Debye length, the ions with an

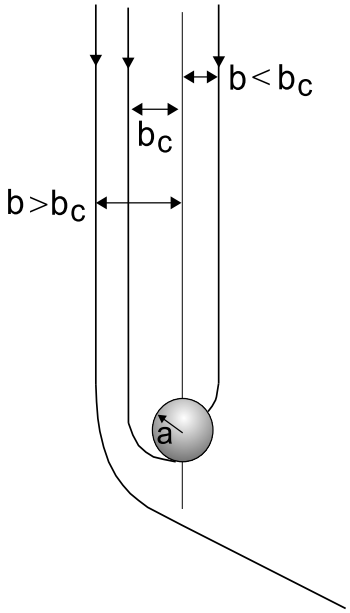

Figure 2.7: *Ions with an impact parameter smaller than b_c impact the particle and transfer their kinetic energy to the grain, while those with larger impact parameters are deflected in the particle electrostatic field, also leading to a momentum transfer.*

impact parameter smaller than the already defined orbit limit b_c (see Section 2.2.2 and Fig. 2.7) are collected and transfer their entire kinetic energy to the particle. The corresponding "collection force" is given by [67]

$$\vec{F}_{coll} = \pi a^2 m_i n_i \vec{u}_i v_s \left(1 - \frac{2e\phi_{fl}}{m_i v_s^2}\right), \tag{2.37}$$

where

$$v_s = \left(\frac{8k_B T_i}{\pi m_i} + u_i^2\right)^{1/2} \tag{2.38}$$

is the effective velocity of the ions approaching the particle, and $\vec{u}_i$ is the ion drift velocity.

Ions with an impact parameter larger than b_c are deflected in the grain electrostatic field transferring a part of their kinetic energy to the grain. The resulting "Coulomb force" is [67]

$$\vec{F}_{coul} = \pi b_{\pi/2}^2 m_i n_i \vec{u}_i v_s \ln\Lambda, \tag{2.39}$$

where

$$b_{\pi/2} = \frac{Q_p e}{4\pi\varepsilon_0 m_i v_s^2} \tag{2.40}$$

is the impact parameter for deflection at 90° and

$$\Gamma = \ln\Lambda = \frac{1}{2}\ln\left(\frac{\lambda_D^2 + b_{\pi/2}^2}{b_c^2 + b_{\pi/2}^2}\right) \tag{2.41}$$

is the Coulomb logarithm integrated over the interval from b_c to λ_D. The Coulomb force vanishes when the collection impact parameter $b_c \geq \lambda_D$ and strongly depends on the way how the Coulomb logarithm is chosen [117]. We use here the most actual and widely accepted form for the Coulomb logarithm given by Barnes et al. [67].

The total force is the contribution of the collected and deflected ions $\vec{F}_{ion} = \vec{F}_{coll} + \vec{F}_{coul}$. For a particle of radius a=5 μm, with n_i=10^9 cm^{-3}, T_i=0.03 eV, λ_D=0.4 mm Q_p=25000 e, and u_i=100 m/s the ion drag force F_{ion} is about 5 times smaller than the weight force. If the ion mean free path is smaller than the Debye length, the collisions which occur within the particle sheath might lead to ion trapping on closed orbits around the particle [118], modifying the strength of the ion drag force.

The Thermophoretic Force

Thermophoretic force acts on a particle in a temperature gradient of the neutral gas. For usual particle sizes of micrometers, it becomes important [69, 70, 115, 68] when the temperature gradient is of a few K/cm. Its microscopic mechanism relies on the fact that on the "hot side" of the grain the neutrals impact with a higher kinetic energy than on the "cold side". Thus a net momentum transport results on the particle in the opposite direction to the temperature gradient and the corresponding force is [68]

$$\vec{F}_{thermo} = -\frac{15}{16}\sqrt{\pi}\frac{a^2\kappa_n}{v_{th,n}}\vec{\nabla}T_n, \tag{2.42}$$

with κ_n the translation heat conductivity and $v_{th,n}$ the thermal velocity of the neutral gas. For Helium, κ_n=0.143 W/Km [119]. For a particle of radius a=5 μm, for $v_{th,n}$=420 m/s and a temperature gradient of 2 K/cm, the thermophoretic force is about 6 times smaller than the weight force. Therefore, it becomes measurable either for smaller particles, or when the gravitation is reduced.

As alternative to the expensive microgravity experiments, this effect has been used for levitation of small particles against gravitation in a vertical temperature gradient [63].

2.3.3 Particle-Particle Interaction

The particle-particle interaction force is the effect of mutual electrostatic repulsion between the negatively charged particles. When the interparticle distance is short enough such that the mutual repulsion force is not fully screened by the plasma, this particle-particle interaction begins to play a very important role. The mutual repulsion is given by the equation

$$F_{ij} = \frac{Q_i Q_j}{4\pi\varepsilon_0 r_{ij}} \exp\left(-\frac{r}{\lambda_D}\right)\left(1+\frac{r_{ij}}{\lambda_D}\right), \tag{2.43}$$

where $r_{i,j}$ is the interparticle distance and Q_i, Q_j are the charges on the particles i and j. Under the influence of an additional confinement, the particles find

an equilibrium position where the balance between the repulsion force and the confinement force is fulfilled. When confining a large number of particles, the dust grains can form regular structures, the so-called plasma crystals. The strength of the horizontal coupling is responsible for the structural stability and for its crystalline properties. The Coulomb coupling parameter can be defined as

$$\Gamma = \frac{Q^2}{4\pi\varepsilon_0 b}\frac{1}{k_B T_d} \tag{2.44}$$

where b is the mean interparticle distance and T_d the temperature of the plasma crystal. It represents the ratio of the Coulomb potential energy of neighboring particles to the thermal energy in the crystal. When $\Gamma > 1$ the system is said to be strongly coupled.

When the plasma shielding is taken into account, the interaction strength is defined by a Yukawa potential and, correspondingly, the coupling parameter becomes

$$\Gamma^* = \frac{Q^2}{4\pi\varepsilon_0 b}\frac{1}{k_B T_d}\exp\left(-\frac{b}{\lambda_D}\right). \tag{2.45}$$

It depends also on the ratio of interparticle distance to Debye radius.

The classical theory of aggregation states can be extended also to these systems [120, 121, 122, 123, 124]. A "gaseous" phase is characterized by a high thermal particle agitation, a "liquid" phase yields ordered grain drifts and in a "crystalline" phase the interparticle bonds are stable over a long period of time for $\Gamma > 168$ in the one-component-limit (OCP) with $\lambda_D \longrightarrow \infty$. The crystalline state is even suitable for observation of oscillations and waves.

2.3.4 Discussion

From this brief description of the important forces acting on the dust particles in a complex plasma, it is clear that the electric field force and the particle weight play the most important role, while the others are much smaller and thus difficult to measure. This is the typical case of particles trapped in the plasma sheath, where the electric field force balances the weight force. When the gravitation influence is reduced or compensated, like in microgravity experiments, the particles do not sediment in the sheath and thus ion drag and thermophoresis together with the electric field force in the plasma bulk become dominant.

When particles are droped through a plasma column (see Chapter 4 and [A.2]), the gravitation force is balanced by the neutral gas friction. Thus the effect of the other forces like ion drag or thermophoresis can be observed and measured. This is possible due to the fact that the balance of the gravitation force occurs in the vertical direction, while the action of ion drag, and thermophoresis occurs in the horizontal direction, being balanced by the horizontal friction. This allows a decoupling of the smaller forces from the larger ones.

On the other hand, in the case of single particles oscillating in the plasma sheath, all the forces (gravitation, neutral gas friction, ion drag, electric field

force, and thermophoresis) act on the vertical direction, and the action of the small ones (thermophoresis and ion drag) can not be decoupled from the action of the dominant gravitation and electric field forces.

In conclusion, the choice of the dominant forces strongly depends on the experimental configuration. The action of various forces will be analyzed in Chapter 3 and 4 for the above mentioned situations: first, trapped particles in the plasma sheath of an RF capacitive discharge and second, free-falling particles through a long RF plasma column.

2.4 Vertical Oscillations of Particles in the Plasma Sheath

2.4.1 Introduction

Among the various motions of particles in dusty plasmas like waves, wakes, or drifts, the grain oscillations in the sheath have focused a high interest and have been considered in detail in a number of publications [125, 68, 126, 82, 44, 127, 128, 53, 45, 83, 47, 129, 104, 130, 131]. The most interesting types of oscillations are the vertical oscillations of single particles [125, 68, 126] and the horizontal dust lattice waves (DL) [82, 44]. Such experiments allow the determination of fundamental parameters of these systems, namely the particle charge [4, 53, 45, 132], or the measurement of the coupling parameter within plasma crystals.

In the earliest experiments, it has been generally assumed that the particle charge is constant, independent on the position in the sheath, and the electric field within the sheath increases linearly from the sheath edge. These models are able to provide quite accurate results in the case of linear particle oscillations [4, 132, 133, 57]. Nevertheless, they are not sufficient for the study of nonlinear resonances. Recently, a new nonlinear approach considering the electric field distribution in the sheath and/or a position-dependent particle charge model have been developed [55, 56].

The aim of this section is to give an overview over the different vertical oscillation modes, starting with purely linear resonances, going to parametric resonances, and, most interesting for our investigations, finally to the nonlinear resonances of the particles in the plasma sheath.

2.4.2 Small Amplitude Resonances

The particles are levitated at a certain level in the plasma sheath due to the balance of the weight force and electric field force. The static equilibrium is defined by (see Fig. 2.8)

$$m_p g = Q_p E(x) \tag{2.46}$$

with Q_p and $E(x)$ the time-averaged particle charge and electric field in the sheath.

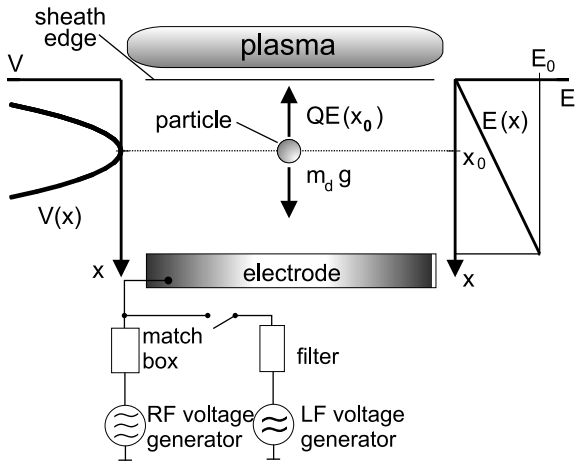

Figure 2.8: *Equilibrium of the particles in the plasma sheath. The linearly increasing electric field and the constant particle charge determine a parabolic potential well for an oscillating particle.*

For an oscillating particle, the friction force is also considered. The excitation force is taken into account as an additional force of the form $F = F_{exc}\sin(\omega t)$. Thus the equation of motion writes as

$$m_p\ddot{x} + m_p\beta\dot{x} = Q_pE(x) - m_pg + F_{exc}\sin(\omega t), \tag{2.47}$$

with β the friction constant normalized to the particle mass (see Section 2.3). This is the general equation of motion for an oscillating particle. Thermophoresis and ion drag are usually neglected in these situations since they are small compared to the gravitation and act in the same vertical direction (see Section 2.3). With the assumption of a constant charge Q_0 and a linearly varying electric field $E(x) = E_0 + E_1x$, the potential profile for the oscillating particle is determined by integrating the general equation of motion

$$U(x) = \frac{E_0Q_0}{m_p}x + \frac{1}{2}\frac{E_1Q_0}{m_p}x^2. \tag{2.48}$$

The resulting potential well has a parabolic shape (see Fig. 2.8) and the particle exhibit a linear resonance. The equation of motion can then be written as

$$\ddot{x} + \beta\dot{x} + \omega_0^2x = \widetilde{F}\sin(\omega t), \tag{2.49}$$

with $\omega_0^2 = -Q_0E_1/m_p$ defining the resonance frequency and $\widetilde{F} = F_{exc}/m_p$ the normalized excitation amplitude. $Q_0E_0 = m_pg$ is the condition of equilibrium so it is not included into the equation of motion. Replacing the electric field by the ion density in the sheath via Poisson's equation (see Section 2.1), the resonance frequency is

$$\omega_0^2 = \frac{Q_pn_i(1-\alpha)e}{\varepsilon_0m_p}, \tag{2.50}$$

where n_i is the ion density at the particle position and α is the ratio of electron to ion density.

From the analysis of the resonance curve of a particle, the resonance frequency and, consequently, the particle charge to mass ratio can be deduced when the plasma parameters are known. This procedure of measuring the charge has been first applied by [4]. There, the particle oscillations have been driven by modulating the RF power with a low frequency sine-wave.

This principle has been later refined using a non-invasive method of exciting the particle oscillations by a modulated laser beam focused on the particle surface [132]. The light pressure is strong enough to excite the oscillations.

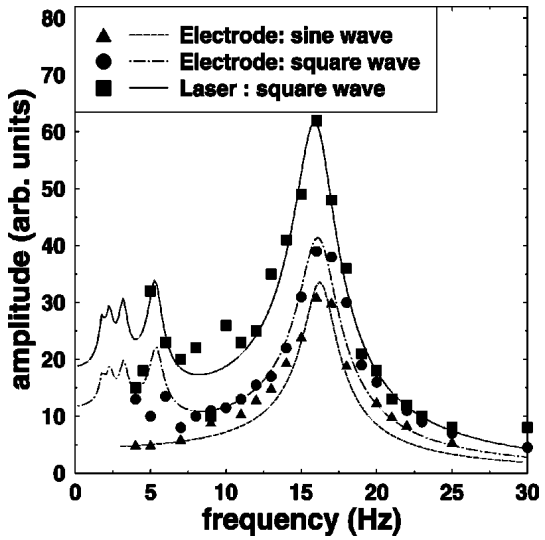

Figure 2.9: *Resonance curves of a single particle. The oscillations are excited using three different techniques: the RF modulation using either a periodical square-wave, or a sine-wave, and the square-wave modulated laser focused on the particle. (From [132])*

Fig. 2.9 shows the resonance curves for the same particles when the oscillations are driven using three different techniques, namely RF voltage modulation either with a periodic square-wave, or with a sine-wave, and by laser excitation with "on" and "off" square-wave modulation. The results are in a good agreement, and show the same resonance frequency. The square-wave modulation of the RF and of the laser produces additional resonances at $\omega_0/3$, $\omega_0/5$, etc. With this method, the earlier results in [4] have been confirmed, and it was shown that the RF power modulation does not perturb the sheath structure, or the measured particle charge.

2.4.3 Parametric Excitation

Experiments with wire excitation at low gas pressures [133] have demonstrated that it is necessary to consider the periodic modulation of the resonance frequency when using invasive excitation techniques due to the periodic variation of the

sheath position. With the modulation of the resonance frequency the equation of motion becomes

$$\ddot{x} + \beta\dot{x} + \omega_0\Big[1 + \epsilon\cos(\omega t)\Big]x = -g + \widetilde{F}\sin(\omega t). \tag{2.51}$$

This is the well-known Mathieu equation [134] describing the parametric excitation, which allows excitation of sub- and super-harmonics of the resonance frequency ω_0 [133] (see Fig. 2.10). It usually occurs at relatively large excitation amplitudes.

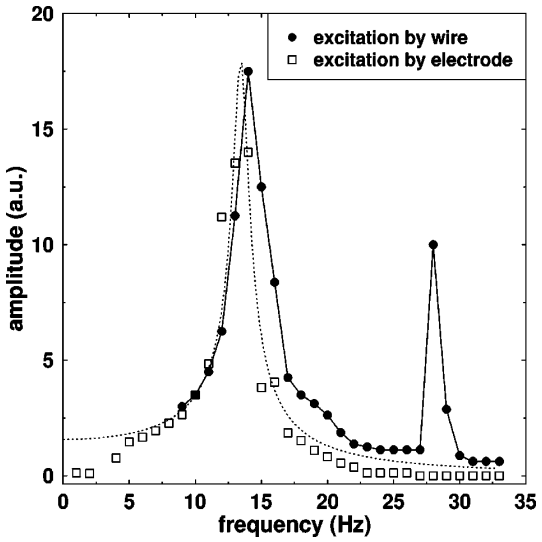

Figure 2.10: *Vertical amplitude of oscillating particles in 2D monolayers for two excitation techniques: RF modulation, and a biased wire below the particles. The peak at $2\omega_0$ occurs only for the wire excitation. (from [133])*

The observed resonance curves are shown in Fig. 2.10 for two excitation methods, namely RF power modulation and low frequency voltage modulation on a wire below the particles. The main resonances corresponding to ω_0 agree very well with each other. Additionally, a peak at the second harmonic frequency occurs in the case of wire excitation (see [133]). Thus this experiment demonstrates the parametric character of the excitation technique where a local, periodic perturbation of the sheath is applied.

Theoretical considerations on this subject can be found in [135], in a simulation approach.

2.4.4 Nonlinear Oscillations

As shown in Section 2.1, the time-averaged ion and electron densities vary within the sheath (see Fig. 2.3). Therefore, for a full description of the oscillations, the variations of the electron and ion densities have to be taken into account. These variations might lead to a non-linear electric field and to position-dependent

charging currents on the particle surface, leading to the idea of a position-dependent particle charge. Here we assume that the electric field and the particle charge can be described by polynomial functions of position

$$\begin{aligned} Q_p(x) &= Q_0 + Q_1 x + Q_2 x^2 + Q_3 x^3 \\ &= \tilde{Q}_0 + \tilde{Q}_1 X + \tilde{Q}_2 X^2 + \tilde{Q}_3 X^3 \end{aligned} \tag{2.52}$$

$$\begin{aligned} E(x) &= E_0 + E_1 x + E_2 x^2 + E_3 x^3 \\ &= \tilde{E}_0 + \tilde{E}_1 X + \tilde{E}_2 X^2 + \tilde{E}_3 X^3. \end{aligned} \tag{2.53}$$

At the sheath edge X=0, $E(X)$=0, so $\tilde{E}_0$=0. It is important to make a distinction between x, which is the so called "local coordinate" relative to the particle equilibrium position, and the "global coordinate" X measured from the sheath edge. The equation of motion becomes nonlinear (in the local reference system) by including higher order terms

$$\ddot{x} + \beta\dot{x} + C_1 x + C_2 x^2 + C_3 x^3 + \ldots = \frac{F_{exc}}{m_p}\cos(\omega t). \tag{2.54}$$

Here $C_0 = Q_0 E_0 = m_p g$ is the condition of equilibrium and does not have to be taken into account in the general equation of motion. The coefficients C_1, C_2, and C_3 are combinations of electric field and charge coefficients with

$$\begin{aligned} C_1 &= (Q_0 E_1 + Q_1 E_0)/m_p \\ C_2 &= (Q_0 E_2 + Q_1 E_1 + Q_2 E_0)/m_p \\ C_3 &= (Q_0 E_3 + Q_1 E_2 + Q_2 E_1 + Q_3 E_0)/m_p. \end{aligned} \tag{2.55}$$

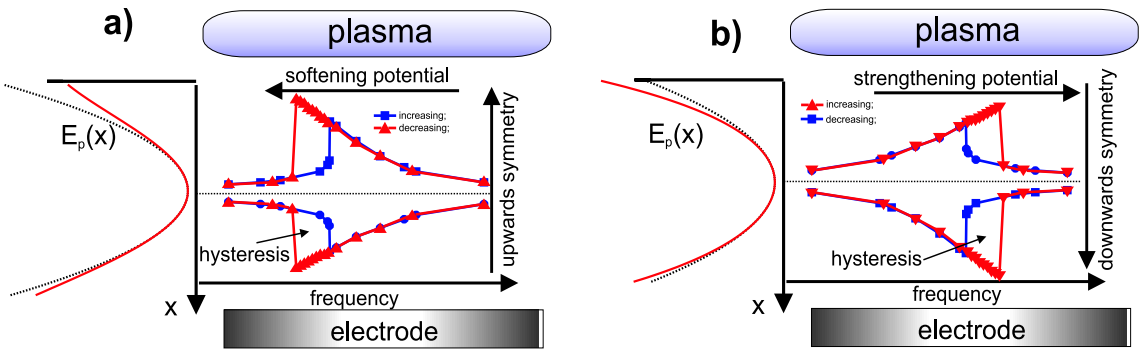

Figure 2.11: *The influence of the shape of the potential well on the resonance curve of a particle. a) $C_2 > 0$, $C_3 < 0$; b) $C_2 < 0$, $C_3 > 0$. The dotted curve indicates a parabolic well.*

By integrating the equation of motion in the local system, the nonparabolic potential energy of a particle in the sheath is derived

$$U(x) = C_0 x + \frac{C_1}{2}x^2 + \frac{C_2}{3}x^3 + \frac{C_3}{4}x^4 + \ldots \quad . \tag{2.56}$$

The particle oscillates in this potential well, so the oscillation properties reflect the features of the potential curve. Fig. 2.11 shows the influence of the potential shape on the resonance curves. If C_2 and C_3 are zero, the particle oscillates in a parabolic potential well (the black dashed line), leading to a linear resonance, with the frequency determined by C_1, as described in Subsection 2.4.2. C_2 defines the asymmetry of the potential well and consequently determines the up/down asymmetry of the particle oscillation in the sheath. If $C_2 > 0$, the particle will exhibit larger upwards excursions than downwards (Fig. 2.11a) and vice versa (Fig. 2.11b). Finally, C_3 determines the softening (Fig. 2.11a), or strengthening (Fig. 2.11b) of the potential well respectively for higher oscillation amplitudes. This results in the bending of the resonance curves towards lower or higher frequencies respectively. A hysteresis between the curves for increasing/decreasing frequencies occurs in the direction of decreasing frequency for a softening potential (Fig. 2.11a) and in the direction of increasing frequency in the case of strengthening well (Fig. 2.11b).

From experiments on particle oscillations (Chapter 3), the resonance curves of the particles are determined. The observed asymmetry and bending of the curves can be related to nonlinear coefficients of the potential well. The goal of this analysis is the determination of charge and electric field variation with the position in the sheath.

3 Nonlinear Vertical Oscillations of Particles as Diagnostic

In this chapter the nonlinear vertical oscillations of single particles is presented. From this, a diagnostic method for studying the particle charge and the structure of the electric field in the sheath is derived. The experimental results are interpreted in terms of the nonlinear variation of the particle charge with the position in the sheath. Also the role of the nonlinearity of the electric field is studied. The sheath model of Liebermann and Lichtenberg has been here employed for comparison with the experimental data.

3.1 Introduction

As already mentioned in Section 2.4, a number of experiments have been carried out on vertical particle oscillations in the plasma sheath [4, 132, 133, 57]. Most of them use particle oscillations as diagnostics under the assumptions of constant particle charge and linearly increasing electric field from the sheath edge into the sheath [4, 132, 133, 57]. More recent experiments on nonlinear particle oscillations have been carried out by Ivlev et al. [56, 55] and by Zafiu et al. [A.1]. Effects like bending and shifting of the resonance curves towards lower frequencies, hysteresis, and sub- or super-harmonics have been explained in [56] in a nonlinear approach for the electric field, assuming again a constant charge of the grain [56].

The influence of regular and stochastic charge variations on both horizontal and vertical particle oscillations have also been studied theoretically by [55]. Ivlev et al. have shown the way how the regular charge fluctuations (position- or time-monotonically dependent) can lead to instabilities only in the vertical oscillations, while the stochastic fluctuations (due to the random charging collisions of the particle with charge carriers) result in oscillation instabilities on both vertical and horizontal direction (dust lattice waves).

Self excited vertical oscillations have been observed in the sheath at very low pressure and described in terms of finite charging time by Nunomura et al. [104]. In these experiments, the delayed particle charging process leads to a charge which is not in equilibrium with the local plasma conditions. Thus an energy gain over a full oscillation cycle can occur, which compensates the dissipation due to friction.

In our experiments we have described the nonlinear particle oscillations in

the plasma sheath in a nonlinearly position-dependent approach for the particle charge, assuming either a linearly increasing or a parabolic electric field in the sheath. This model is more general than the afore mentioned one of Ivlev et al. [56], since it does not overimpose any limitations on the charge or on the electric field distribution.

3.2 Experimental setup

Melamine Formaldehyde (MF) single spherical particles of d=9.47 μm and d=12.07 μm and Polymethilmethacrylate (PMMA) particles of d=20.02 μm have been injected into a capacitively coupled RF discharge at a pressure of 5.8 Pa in Helium. The lower electrode is powered, while the rest of the discharge vessel is grounded. The particles are observed from top in the scattered light of a horizontal laser sheath and from the side using a digital high speed camera (up to 200 frames per second) when illuminated by a vertical laser sheath. Vertical oscillations are induced by sinusoidal, small amplitude modulation of the RF power on the bottom electrode (5 V_{pp} for d=9.47 μm, 10 V_{pp} for d=12.07 μm, and 23 V_{pp} for d=20.02 μm). This kind of modulation does not affect the structure of the time-averaged plasma sheath, as shown by Homann et al. under similar conditions [132] (see Section 2.4).

Besides the above mentioned particle sizes used for studying the vertical oscillations, very small grains of d=0.93 μm have been injected to mark the sheath edge. Due to their very low weight, these particles cannot penetrate far into the sheath, and can thus be used as an indicator of the sheath edge. It was assumed here that the ion drag force is negligible compared to the weight even for these very small particles.

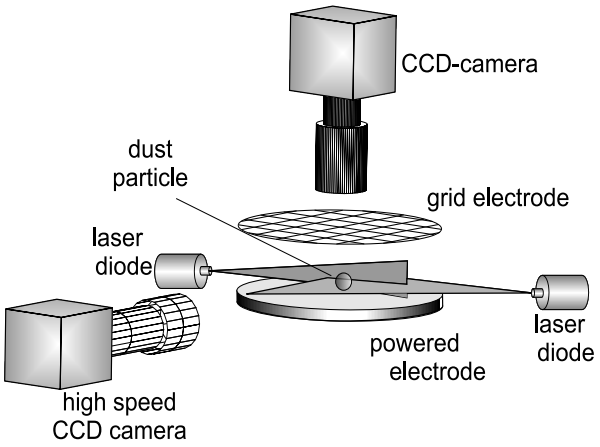

Figure 3.1: *General view of the experimental setup.*

3.3 Experimental Results

For small excitation amplitudes, linear harmonic oscillations have been observed. Increasing the excitation amplitude, however, the particles clearly exhibit nonlinear resonance characteristics (see Section 2.4). The resonance curves for the 9.47 μm and 20.02 μm particles are shown in Fig. 3.2 as upward/downward elongations from the equilibrium position. One can observe that in both cases the resonance curves are bent and shifted towards lower frequencies. The amplitude curve for increasing frequency rises relatively slowly until a point where it "jumps" to a much higher value, then it decreases monotonically as the frequency is further increased. For decreasing frequency, the same amplitude values as for increasing frequency are reached until a sharp "jump down" at a certain frequency value, smaller than that for the "jump up" point. The hysteresis zone between the curves for increasing and decreasing frequencies increases with the excitation amplitude and is strongly dependent on the particle size. Another characteristic is the asymmetry between upward/downward elongations. The smaller (9.47 μm) particles exhibit a larger upward elongation than downward, while for the larger (20.02 μm) particles the asymmetry direction is opposite.

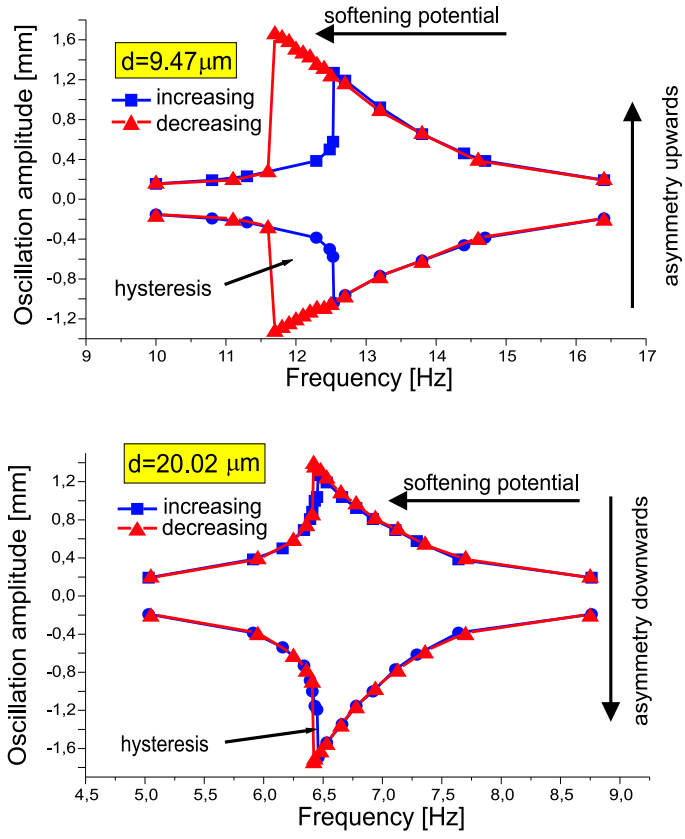

Figure 3.2: *Nonlinear resonance for 9.47 μm and 20.02 μm particles as upward and downward elongations from the equilibrium position x=0.*

According to the nonlinear oscillation model presented in Section 2.4, the bending and shift of the resonance curves towards smaller frequencies can be translated in terms of softening of the potential curve. The oscillation asymmetry is an indication of the asymmetry of the potential well. The change in the asymmetry direction from the 9.47 μm to the 20.02 μm particles suggests a similar change in the potential curve. Additionally, the hysteresis between increasing and decreasing frequency is an indication of non-equilibrium transitions in the oscillation regime, characteristic for a non-parabolic potential well.

3.4 Data Processing

Here the model of nonlinear oscillations presented in the Section 2.4 has been employed to determine the coefficients C_1, C_2, and C_3 from the experiment, for a full determination of the potential well of the oscillating particle. The calculation has been carried out in two ways. First, a trial solution [134]

$$x(t) = B_0 + A_1 \sin(\omega t) + B_1 \cos(\omega t) \tag{3.1}$$

has been assumed for the equation of motion

$$\ddot{x} + \beta\dot{x} + C_1 x + C_2 x^2 + C_3 x^3 + \ldots = \frac{F_{exc}}{m_p} \cos(\omega t). \tag{3.2}$$

Here we restrict ourselves to the three coefficients holding the main information, i.e. resonance frequency (C_1), oscillation/potential asymmetry (C_2) and weakening/strengthening of the potential (C_3). Higher orders are ignored.

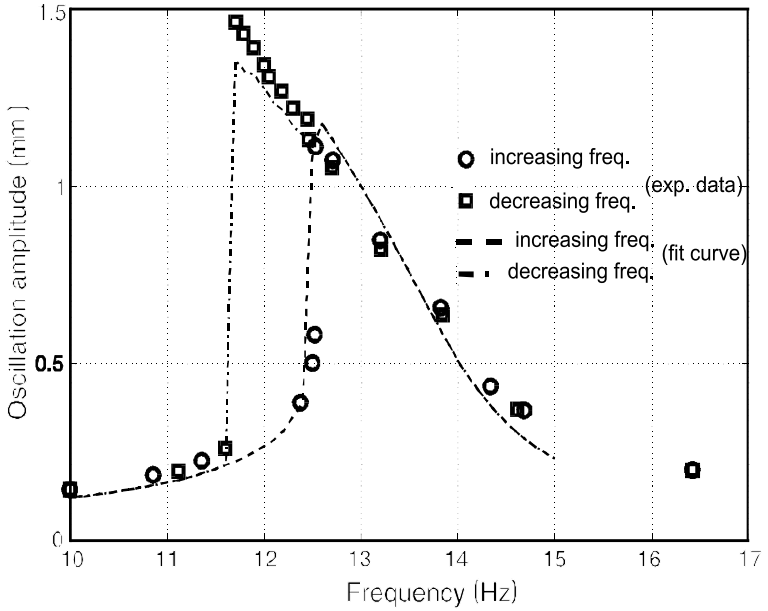

Figure 3.3: *Best-fit results of the nonlinear resonance curve for a 9.47 μm particle. Here, the average amplitude between upward and downward elongations is plotted.*

a (μm)	$C_1(s^{-2})$	$C_2(m^{-1}s^{-2})$	$C_3(m^{-2}s^{-2})$	$\beta(s^{-1})$
9.47	7200	$1.5 \cdot 10^5$	$-1.2 \cdot 10^9$	1.64
12.07	6200	$1 \cdot 10^5$	$-1.1 \cdot 10^9$	1.28
20.02	1900	$-5.1 \cdot 10^5$	$-6 \cdot 10^7$	0.78

Table 3.1: Best-fit-values for coefficients C_1, C_2, and C_3 and damping coefficient β.

This analytical solution (A.1) fits quite precisely the experimental resonance curves, but it is nevertheless unable to recover satisfactorily the hysteresis effect.

Therefore, the equation of motion has been solved numerically. This numerical solution reproduces all the features of the experimental resonance curves. The nonlinear coefficients C_1, C_2, and C_3 have been found by fitting the numerical solution to the experimental resonance curves (see Fig. 3.3).

Table 3.1 shows the values of the coefficients C_1, C_2, and C_3 obtained using this method, and the computed values for the normalized damping coefficient β. The change of sign of C_2 is in agreement with the change of oscillation asymmetry experimentally observed. This can be traced back to a change of asymmetry of the effective potential well from 9.47 μm to the 20.02 μm particles. The values obtained for C_3 are all negative, which corresponds to a softening of the effective potential well for all particle sizes.

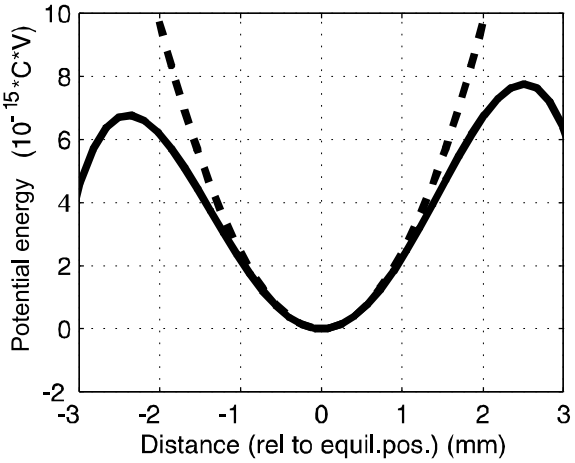

Figure 3.4: *Potential energy curve for the 9.47 μm computed using the values for C_1, C_2, and C_3 in comparison with an ideal parabolic potential.*

Using these coefficients, the potential energy curve of the particle can be calculated by integrating the general equation of motion (as shown in Section 2.4). Fig. 3.4 shows the potential energy curve for the 9.47 μm particles in comparison with an ideal parabolic potential defined only by C_1. An oscillating particle with a very high amplitude, larger than the distance to the local maxima of the potential well, would escape the potential trap and either gets lost towards the electrode, or moves only under the influence of gravity in the plasma direction.

3.5 The Sheath Model

Contributions of various order from both particle charge and electric field are contained in the nonlinear coefficients. Therefore their individual variations with the position is to be obtained from these coefficients for a complete analysis.

The system of equation (2.55) cannot be simply solved due to the large number of variables. Therefore some assumptions on the charge and electric field are necessary. The theoretical self-consistent model of Lieberman and Lichtenberg [81, 82] (see Section 2.1) has been employed here to determine the potential energy of a particle in the sheath.

Using various values for H, for the measured electron and ion temperature, and plasma density as input parameters to this model, the time-averaged electron and ion densities and the electric field distribution within the sheath have been determined. The charge on the particles is obtained from the balance of the OML ion and electron currents (accounting for the supersonic ion flow in the sheath, see Section 2.2 and [A.1]). The particle charge is found to vary quite strongly with the position in the sheath. The potential energy of the oscillating particles has been calculated and the coefficients C_1, C_2, and C_3 have been derived. The model input parameters have been chosen in order to recover the values for C_1, C_2, and C_3 found from experiment.

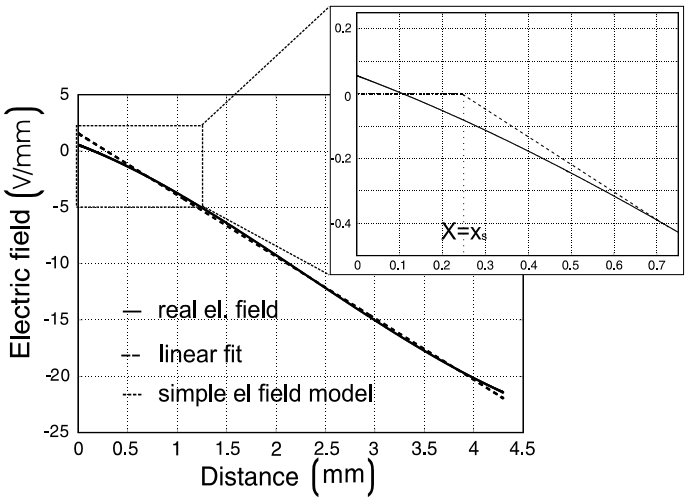

Figure 3.5: *a) Time-averaged electric field within the sheath provided by the Lieberman sheath model in comparison with a linear fit. In the expanded figure the assumption of a small zero-field plateau is sketched.*

Using this procedure, it has been found that the electric field increases almost linearly with the depth X from the sheath edge towards the electrode, as in Fig. 3.5. Only very close to the sheath edge, the electric field has a smaller slope. For simplicity of the analysis, the electric field has been modelled in the following way: from the sheath edge ($X = 0$), the electric field has a small plateau with E=0 until the "turning point" (at $X = x_s$). From this point on, the field increases linearly with the distance in the sheath $E = \tilde{E}_1(X - x_s)$.

d (μm)	$\tilde{Q}_0$(e)	$\tilde{Q}_1$(e/m)	$\tilde{Q}_2$(e/m^2)	$\tilde{Q}_3$(e/m^3)
9.47	$1.10 \cdot 10^4$	$-7.18 \cdot 10^6$	$4.42 \cdot 10^9$	$-8.92 \cdot 10^{11}$
12.07	$2.67 \cdot 10^4$	$-1.98 \cdot 10^7$	$1.06 \cdot 10^{10}$	$-1.93 \cdot 10^{12}$
20.02	$6.86 \cdot 10^4$	$-2.64 \cdot 10^7$	$6.24 \cdot 10^9$	$-6.34 \cdot 10^{11}$

Table 3.2: Charge coefficients in the "absolute coordinate system".

3.6 Results

Using the linear electric field found from the sheath model, the potential drop has been determined by integration over the electric field between the sheath edge and the electrode position at x_{max} determined by the position of the 0.93 μm particles

$$\int_{x_s}^{x_{max}} E(X)dX = V_{plasma} - V_{bias}. \tag{3.3}$$

This potential drop has to be the same as the difference of the plasma potential V_{plasma}=32.5 V and the electrode self-bias V_{bias}=-45.7 V. The slope of the electric field has been calculated as $\tilde{E}_1$=4.10×10^6 V/m^2 (see Fig. 3.6). From the coefficients of the electric field $\tilde{E}_1$, and $\tilde{E}_2$=0, the charge coefficients in the "global" reference system have been deduced. Table 3.2 summarizes the charge coefficients for the three particle sizes. At this point, the main objective of this analysis, namely the determination of the position-dependent particle charge and the electric field distribution in the plasma sheath has been reached.

Since the charging process is a feature of the plasma sheath, it involves the same mechanisms for all three particle sizes. Therefore, it is reasonable to introduce a "universal charging function". Employing the charging model of the spherical capacitor for the grains, we can split the charge of the grain into the geometrical factor $4\pi\epsilon_0 R$ and the floating potential $\Phi_p(X)$ which depends only on the charging process in the sheath. Therefore the floating potential $\Phi_p(X)$ can be chosen as charging function. The value of x_s=0.25 mm has been chosen for the best agreement of the floating potential curves for all three particle sizes. Nevertheless, Fig. 3.6 shows that the floating potential curves are not the same for all the particles. For d=9.47μm and d=12.07μm, the curves agree quite well, but for the largest particles (d=20.02μm), the floating potential curve is shifted.

Since in similar experiments of Ivlev et al. [56] the nonlinearity has been attributed exclusively to the electric field, different forms for the electric field have been chosen for comparison, whereas the particle charge is still described by a third order polynomial, i.e.

$$E(X) = \begin{cases} 0 & X \le x_s \\ \tilde{E}_1(X - x_s) + \tilde{E}_2(X - x_s)^2 & X > x_s. \end{cases} \tag{3.4}$$

$\tilde{E}_1$ is arbitrarily chosen between 0 and 4×10^6 V/m which corresponds to purely parabolic up to purely linear electric field profiles. $\tilde{E}_2$ is computed from the potential drop within the sheath. The maximum chosen value of $\tilde{E}_1$ is 4×10^6 V/m^2

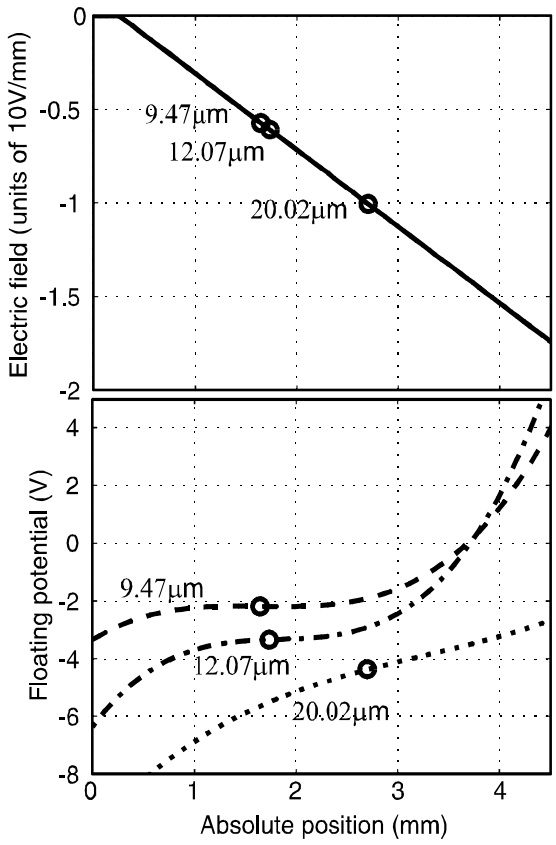

Figure 3.6: *Electric field within the sheath and particle floating potential; the symbols mark the equilibrium position of particles in the sheath.*

because for larger values, E_2 would become negative, resulting in an unphysical concave curvature of the electric field. The results for the electric field profile and for the particle charge are plotted in Fig. 3.7. As it can be observed, the floating potential curves corresponding to the largest particle are still shifted from the others for each set of electric field components. Particularly, Fig. 3.7c with $\tilde{E}_1 = 4 \cdot 10^6$ V/m^2 nearly corresponds to the case of linear electric field discussed above.

Since, by assuming a parabolic profile for the electric field, the general agreement is not improved over the situation of a linear variation of the electric field, we can consider that the linear model provides results which are accurate enough. The agreement problem for the floating potential curves is discussed in the following.

3.7 Discussion and Conclusions

Reviewing the main outcome of this analysis, the sign change of the asymmetry coefficient C_2 can be related to the change of slope for the floating potential curve from small to large particles. The weakening of the potential well for higher oscillation amplitudes, as deduced from the experimental resonance curves, can

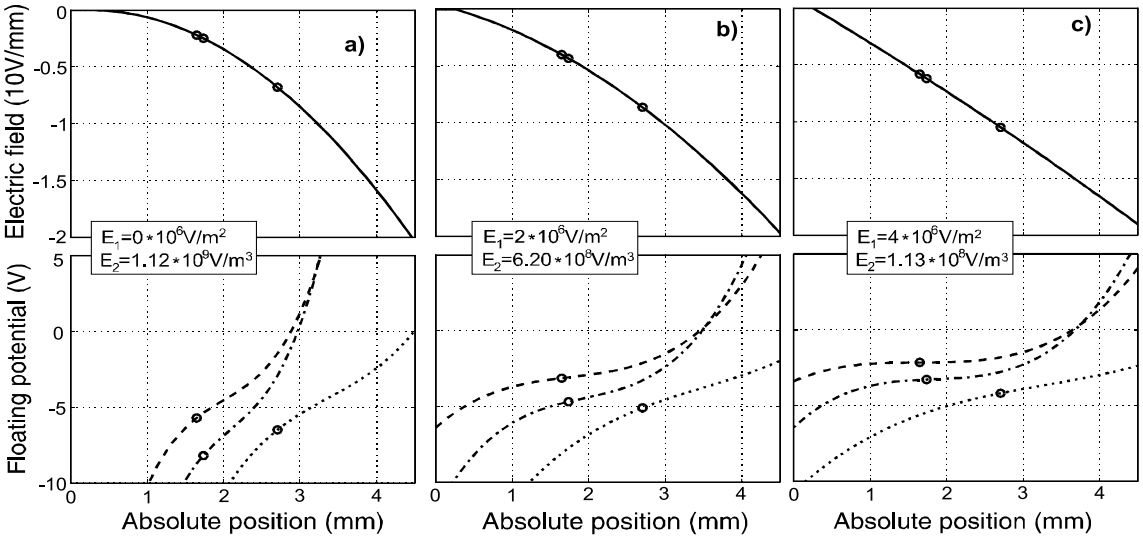

Figure 3.7: *Electric field within the sheath and the floating potential on the particle E_1. The symbols mark the equilibrium position of particles in the sheath*

be traced back to a negative value of C_3.

Similar decreasing trend of the negative floating potential can be observed for all three particle sizes. This decrease can be explained in terms of reduction of the electron density with the depth, which leads to a less effective charging process.

A quite good mutual overlap of the floating potential curves has been obtained for the 9.47 μm and 12.07 μm particles, for both electric field profiles (linear or nonlinear), but the curve corresponding to the 20.02 μm particle is somewhat shifted. This could have three different reasons:

First, the capacitive charging model assumed for particles into the sheath might be doubtful (A.1), according to Tomme et al. [57]. From their experiments with damped oscillations of dropped particles, a complicated variation of the charge with the particle radius has been deduced.

Second, an eventual perturbation of the ion current on the particle surface due to ion neutral collisions within the sheath might be taken also into account. The heavy particles reach an equilibrium position quite deep in the sheath, at a depth which is large compared to the mean free path for ion-neutral collisions. This alters the OML ion current flowing from the presheath and thus a less effective discharging due to the ions leads to a higher negative floating potential.

Third, a different microscopic charging process might occur for the material of the largest particles (they are made of PMMA, while the others are of MF). This could influence the floating potential of these particles.

Our results do not support the idea of nonlinear resonances produced only as a result of a nonlinear variation of the electric field in the plasma sheath with a constant particle charge (see A.1 for details).

Nevertheless, this model provides results which are in a good agreement with the experimental data and with the sheath model of Lieberman et al. [81], when

assuming a position dependent particle charge for both a linear or a parabolic electric field in the sheath. Other forces like thermophoresis or ion drag are neglected here due to the dominance of the electric field force and gravitation. Thus, the nonlinear oscillations of particles are used here as relatively precise diagnostic instruments for determining the most important parameters of the plasma sheath, namely the electric field and the floating potential of a spherical probe immersed into the sheath.

4 Falling Particles in the Plasma Bulk

So far, only the behavior of particles trapped in the plasma sheath in 2D structures has been discussed. The dynamics of 3D structures as a natural step forward in the study of dusty plasma is the subject of this chapter. We will give an overview on the behavior of falling particles in the plasma bulk. The dominant weight force is balanced by the friction force with the neutral gas, thus the action of less strong forces like ion drag and thermophoresis can be measured.

4.1 Introduction

Among complex plasma experiments, the formation of large, three-dimensional plasma crystals focused a strong experimental and theoretical effort during the last few years. The 3D systems are of higher relevance in the modelling of solid state physics at a macroscopic scale. It has been expected that once such crystals have been obtained, phenomena already studied in the 2D systems, like phase transitions, waves, and wakes, will be similarly accessible also in 3D systems. 3D dust clouds, which fill almost the whole plasma volume, have been obtained either under microgravity conditions [59], onboard the MIR and the International Space Station (ISS), or when the gravitation force is balanced by the thermophoretic force [63] in strong temperature gradients.

However, it was surprising to observe that even under such favorable conditions, the particles are pushed towards the plasma boundaries, while a considerable region in the plasma center remains free of grains [59, 136]. This particle-free region has been called "void" and it seems to be present in almost all experiments carried out so far and under all plasma conditions. Therefore, it is a severe impediment for obtaining real 3D plasma crystals.

For the explanation of this effect, theoretical calculations [62, 61] have been developed in parallel with simulations [137] and experiments [63], taking into account the action of the electric force, ion drag and thermophoresis on the particles. These forces are of great interest since are dominant after eliminating the gravitation force. Some of these works have even raised some doubt on the validity of ion drag equations by Barnes et al. [67] (see Section 2.3). Akdim et al. [137] or Khrapak et al. [138] proposed an enhancement of the ion drag force by a factor of 10 up to 40.

Therefore, to measure ion drag and thermophoresis under controllable and

reproducible conditions, we conceived a novel experiment. There, the particles have been dropped through a long plasma column, at high and low gas pressures. The gravitational force is balanced by the friction with the neutral gas, allowing the study of other more subtle forces.

4.2 Dynamical horizontal equilibrium

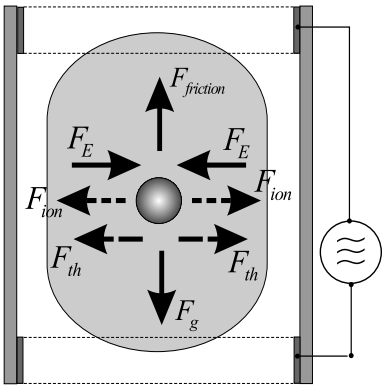

Figure 4.1: *Horizontal and vertical balance of the forces acting on a falling particle through a plasma column. The electric field acts as a confining force, whereas the ion drag and thermophoresis push the particles outwards.*

The most important forces which might act on a particle in the plasma have been described in Section 2.3. In a cylindrical discharge, the maximum power is deposited on the axis, therefore the maximum values of the ion, electron, and neutral gas temperatures, of the electron and ion densities and the highest electric potential are reached here. This is verified by the measurements of plasma parameters.

The radially decreasing plasma potential profile results in an electric field which accelerates the ions from the center towards the walls. Under the influence of this ion flow, the negatively charged particles feel a radial outward ion drag force as described in Chapter 2.3. This ion drag model is valid under the assumption of collisionless ions within the Debye sphere around the particle, which is not fully met here in the case of high pressure discharges (100 Pa to 200 Pa). For the negatively charged particle, the radial electric field in the plasma acts as a confining electric field force.

Since the gas temperature is highest in the center of the discharge, the plasma column is characterized by a negative radial temperature gradient. Therefore, the thermophoretic force acting on the grains is also oriented towards the walls.

Other plasma forces like the effect of polarization of the shielding sheath around the dust grain are neglected, since they play no role in the plasma bulk, which is characterized by low ion/electron flows and electric fields.

After this analysis, we can talk about a decoupling between the dominant gravitation acting in the vertical direction and the much smaller, horizontally

acting, plasma forces, allowing a discussion of the particle equilibrium on separate directions.

The dynamical equilibrium between the forces acting on the horizontal direction on a dust particle in the plasma can be written as follows (see Fig. 4.1)

$$F_{ion} + F_{thermo} - F_{el} = F_{frict\_x} + m_p \ddot{x}. \tag{4.1}$$

Here F_{ion} is the ion drag force, F_{thermo} is the thermophoresis, F_{el} is the electric field force and F_{frict} is the neutral gas friction force. When $F_{ion} + F_{thermo} < F_{el}$ the particles are focused towards the plasma center, otherwise they are expelled outwards. The expulsion effect is closely related to the formation process of voids in microgravity experiments. The terms on the LHS are determined by the plasma parameters and the particle charge, while those on the RHS can be directly measured from the analysis of the particle trajectories. Therefore, in the following analysis the sum on the LHS will be named generically "plasma force", and that on the RHS the "trajectory force".

4.3 Experimental Setup and Measurement Technique

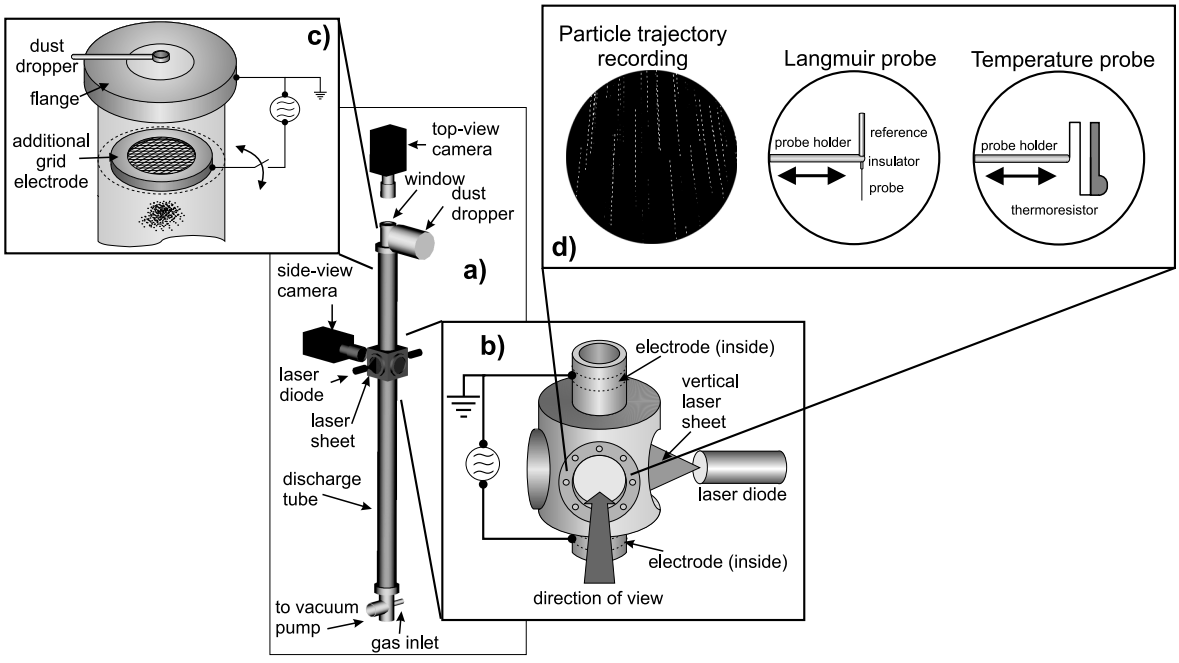

Figure 4.2: *a) Scheme of the experimental setup; b) magnified view of the observation level, in the middle of the plasma column; c) auxiliary discharge setup for cluster separation; d) magnified view of the observation window; the images of the falling particles are recorded here. In the same field of view, the plasma parameters are measured using a compensated Langmuir probe and a thermoresistor for measurement of the neutral gas temperature distribution.*

The experiments have been performed in a glass tube (see Fig. 4.2a) with a total length of 120 cm and a internal diameter of 50 mm. Monodisperse spherical particles made of melamine formaldehyde (MF) (between $a = 3.47$ μm and $a = 12.07$ μm diameter) and Polymethylmethacrylate (PMMA) particles of a=20.02 μm are dropped from the top of the tube, using a computer controlled dust dropper. The dust cloud is observed about 30 cm below the injection point. This distance allows the particles to reach a regime with a constant vertical velocity. The observation level (see Fig. 4.2b) is a cylindrical plastic connection with four windows, between two glass tubes, providing optimal image recording conditions due to the flat windows. The discharge is operated in Helium at high pressures (100, 150 and 200 Pa) and at low pressures (20 Pa), using two internal copper ring electrodes positioned in the glass tubes at upper and lower ends of the observation level. The lower electrode is powered with 0.8, 1.6, 2.0, 2.3 and 2.6 W (corresponding to 8, 11, 14, 17 and 20 W at the RF generator output) for the high pressure regime, and with very low powers below 0.5 W, (corresponding to 1 to 5 W at the generator output) at low pressure. The frequency of the applied RF voltage is 13.56 MHz. The upper electrode, as well as the metallic flanges positioned at the top and bottom of the glass tubes are grounded.

The falling particles are illuminated stroboscopically at 400 Hz (in the case of high gas pressure), and 3 kHz (at low pressure, due to the higher vertical velocity) through the side windows, using a thin vertical laser sheath with a power density of about 10 mW/mm^2 (see Fig. 4.2b). A camera with tunable frame rate has been used for image recording perpendicular to the laser sheath. This setup enables the observation of vertical cross-sections through the dust cloud. The stroboscopic illumination increases the time resolution of the image recording and it is suitable even in combination with standard video technique. The dust images have been recorded and processed on a PC. A long exposure regime of the camera (about 20 frames per second) has been used here, so that the particle trajectories look like dotted lines on the recorded images (see Fig. 4.2d).

The plasma parameters (electric potential distribution, electron temperature and plasma density) have been determined from Langmuir probe measurements. For each set of experimental conditions, probe measurements have been performed without dust, assuming that the presence of a small number of particles does not influence the plasma parameters significantly [A.1]. Radial profiles of the plasma parameters are recorded with a resolution of 1 mm. A compensated cylindrical probe, 6.90 mm long and 0.05 mm in diameter, with the compensation electrode 10 mm long and 0.8 mm diameter has been used here (see Fig. 4.2d).

The radial profile of the neutral gas temperature has been measured in order to determine the temperature gradient and therefrom, the thermophoretic force acting on the particles.

A temperature probe consisting of a thermoresistor (see Fig. 4.2d) has been used here for horizontal profile measurements with a spatial resolution of 1 mm (see [A.2] for details).

The errors deriving from the existence of clusters, as described in Chapter 2.3 affect not only the vertical, but also the horizontal velocity measurements. There-

fore, it is desirable to have most of the particle cluster separated into individuals.

For this aim, an additional RF funnel-shaped electrode with a grid bottom is positioned about 50 mm below the grounded vacuum flange (see Fig. 4.2c). The clusters are trapped for several seconds above the grid in order to "Coulomb-explode" due to their high negative charge. When this auxiliary discharge is turned off, the trapped particles are released and fall towards the main discharge (details in [A.2]). This ensures that only individual particles have been used in the analysis of the forces.

4.4 Experimental Results

The experiments have been performed at high and low pressures. Interesting differences have been observed in the particle behavior between these two pressure regimes.

4.4.1 Particle Trajectories

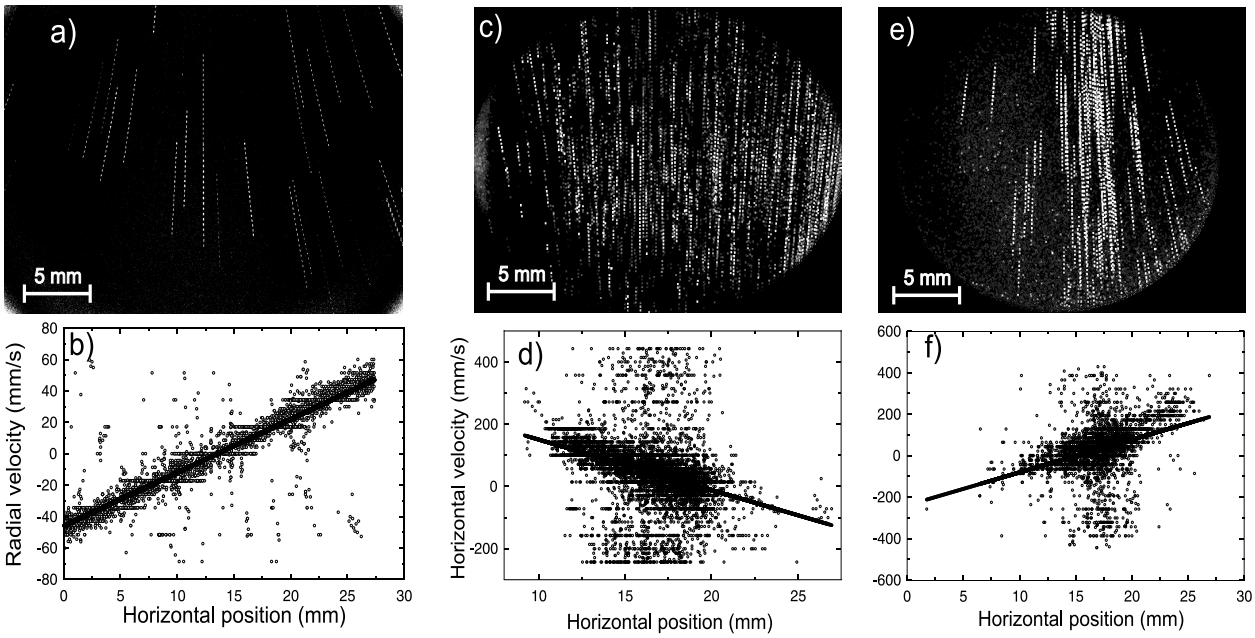

Figure 4.3: *Recorded particle images in the case of a) high pressure discharge, c) low power discharge at low pressure, and e) higher power discharge at low pressure. The measured radial/horizontal velocity of the particles is plotted in b), d), and f) respectively.*

The stroboscopic particle trajectories have been recorded and analysed. The precision in the determination of the particle motion velocity is limited by the pixel-resolution of the recorded images and by the existence of still unexploded particle clusters among the falling individual particles.

At high pressure discharges (150 Pa, 150 Pa, and 200 Pa), the particles are found to be always repelled from the plasma center, exhibiting a radial motion towards the discharge walls. Fig. 4.3a and b shows an example of the recorded particle image and the radial velocity distribution for a set of experimental conditions. The radial velocity of the particles increases almost linearly with the radial position, showing that the particles are accelerated outwards. The slope of the radial velocity increases as the power is increased (see [A.2] for details).

At low gas pressure (20 Pa), small particles (3.47 and 4.81 μm) exhibit an interesting behavior: when the discharge power is low (1 to 2 W), the particles are focused towards the discharge axis (see Fig. 4.3c and d), while for higher input powers (3 to 5 W), they are again expelled from the plasma center (Fig. 4.3e and f). Thus we can talk about a transition from the particle expulsion motion to a focussing one at a relatively sharp power boundary value which depends on the particle size [139]. The radial velocity of the particles still increases almost linearly for the both focussing and expulsion regimes. For larger particles (a=7.1 μm and a=12.1 μm in diameter) no focussing or expulsion have been observed in this power range, due to their larger inertia compared to the ion drag or electric field force. This transition from expulsion to focussing motion demonstrates how can be obtained void-free complex plasmas under microgravity conditions.

4.4.2 Plasma Parameters

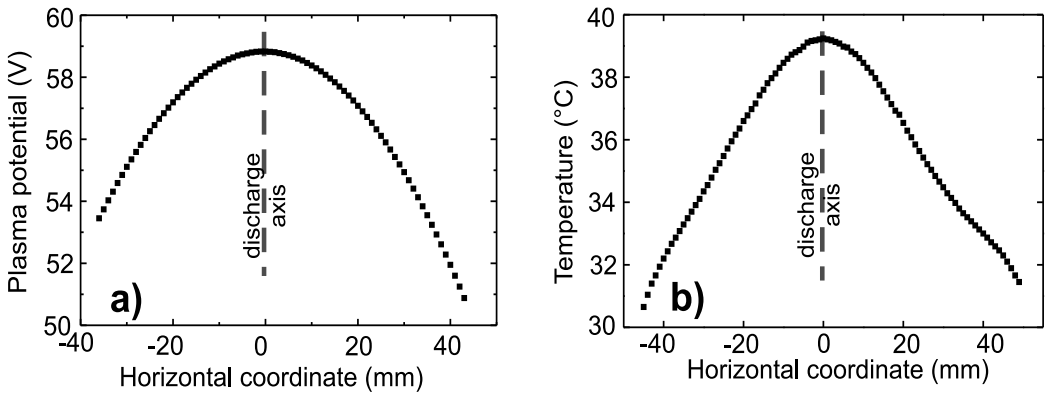

Figure 4.4: *Measured potential and neutral gas temperature profiles for a high pressure discharge (150 Pa).*

The electric potential distribution and the radial temperature profile of the neutral gas are plotted in Fig. 4.4, for the case of high pressure discharges. The potential distribution is parabolic and both curves are centered on the discharge axis, confirming the anticipated direction of the electric field force, ion drag and thermophoresis. In the case of low pressure experiments, these curves are similar.

4.5 Determination of Forces Acting on the Particles

In the equation describing the dynamical horizontal equilibrium, the "trajectory force" has to balance the "plasma force", so that the particle motion can be explained in terms of equilibrium of the aforementioned individual forces (electric field force, ion drag, thermophoresis and neutral gas friction).

From the particle trajectory analysis, the "trajectory force" in Eq. 4.1 has been determined. The horizontal acceleration of the particles (see [A.2])

$$\ddot{\vec{x}} = \frac{\partial \vec{x}}{\partial \vec{x}} \frac{d\vec{x}}{dt} = \dot{\vec{x}} \frac{\partial \vec{x}}{\partial \vec{x}}, \tag{4.2}$$

has been precisely measured from the radial velocity distribution of the particles.

The neutral drag coefficient computed using the measured vertical velocity (see [A.2]) has been used in the analysis of horizontal force balance. The "trajectory force" is then

$$\vec{F}_{traject} = m \left[\frac{d\dot{\vec{x}}}{d\vec{x}} + \beta \right] \dot{\vec{x}}. \tag{4.3}$$

It has to balance the plasma force F_{plasma}, namely the sum of thermophoresis, ion drag and electric field force.

The radial electric field distribution has been determined from Langmuir probe measurements. The particle charge is determined by the balance of the ion and electron currents provided by the OML theory [90]. Accounting for ion drift motion as by Whipple [91] does not alter the results significantly. Thus, the electric field force acting on a particle is

$$F_{el} = 4\pi\varepsilon_0 a \phi_{fl} \frac{d\phi_{pl}}{dx}, \tag{4.4}$$

with ϕ_{fl} the floating potential and ϕ_{pl} is the plasma potential determined from the probe measurements.

The ion drift velocity has been computed from the radial electric field of the plasma column by $\vec{u_i} = \mu \vec{E}$. μ is the mobility of singly ionized ions in the neutral environment of their parent gas and is given for helium by $\mu = 0.143$ kg m s^{-3}K^{-1} [119].

The ion drag has been computed using the equations of Barnes et al. [67] described in Section 2.3 assuming a collisionless regime of the ions.

The measured profile of the radial temperature of the neutral gas has been used for the determination of the thermophoretic force (see [A.2]).

4.6 Analysis of the High Pressure Experiments

In the case of high pressure experiments the particles always exhibit an expulsion behavior.

4.6.1 Discharge with Symmetric Temperature Profile

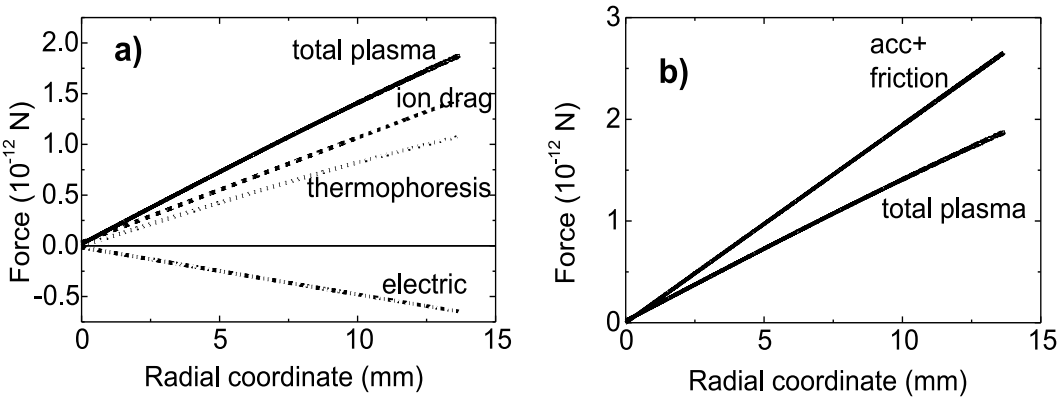

Figure 4.5: *a) Plasma force (thermophoresis + ion drag + electric field force), for high pressure discharge b) comparison of the measured "trajectory force" (acceleration + neutral friction force) with the total "plasma force".*

The results of of the force measurements are presented here in a radial analysis due to the symmetry of the potential and temperature profiles.

The comparison of the total trajectory and plasma forces in the case of high power discharges is presented in Fig. 4.5. The electric field force acts as a confining force, so it is counted negative, whereas the ion drag and thermophoresis point outwards. From this analysis, the trajectory and plasma forces agree within an error of 30%, and the measured trajectory force is slightly larger than the plasma force. The relative difference of trajectory to plasma forces is shown in Fig. 4.6 for various pressure and power conditions. It can be observed that for very low powers, the relative difference is negative, which means that the measured plasma force is slightly larger than the trajectory force. This can be related to relatively high measurement errors in estimating the neutral gas temperature an the plasma parameters (see [A.2] for details).

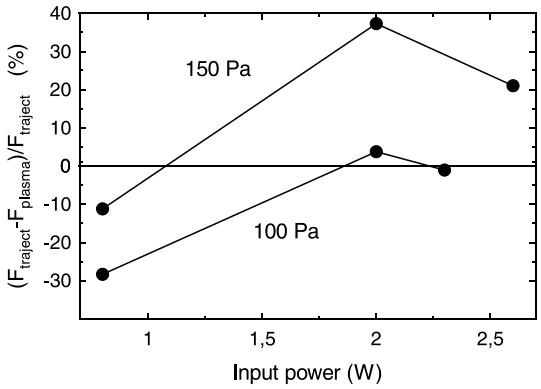

Figure 4.6: *Relative difference of trajectory and plasma forces.*

It is important to state here that the confining electric force is smaller than the sum of thermophoretic force and ion drag for all gas pressures in the range

100 to 200 Pa and for all input powers, while the thermophoretic force and the ion drag force are comparable. This shows that for high gas pressure, no confinement can be expected in this experimental configuration.

4.6.2 Discharge with Asymmetric Temperature Profile

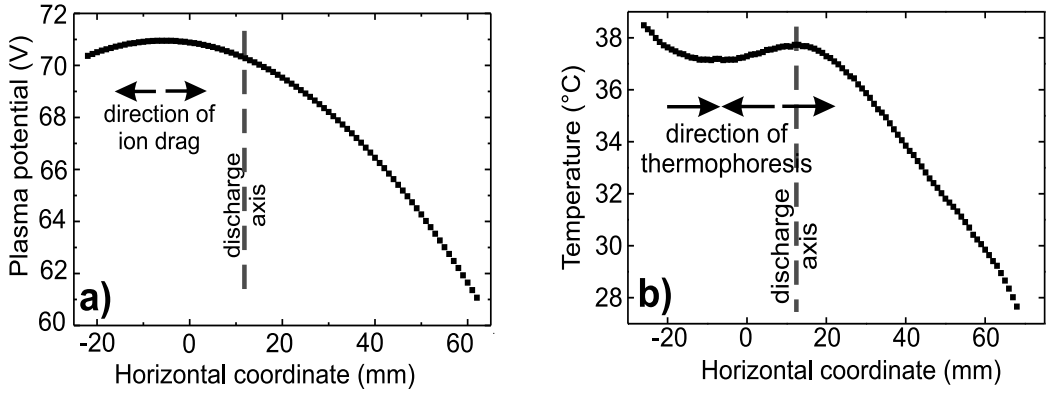

Figure 4.7: *Measured potential and neutral gas temperature profiles for a high pressure discharge (150 Pa) when the temperature profile is modified by a heat source.*

The experiments have been extended in order to establish regions in the plasma where ion drag and thermophoresis have opposite directions. Therefore the neutral gas temperature profile of the discharge has bee modified using an external heat source (a Peltier element) at the observation level (the left side in the recorded particle images).

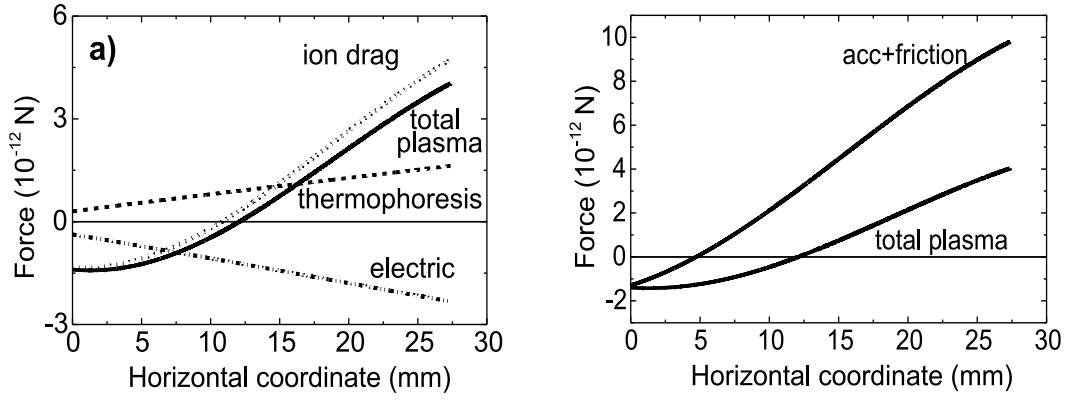

Figure 4.8: a) *Plasma force (thermophoresis + ion drag + electric field force), for high pressure discharge b) comparison of the measured "trajectory force" (acceleration + neutral friction force) with the total "plasma force", when the temperature profile is modified by a heat source.*

Polymethylmethacrylate (PMMA) particles ($a = 20.02$ μm diameter) are dropped through the same experimental setup using the same technique. The

particle trajectories are again analyzed and the horizontal and vertical velocities are extracted. Temperature and Langmuir probe measurements have been performed as in the symmetric case.

Fig. 4.7a and b shows the measured temperature profile and the plasma potential distribution. For this case the temperature profile is visibly modified due to the heat source (Fig. 4.7b). The plasma potential is also modified due to the use of quite large metallic pieces of the heat source in the vicinity of the plasma. The profile is still parabolic, but shifted towards the heat source (see Fig. 4.7a). The arrows indicate the direction of the ion drag, and of thermophoresis.

For this modified asymmetric temperature case, horizontal cartesian coordinates are used, with the origin corresponding to the left side of the recorded particle images. They should not be confused with the radial coordinate used in the symmetric case for high pressures.

In Fig. 4.8a and b, both the plasma force (ion drag, thermophoresis and electric force) and the trajectory force are plotted. Again, the confining electric force is smaller than the sum of thermophoresis and ion drag, while the thermophoretic force is smaller, but comparable to the ion drag. In this case the difference between the total trajectory and plasma forces is measured to be about 50%. This slightly lower agreement is a result of the fact that in this special case of asymmetric temperature and potential profile, systematic errors in the Langmuir probe and temperature analysis could not be compensated as in the symmetric case (see [A.2] for details).

4.6.3 Normalized Forces

A more elegant discussion of the horizontal force balance can be performed in a normalized form which depends only on a small number of easily measurable quantities [139]. Here it was assumed that the floating potential on a dust grain can be approximated to $\phi_{fl} \approx 2T_e$ when $T_i \ll T_e$. Thus, all the forces are normalized to the geometric particle cross section $F_N = \pi a^2 n_i m_i u_i v_s$ (the significance of these notations is detailed in Chapter 2.3). The electric field force and the ion drag become

$$\widehat{F}_{el} = 8\Big(\frac{\lambda_D}{a}\Big)\Big(\frac{\lambda_D}{\lambda_{mfp}}\Big)\Big(\frac{1}{1+\alpha^2}\Big)^{1/2}, \tag{4.5}$$

$$\widehat{F}_{coll} = 1 + \frac{\pi}{2}\frac{T_e}{T_i}\frac{1}{1+\alpha^2} = \Big(\frac{b_c}{a}\Big)^2, \tag{4.6}$$

$$\widehat{F}_{coul} = 4\Big(\frac{\pi}{4}\frac{T_e}{T_i}\frac{1}{1+\alpha^2}\Big)^2\widehat{\Gamma} = 4\Big(\frac{b_{\pi/2}}{a}\Big)^2\widehat{\Gamma}, \tag{4.7}$$

with the normalized Coulomb logarithm

$$\widehat{\Gamma} = \frac{1}{2}\ln\frac{(\lambda_D/a)^2 + (b_{\pi/2}/a)^2}{(b_c/a)^2 + (b_{\pi/2}/a)^2}. \tag{4.8}$$

It can be observed that all the forces depend only on the parameters (λ_D/a), $(\lambda_D/\lambda_{mfp})$, (T_e/T_i), and $\alpha = u_i/v_{th}$.

The ratio of ion drag to electric forces $\chi = F_{ion}/F_{el}$ determines whether the particles are focused into the plasma center, or pushed outwards. Thus, if the above-mentioned ratio is $\chi > 1$, a particle expulsion is to be expected.

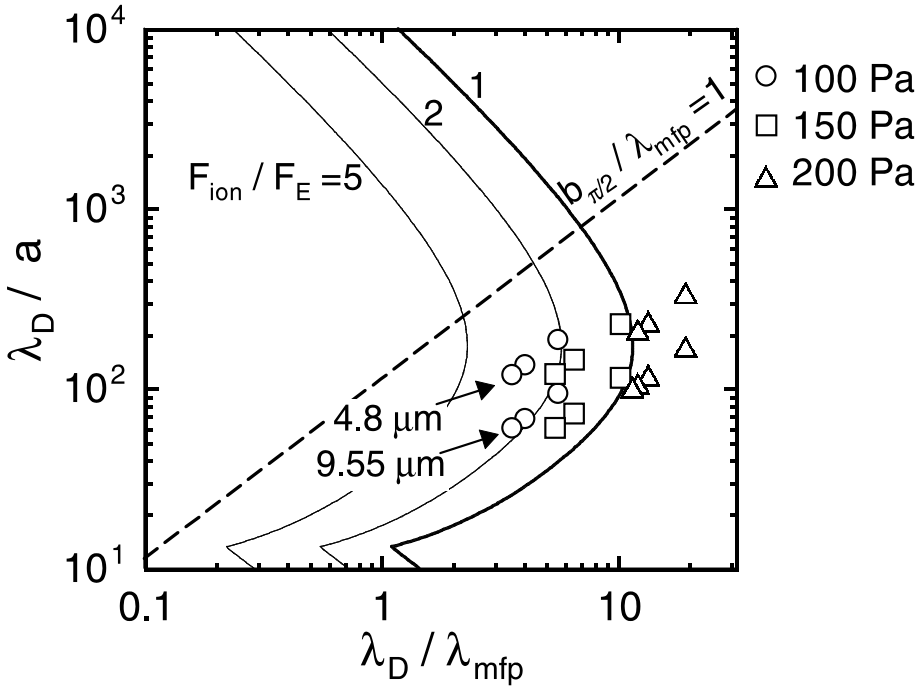

Figure 4.9: *Contour plot of the ion drag to electric field force ratio as function of the parameters λ_D/λ_{mfp} and λ_D/a. The other parameters are $T_e/T_i = 150$ and $\alpha = 0.2$. Data points for high pressure discharge are shown for particle sizes 4.81 μm and 9.55 μm. Under all conditions, the particles are expelled from the plasma.*

At high pressures, the falling particles exhibit always an expulsion motion. The points corresponding to the experimental data are plotted in Fig. 4.9 in the diagram of ion drag to electric force ratio. The experimental points corresponding to pressures of 100 Pa and 150 Pa fall mostly in a region where the ion drag alone exceeds the electric field force. For all the experimental data, the ratio λ_D/λ_{mfp} is larger than 3 due to the strong decrease of λ_{mfp} with increasing pressure. They lie on the diagram in the region where the ion mean free path is smaller than the Debye length and impact parameter for 90^0 ion deflection. Here, the collisionless assumptions for the ion drag model [67] are not fulfilled. So the fact that some experimental data lie in the region where $\chi < 1$, must be interpreted with care [139]. Nevertheless, even for the experimental points situated in the region with $\chi < 1$, if the thermophoretic force is taken into account, the balance of the plasma forces (electric field force, ion drag and thermophoresis) will be such that the particles are expelled from the plasma.

4.6.4 Discussion

Summarizing, the measured trajectory force has been compared with the plasma force (ion drag, thermophoresis and electric field force). A reasonable agreement between trajectory and plasma forces have been observed in both high pressure cases: for the radially symmetric plasma, the forces agree within 30%, while for the asymmetric case, the agreement is slightly worse, within 50%.

The highest mismatch of about 30% in the symmetric case for 150 Pa and 2.3 W can be correlated to the fact that for these experimental conditions the dust dropper has been freshly refilled, so that a huge number of particles were injected into the plasma column.

A high dust particle density considerably lowers the free electron density due to the negative charge attached to the particles. This affects both the charging process and the electric field distribution inside the plasma (see Section 2.2). The probe measurement has been performed in a particle-free plasma because it is practically impossible to record a complete plasma parameter profile within the few fractions of second when the particles fall. Therefore the influence of the reduced electron density of the plasma shall be discussed.

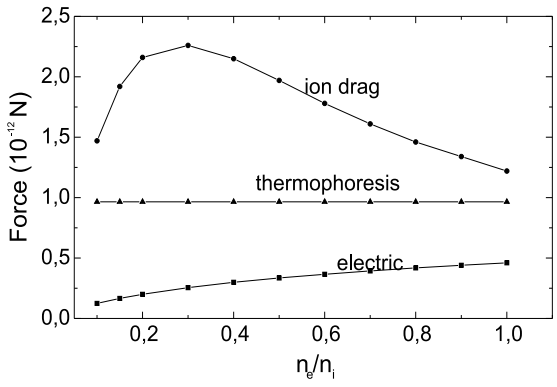

Figure 4.10: *Variation of thermophoresis, ion drag and electric force with the ratio n_e/n_i due to reduction of the electron density for high particle numbers.*

Fig. 4.10 shows the change of the ion drag, thermophoresis and electric force on the particles with variation of the n_e to n_i ratio (see [A.2] for details). With the ratio n_e/n_i a considerable change of the ion drag force and of the electric force can be observed. Thus the difference between the measured "plasma" and "trajectory" forces can be minimized. For 150 Pa and 2.6 W, a perfect match can be obtained for two different values $n_e/n_i = 0.6$ and $n_e/n_i = 0.15$. Therefore, a quantitative analysis of n_e/n_i from this results would be speculative.

With the increase of the dust density, the interparticle distance correspondingly decreases such that the mutual repulsion can have a considerable contribution to the total force which expels the particles out of the discharge. This effect is quite difficult to quantify because of the time-variable number of grains, and due to the space-variation of particle density inside the dust cloud.

4.7 Low Pressure Experiments

In contrast to the afore described effects in high pressure experiments, where the particles are always pushed out of the plasma, the particle behavior in a low pressure plasma changes with the input discharge power. Thus at low pressures, the particles exhibit both the expulsion effect for higher discharge power and a confining behavior when the discharge is low powered [139]. The transition from expulsion to attraction regime can be discussed in terms of horizontal force balance between the confining electric field force and ion drag. This discussion is carried out also in the normalized force system.

In the case of a low pressure discharge, the ion mean free path exceeds both the Debye length and the characteristic impact parameters of the ion drag force, so that the collisionless assumption for the ion drag model [67] is fulfilled.

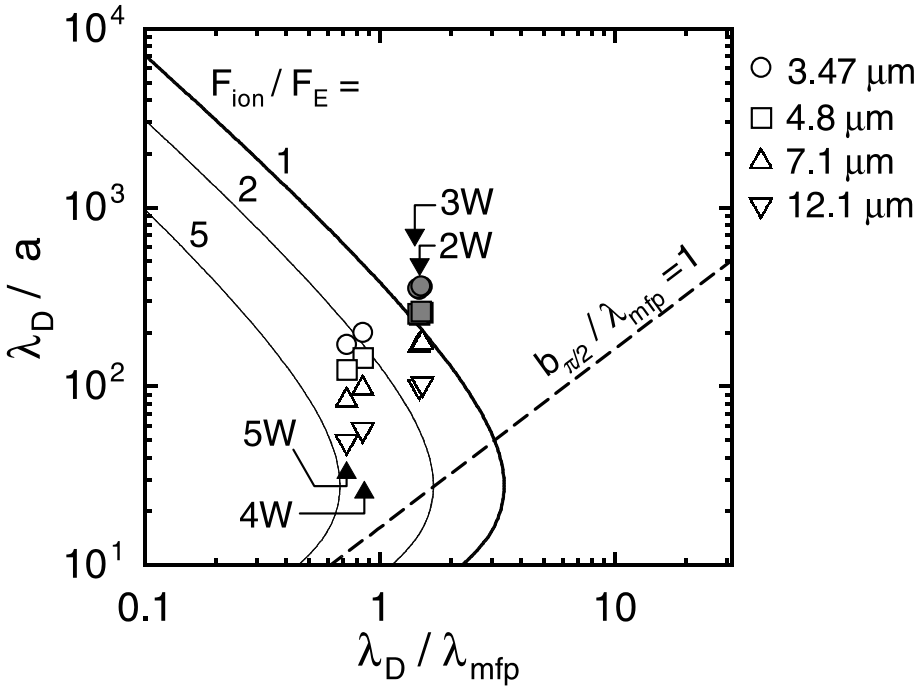

Figure 4.11: *Contour plot of the ion drag to electric field force ratio as function of the parameters λ_D/λ_{mfp} and λ_D/a. The other parameters are $T_e/T_i = 100$ and $\alpha = 2$. Data points for low pressure discharge are shown for particle sizes between 3.47 μm and 12.07 μm. The 3.47 μm and 4.81 μm particles exhibit either focusing or expulsion effects marked by solid and open symbols respectively.*

The diagram of this force ratio is shown in Fig. 4.11 as a function of λ_D/a and λ_D/λ_{mfp}. The ratio T_e/T_i is fixed to 100 due to the fact that at low pressures, the ions are slightly above the room temperature, and $\alpha = 2$, as estimated from the ion mobility. The symbols represent the experimental data for particles from 3.47 μm to 12.07 μm in a low pressure discharge. The open symbols characterize the situations when the particles are expelled, while the solid symbols are for particle focussing.

It is important to emphasize here that the points on the diagram corresponding to the focussing effect of the small particles are in the region with $\chi < 1$. The points representing higher powering conditions, where the particles are expelled, are in the region where $\chi > 1$.

Thus, a very good agreement between the experimentally observed effects and the theoretical predictions of the forces acting on the particles for given plasma parameters is obtained (see [139]).

For the large particles, for which no focusing or expulsion has been observed due to their large inertia, the corresponding points lie in the diagram in the expulsion region, at $1 < \chi < 5$. When the power is very high, above 15 W, even for these particles, an evident expulsion behavior can be observed.

4.7.1 Discussion

Summarizing, in the case of low pressure experiments, a transition from the particle expulsion behavior for high discharge powers to a focussing effect in the case of a low powers could be observed. Since the thermophoretic force is here very small compared to the ion drag force, this transition could be related to the dominance of the ion drag or electric field respectively. The change to focussing effect can be related to the transition process from "void" to "voidless" 3D particle structures in microgravity experiments. A good agreement between the measured effects and the theoretical models for thermophoresis and ion drag [67] has been obtained.

4.8 Summary

In conclusion, this novel approach of measurement using falling dust particles gives reliable qualitative and quantitative information on the forces acting on the grains in plasma when the influence of gravitation is reduced. For high pressure experiments, a quite good quantitative agreement of our results with the model of Barnes [67] concerning the ion drag force strength is observed, even though the collisionless assumption for ions is not met. In the case of low pressure discharge, the experimentally observed effects of focusing or expulsion are in a very good agreement with the balance of the electric field force and ion drag as predicted by Barnes et al [67]. Thus, our results do not support the idea of an enhancement of the ion drag force as proposed by [137, 138].

The expulsion effect of particles from the central regions of the plasma can be related to the mechanism of void formation in systems where the gravitation force on the grains is reduced using various methods. According to our observations, 3D void-free systems of particles might be obtained only under low pressure and discharge power conditions when using relatively small particles.

5 Summary and Conclusions

The forces acting on plastic micro-spheres introduced into a discharge plasma are crucial parameters for understanding and describing the dynamics of complex plasmas. The fundamental question of force balance has been studied in two experiments, under different conditions: when the particles are trapped in the non-equilibrium plasma sheath, and when freely falling through the plasma bulk.

The key results of the present thesis can be summarized as follows:

- large amplitude oscillations of particles in the plasma sheath are always found to shift the resonance frequency towards lower frequencies. This is a clear indication of a weakening of the potential well at large excursions from the equilibrium position of the particles

- close agreement with experimental findings is found for numerical integrations of the equation of motion, when a position-dependent particle charge is assumed. Thus the characteristics of particle resonances are consistent with a reduction of the particle charge with depth inside the sheath. A similar reduction of the particle charge was also concluded in [104] from the onset of unstable vertical oscillations of particles.

- the comparison of the self consistent sheath model of Lieberman-Lichtenberg [81, 82] with the measured nonlinear resonance curves leads to a linear variation of the electric field in the sheath. This observation is an independent confirmation of the parabolic shape of the time averaged electric potential reported in [140]. On the other hand, the conclusion of other authors [56] that the nonlinear resonance can be described by a particle with fixed charge moving in an anharmonic electric potential well, could be ruled out.

- a novel experimental approach was introduced for studying the weaker forces acting on microparticles. The underlying idea was to balance gravity by the neutral gas friction in a drop tube. In this way the microparticles could be studied in a quasineutral plasma environment, where no electric field was necessary for balancing the weight force, as in the case of levitation in the sheath.

- the decoupling of the weaker from the stronger vertical forces could be achieved due to the horizontal orientation of the weaker forces. In this way,

the balance of the horizontal forces could be derived with good sensitivity from the deviation of the particle trajectories from the vertical direction.

- the individual determination of ion drag force, thermophoretic force, and ambipolar electric field force was achieved by measuring the radial potential profile (yielding E(r)) and the radial temperature profile T(r). In this way, a quantitative comparison of the ion drag force with the standard model [67] became possible. The resulting forces are in general agreement with this formula. This finding is in contrast with recent theoretical results of other authors [137, 138], who require strong enhancements of the ion drag force over the standard value.

- the dominance of the ion drag force and thermophoresis over the electric field force under most experimental conditions results in a net force which expels particles from the plasma, in agreement with the ion drag model of Barnes et al [67]. A similar behavior is responsible for the formation of dust free regions in the center of complex plasmas (the so-called "void") under microgravity conditions. For a narrow set of experimental parameters (low power and low gas pressure) it was found that the force equilibrium is reverted and the particles are focused towards the center of the plasma. This is the first experimental hint which describes the regime where the void formation is expected to disappear.

- the force ratio of ion drag to electric field force could be conveniently summarized as a set of contour lines in a universal diagram. This diagram combines the standard normalized formulas for the forces [67] with an estimate of the electric field from ion mobility in the parent gas. The measured cases are found to fit well into this diagram, in particular, the change from expulsion to focusing in the case of low pressure experiments occurs close to the contour for ion drag to electric force balance. The results at high gas pressure were found to violate the assumption of collisionless ion trajectories, on which the standard formula for ion drag is based. This high pressure regime could be clearly separated by a borderline, where the ion mean free path equals the impact parameter for 90 degree deflections. Most of the high pressure data were found inside the expulsion regime of this diagram even by neglecting thermophoresis. A small set of data points that were found outside this regime would still lead to expulsion by considering thermophoresis. Nevertheless, the good agreement of the measured ion drag force with the standard model [67] even for the high pressure regime suggests that the ion drag force is not strongly modified by ion-neutral collisions, which are important at high pressures.

The results of the present thesis have contributed to questions of high actuality and fundamental importance in complex plasma research, in particular the charging behavior of particles in the plasma sheath and the void phenomenon. The observed reversal of the net force acting on falling particles is an experimental

hint for a necessary parameter range to suppress void formation. Nevertheless, it is not able to completely explain the structure of the void, or the sharp void boundary. Moreover, the agreement of the measured ion drag force with the standard model suggests further improvements of the simulations. Presently the simulations require a strong enhancement of the ion drag force to generate voids. Besides that, the experiments with particles in the sheath region have pointed out how complex plasmas differ from ordinary plasmas in the way that the electric field force QE is a linear force for electrons and ions, which have a fixed charge, but becomes inherently nonlinear for microparticles due to the temporal and spatial variability of Q.

The immediate experimental confirmation of the standard model for the ion drag force and the determination of its range of validity in the presence of collisions is of high practical importance for the modelling of dust transport in technological devices like etching reactors for microchip processing or fine film deposition for efficient amorphous solar cells. Likewise, this force is important for astrophysical situations, like in the plasma torus at Jupiter [141], or in planetary rings.

Bibliography

[1] J. H. Chu and L. I, Phys. Rev. Lett. **72**, 4009 (1994).

[2] H. Thomas *et al.*, Phys. Rev. Lett. **73**, 652 (1994).

[3] Y. Hayashi and K. Tachibana, Jpn. J. Appl. Phys. **33**, L804 (1994).

[4] A. Melzer, T. Trottenberg, and A. Piel, Phys. Lett. A **191**, 301 (1994).

[5] A. D. Taylor, W. J. Baggaley, and D. I. Steel, Nature **380**, 323 (1996).

[6] C. K. Goertz and G. Morfill, Icarus **53**, 219 (1982).

[7] G. E. Morfill, E. Grün, C. K. Goertz, and T. V. Johnson, Icarus **53**, 230 (1982).

[8] M. Horányi and T. E. Cravens, Nature **381**, 293 (1996).

[9] T. Nakano, in *Advances in Dusty Plasmas*, edited by P. K. Shukla, D. A. Mendis, and T. Desai (World Scientific, Singapore, 1997), p. 336.

[10] G. S. Selwyn, J. E. Heidenreich, and K. L. Haller, J. Vac. Sci. Technol. A **9**, 2817 (1991).

[11] L. Boufendi *et al.*, J. Appl. Phys. **73**, 2160 (1993).

[12] R. N. Nowlin and R. N. Carlile, J. Vac. Sci. Technol. A **9**, 2825 (1991).

[13] R. N. Carlile and S. S. Geha, J. Appl. Phys. **73**, 4785 (1993).

[14] A. Bouchoule *et al.*, J. Appl. Phys. **70**, 1991 (1991).

[15] A. Bouchoule, Physics World 47 (1993).

[16] G. S. Selwyn, J. Singh, and R. S. Bennett, J. Vac. Sci. Technol. A **7**, 2758 (1989).

[17] A. Bouchoule, *Dusty plasmas: physics, chemistry, and technological impacts in plasma processing* (John Wiley & Sons Ltd, New York, 1999).

[18] F. Verheest, *Waves in dusty space plasmas* (Kluwer Academic Publ., Dordrecht, 2000).

[19] C. K. Goertz, Rev. Geophys. **27**, 271 (1989).

[20] C. K. Goertz, *Staub–Plasma–Wechselwirkungen*, Chap. 14.

[21] U. de Angelis, Physica Scripta **45**, 465 (1992).

[22] N. A. Clark, A. J. Hurd, and B. J. Ackerson, Nature **281**, 57 (1979).

[23] P. Pieranski, Contemp. Phys. **24**, 25 (1983).

[24] C. A. Murray, W. O. Sprenger, and R. A. Wenk, J. Phys.: Condens. Matter **2**, SA 385 (1990).

[25] H. Löwen, Physics Reports **237**, 249 (1994).

[26] G. Nägele, Physics Reports **272**, 215 (1996).

[27] D. G. Grier and C. A. Murray, J. Chem. Phys. **100**, 9088 (1994).

[28] H. Löwen, Phys. Bl. **51**, 165 (1995).

[29] M. Schmidt and H. Löwen, Phys. Rev. Lett. **76**, 4552 (1996).

[30] J. C. Crocker and D. G. Grier, Phys. Rev. Lett. **77**, 1897 (1996).

[31] F. Diedrich *et al.*, Phys. Rev. Lett. **59**, 2931 (1987).

[32] D. J. Wineland *et al.*, Phys. Rev. Lett. **59**, 2935 (1987).

[33] G. Birkl, S. Kassner, and H. Walther, Nature **357**, 310 (1992).

[34] I. Waki, S. Kassner, G. Birkl, and H. Walther, Phys. Rev. Lett. **68**, 2007 (1992).

[35] J. N. Tan, J. J. Bollinger, A. S. Barton, and D. J. Wineland, in *Non–Neutral Plasma Physics II*, edited by J. Fajans and D. Dubin (AIP Press, New York, 1995), p. 215.

[36] J. Pieper, J. Goree, and R. Quinn, J. Vac. Sci. Technol. A **14**, 519 (1996).

[37] A. Melzer, A. Homann, and A. Piel, Phys. Rev. E **53**, 2757 (1996).

[38] A. Melzer, A. Homann, and A. Piel, in *The melting transition of the Plasma crystal*, pp. 135–138.

[39] H. Thomas and G. E. Morfill, Nature **379**, 806 (1996).

[40] N. N. Rao, Planet. Space Sci. **41**, 21 (1993).

[41] N. D'Angelo, Planet. Space Sci. **42**, 507 (1994).

[42] S. V. Vladimirov, Phys. Plasmas **1**, 2762 (1994).

[43] O. Havnes *et al.*, J. Vac. Sci. Technol. A **14**, 525 (1996).

[44] F. Melandsø, Phys. Plasmas **3**, 3890 (1996).

[45] A. Homann *et al.*, Phys. Rev. E **56**, 7138 (1997).

[46] R. L. Merlino, A. Barkan, C. Thompson, and N. D'Angelo, Plasma Phys. Control. Fusion **39**, A421 (1997).

[47] A. Homann *et al.*, Phys. Lett. A **242**, 173 (1998).

[48] A. Piel, A. Homann, and A. Melzer, Plasma Phys. Control. Fusion **41**, A453 (1999).

[49] D. Samsonov *et al.*, Phys. Rev. Lett. **83**, 3649 (1999).

[50] A. Melzer, S. Nunomura, D. Samsonov, and J. Goree, Phys. Rev. E **62**, 4162 (2000).

[51] O. Havnes *et al.*, Planet. Space Sci. **49**, 223 (2001).

[52] V. Nosenko, J. Goree, Z. W. Ma, and A. Piel, Phys. Rev. Lett. **88**, 135001 (2002).

[53] S. Peters, A. Homann, A. Melzer, and A. Piel, Phys. Lett. A **223**, 389 (1996).

[54] S. V. Vladimirov, Phys. Rev. E **49**, R997 (1994).

[55] A. V. Ivlev, U. Konopka, and G. E. Morfill, Phys. Rev. E **62**, 2739 (2000).

[56] A. V. Ivlev, R. Sütterlin, V. Steinberg, and G. E. Morfill, Phys. Rev. Lett. **85**, 4060 (2000).

[57] E. B. Tomme, B. M. Annaratone, and J. E. Allen, Plasma Sources Sci. Technol. **9**, 87 (2000).

[58] H. M. Thomas, in *VII Workshop on The Physics of Dusty Plasmas* (Boulder, Colorado, 1998).

[59] G. E. Morfill *et al.*, Phys. Rev. Lett. **83**, 1598 (1999).

[60] H. Thomas *et al.*, Physica Scripta **89**, 16 (2001).

[61] J. Goree, G. E. Morfill, V. N. Tsytovich, and S. V. Vladimirov, Phys. Rev. E **59**, 7055 (1999).

[62] V. N. Tsytovich, S. V. Vladimirov, G. E. Morfill, and J. Goree, Phys. Rev. E **63**, 056609 (2001).

[63] E. Thomas Jr., B. M. Annaratone, G. E. Morfill, and H. Rothermel, PRE **66**, 016405 (2002).

[64] H. Ikezi, Phys. Fluids **29**, 1764 (1986).

[65] J. H. Chu and L. I, Physica A **205**, 183 (1994).

[66] J. H. Chu, J. B. Du, and L. I, J. Phys. D: Appl. Phys. **27**, 296 (1994).

[67] M. S. Barnes *et al.*, Phys. Rev. Lett. **68**, 313 (1992).

[68] T. Nitter, Plasma Sources Sci. Technol. **5**, 93 (1996).

[69] H. Vestner and L. Waldmann, Physica **86A**, 303 (1977).

[70] H. Vestner and J. Halbritter, Z. Naturforschung **36a**, 559 (1981).

[71] S. M. Levitskij, Zh. Tekh. Fiz **27**, 1001 (1957).

[72] F. Schneider, Z. Angew. Phys. **6**, 456 (1954).

[73] P. Belenguer and J. P. Boeuf, Phys, Rev. A **41**, 4447 (1990).

[74] P. Belenguer, Ph.D. thesis, Université Nancy, 1990.

[75] M. Surendra, D. B. Graves, and I. J. Morey, Appl. Phys. Lett. **56**, 1022 (1990).

[76] M. Surendra, D. B. Graves, and G. M. Jellum, Phys. Rev. A **41**, 1112 (1990).

[77] V. A. Godyak and A. S. Kanneth, IEEE Trans. Plasma Sci. **14**, 112 (1986).

[78] V. A. Godyak, R. B. Piejak, and B. M. Alexandrovich, Rev. Sci. Instrum. **61**, 2401 (1990).

[79] V. A. Godyak, R. B. Piejak, and B. M. Alexandrovich, Phys. Rev. Lett. **68**, 40 (1992).

[80] V. A. Godyak, R. B. Piejak, and B. M. Alexandrovich, Plasma Sources Sci. Technol. **1**, 36 (1992).

[81] M. A. Liebermann, IEEE Trans. Plasma Sci. **16**, 638 (1988).

[82] M. A. Liebermann and A. J. Lichtenberg, *Principles of plasma discharges and material processing* (John Wiley and Sons Inc., New York, 1994).

[83] A. Homann, Dissertation, Christian–Albrechts–Universität Kiel, 1998.

[84] A. Melzer, *Der Plasmakristall: Phasenübergang und Stabilität*, Vol. 74 of *Reihe Physik* (Harri Deutsch Verlag GmbH, Frankfurt/ Main, 1997).

[85] T. Trottenberg, Diplomarbeit, Universitt Kiel, 1994.

[86] M. Klindworth, Master's thesis, Institute for Experimental and Applied Physics Christian-Albrechts-University Kiel, Kiel, 1999.

[87] R. Flohr, H. Schirmer, and A. Piel, Contrib. Plasma Phys. **33**, 153 (1993).

[88] R. Flohr, A. Melzer, and A. Piel, Plasma Sources Sci. Technol. **3**, 206 (1994).

[89] R. Flohr, Dissertation, Christian– Albrechts– Universität Kiel, 1993.

[90] H. M. Mott-Smith and I. Langmuir, Phys. Rev. **28**, 727 (1926).

[91] E. C. Whipple, Rep. Prog. Phys. **44**, 1197 (1981).

[92] J. E. Allen, R. L. F. Boyd, and P. Reynolds, Proc. Roy. Soc. (London) **70**, 297 (1957).

[93] F. F. Chen, Plasma Phys. **7**, 47 (1965).

[94] P. M. Chung, L. Talbot, and K. J. Touryan, *Electric Probes in Stationary and Flowing Plasmas: Theory and Appliations*, Vol. Bd. II of *Applied Physics and Engineering* (Springer Verlag, Berlin Hiedelberg New York, 1975).

[95] J. E. Allen, B. M. Annaratone, and U. deAngelis, J. Plasma Phys. **63**, 299 (2000).

[96] M. Lampe, J. Plasma Phys. **65**, 171 (2001).

[97] O. Hachenberg and W. Brauer, Adv. Electron. Phys **11**, 413 (1959).

[98] D. J. Gibbons, *Handbook of Vacuum Physics*, Vol. 2 of *3* (A. H. Beck, Oxford: Pergamon, 1966).

[99] H. d. Hagstrum, Phys. Rev **123**, 758 (1961).

[100] J. S. Colligon, Vacuum **11**, 272 (1961).

[101] W. C. Knudsen and K. K. Harris, Journal of Geophysical Research **78**, 1145 (1973).

[102] R. Kollath, *Sekundärelektronen-Emission fester Körper bei Bestrahlung mit Elektronen, Handbuch der Physik, XXI* (Springer Verlag, Berlin, Göttingen, Heidelberg, 1956).

[103] D. Winske and M. E. Jones, IEEE Trans. Plasma Sci. **23**, 188 (1995).

[104] S. Nunomura, T. Misawa, N. Ohno, and S. Takamura, Phys. Rev. Lett. **83**, 1970 (1999).

[105] C. Cui and J. Goree, IEEE Trans. Plasma Sci. **22**, 151 (1994).

[106] J. Goree, Plasma Sources Sci. Technol. **3**, 400 (1994).

[107] O. Havnes *et al.*, J. Geophys. Res. **92 A3**, 2281 (1987).

[108] O. Havnes, T. K. Aanesen, and F. Melandsø, J. Geophys. Res. **95**, 6581 (1990).

[109] P. S. Epstein, Phys. Rev. **23**, 710 (1924).

[110] M. J. Baines, I. P. Williams, and A. S. Asebiomo, Mon. Not. R. Astron. Soc. **130**, 63 (1965).

[111] S. Hamaguchi and R. T. Farouki, Phys. Rev. E **49**, 4430 (1994).

[112] J. E. Daugherty, R. K. Porteous, and D. B. Graves, J. Appl. Phys. **73**, 1617 (1993).

[113] S. Hamaguchi and R. T. Farouki, Phys. Plasmas **1**, 2110 (1994).

[114] M. D. Kilgore, J. E. Daugherty, R. K. Porteous, and D. B. Graves, J. Appl. Phys. **73**, 7195 (1993).

[115] J. Perrin, P. Molinás-Mata, and P. Belenguer, J. Phys. D: Appl. Phys. **27**, 2499 (1994).

[116] K. Chen, T. Kaplan, and M. Mostoller, Phys. Rev. Lett. **74**, 4019 (1995).

[117] D. Winske and M. E. Jones, IEEE **22**, 454 (1994).

[118] J. Goree, Phys. Rev. Lett. **69**, 277 (1992).

[119] U. Grigull and H. Sandner, *Wärmeleitung* (Springer Verlag, Berlin, Heidelberg, New York, 1979).

[120] K. Kremer, M. O. Robbins, and G. S. Grest, Phys. Rev. Lett. **57**, 2964 (1986).

[121] M. O. Robbins, K. Kremer, and G. S. Grest, J. Chem. Phys. **88**, 3286 (1988).

[122] R. T. Farouki, S. Hamaguchi, and M. Dalvie, Phys. Rev. A **45**, 5913 (1992).

[123] R. T. Farouki and S. Hamaguchi, J. Chem. Phys. **101**, 9885 (1994).

[124] S. Hamaguchi and R. T. Farouki, J. Chem. Phys. **101**, 9876 (1994).

[125] T. Nitter, T. K. Aslaksen, F. Melandsø, and O. Havnes, IEEE Trans. Plasma Sci. **22**, 159 (1994).

[126] M. Zuzic, H. Thomas, and G. E. Morfill, J. Vac. Sci. Technol. A **14**, 496 (1996).

[127] U. Konopka, L. Ratke, and H. M. Thomas, Phys. Rev. Lett. **79**, 1269 (1997).

[128] U. Konopka, G. E. Morfill, and L. Ratke, Phys. Rev. Lett. **84**, 891 (2000).

[129] G. Morfill, A. Ivlev, and J. Jokipii, Phys. Rev. Lett. **83**, 971 (1999).

[130] S. V. Vladimirov, K. Ostrikov, and M. Y. Yu, Phys. Rev. E **60**, 3257 (1999).

[131] O. S.Vaulina, S. A. Khrapak, A. P. Nefedov, and O. F. Petrov, Phys. Rev. E **60**, 5959 (1999).

[132] A. Homann, A. Melzer, and A. Piel, Phys. Rev. E **59**, 3835 (1999).

[133] H. Schollmeyer, A. Melzer, A. Homann, and A. Piel, Phys. Plasmas **6**, 2693 (1999).

[134] C. Hayashi, *Nonlinear Oscillations in Physical Systems* (Princeton University Press, Princeton, New Jersey, 1985).

[135] G. Sorasio, D. resendes, and P. K. Shukla, Phys. Lett. A **293**, 67 (2002).

[136] G. Praburam and J. Goree, Plasma Sources Sci. Technol. **5**, 84 (1996).

[137] M. R. Akdim and W. J. Goedheer, Phys. Rev. E **65**, 015401 (2002).

[138] S. A. Khrapak, A. I. Ivlev, G. E. Morfill, and H. M. Thomas, Proceedings, 3rd ICPDP, Durban, South Africa 2002 .

[139] C. Zafiu, A. Melzer, and A. Piel, *Measurement of Focussing Forces on Falling Dust Particles and its Relation to the Void Formation in Complex Plasmas* (2002), submitted.

[140] E. B. Tomme, D. A. Law, B. M. Annaratone, and J. E. Allen, Phys. Rev. Lett. **85**, 2518 (2000).

[141] M. Horányi, Phys. Plasmas **7**, 3847 (2000).

A Reprints of Journal Papers

A.1

NONLINEAR RESONANCES OF PARTICLES IN A DUSTY PLASMA SHEATH

C. Zafiu, A. Melzer and A. Piel

PHYSICAL REVIEW E
Vol. 63 (2001), Pages 066403-1–066403-8

PHYSICAL REVIEW E, VOLUME 63, 066403

Nonlinear resonances of particles in a dusty plasma sheath

C. Zafiu, A. Melzer, and A. Piel
Institut für Experimentelle und Angewandte Physik, Christian-Albrechts-Universität Kiel, 24098 Kiel, Germany
(Received 5 December 2000; published 23 May 2001)

Vertical oscillations of microparticles trapped in the sheath of a capacitive rf discharge have been excited showing a strongly nonlinear resonance. The nonlinear oscillations are analyzed in terms of an anharmonic fourth-order potential energy curve. It is demonstrated that the observed nonlinearities can be related to a position dependent charge of the microspheres, whereas the electric field is found to be as nearly linearly increasing. The experimental results on the position dependent charging and electric field structure are compared to a numerical model.

DOI: 10.1103/PhysRevE.63.066403 PACS number(s): 52.27.Lw, 52.35.Fp

I. INTRODUCTION

In the last few years, dusty plasmas have attained a great interest because of their importance for astrophysical phenomena and their application in plasma processing technologies. Plasmas containing small particles (nanometer to micrometer size) are found in planetary rings, comets, nebulae, noctilucent clouds, etc. Dusty plasmas play an important role in industrial devices for microchip processing, where particle formation poses a serious problem of contamination. Technological applications are found in discharges with reactive gases for particle growth and deposition, as well as manufacturing of nanopowders, solar cells, and new materials.

Even more fascinating in view of fundamental physics is the observation that microspheres trapped in the plasma sheath form nearly two-dimensional crystal-like structures (the so called plasma crystals [1–4]) providing an ideal model for condensed matter on a macroscopic scale.

The charge of the grains and the electric field structure in the sheath are considered to be crucial parameters for the particle trapping and crystallization of microparticle crystals in laboratory experiments on Earth.

Oscillatory motion of particles that are trapped in the sheath of an rf discharge was already used as a diagnostic means for determining the charge on microspheres [5]. This technique was later refined by using a laser force on the particle [6], confirming the Q/M values found earlier. The various oscillation modes of a particle trapped in the sheath, including parametric excitation of the vertical resonance, were studied in Ref. [7].

Damped linear oscillations of particles dropped into the sheath were exploited to obtain a detailed insight into the particle charge [8]. The key point in all these experiments is that the electric field is considered to be linearly increasing and the charge on the particle is constant, resulting in a linear resonance of the oscillating particle. A linear resonance is characteristic of a particle oscillating in a parabolic effective potential well, that results from the assumptions on the electric field and particle charge [5,6,9].

Recently, the nonlinear oscillations of single particles, that were trapped into the sheath region were used to explore the electric field structure of the sheath [10]. Self-excited oscillations driven by a delayed charging due to a finite charging time were observed by Nunomura *et al.* [11].

In the experiments here, micrometer sized spherical plastic particles of three different sizes are trapped in the ionic space charge sheath of a capacitive rf discharge (see Sec. IV) and their vertical nonlinear oscillations are studied here to derive the position dependent charging. The experimental results are compared with a numerical model.

II. OSCILLATION MODEL

The particles trapped in the positive ionic space charge of an rf discharge, usually attain a high negative charge (see also Sec. III) due to the higher electron mobility. The resulting electric force on the particle points upwards against the gravitational force and the static equilibrium of the particle in the sheath is described by the force balance [see Fig. 1(b)]

$$Mg = Q(x)E(x). \tag{1}$$

Here, we assume that the charge and electric field are position dependent but time averaged. x is coordinate in the ''local coordinate system'' relative to the particle equilibrium position. The ''absolute coordinate system'' is taken to be relative to the sheath edge. With x_0 being the equilibrium particle position in the 'absolute'' system, $x + x_0 = X$.

The general equation of motion then has the form

$$M\ddot{x} + M\beta\dot{x} = Q(x)E(x) - Mg + F_{exc}\sin(\omega t). \tag{2}$$

$M\beta\dot{x}$ is the force due to the friction of the particle with the neutrals [12]. The excitation force $F_{exc}\sin(\omega t)$ is due to the modulation of the rf power with a low frequency voltage, that results in a ''shaking'' of the plasma sheath with the applied low frequency. This periodical force drives the particle oscillation.

Other forces like the thermophoretic force [5], and the ion drag force [9] are neglected here. They are commonly assumed to be much smaller than the electric field force or gravity in the sheath, for large dust grains ($\geqslant 2$ μm).

In previous experiments [5,9], the electric field was assumed as linearly increasing from the sheath edge to the electrode [see Fig. 1(b)]; it was also assumed that the electric charge on the dust grains is constant over the regions covered by the oscillations. This results in a parabolic effective potential energy well for the particle. In this case, the general equation of motion simplifies to

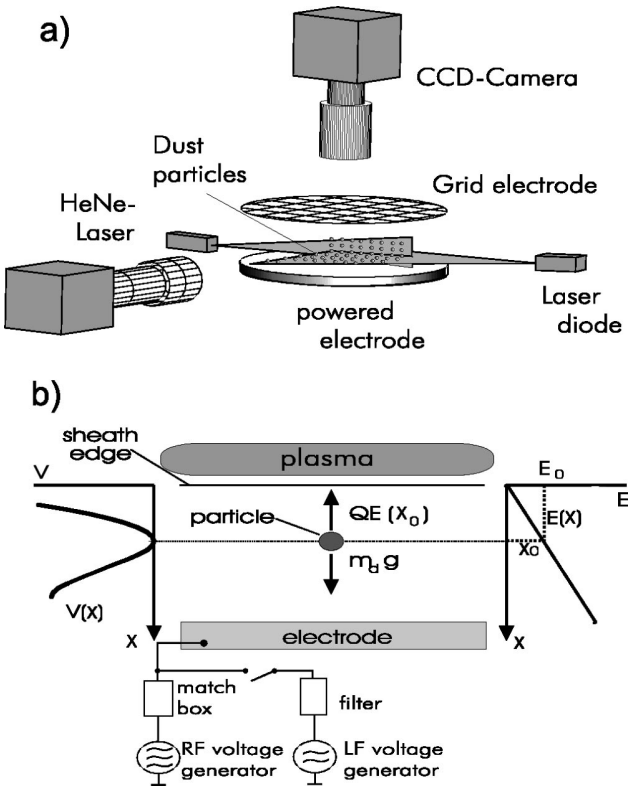

FIG. 1. Scheme of the experimental setup (a) and equilibrium in the sheath, modulation technique, electric field, and effective potential (b).

$$\ddot{x}+\beta\dot{x}+\omega_0^2 x=\frac{1}{M}F_{exc} \tag{3}$$

with $\omega_0^2=Q_0E_1$, where Q_0 is the constant charge and E_1 is the slope of the electric field. This equation describes a damped harmonic oscillation with a linear resonance. Such linear resonances of single particles were exploited to measure the electric charge of the dust grains [5].

Variation of the electron and ion densities and currents in the sheath lead to a deviation from the linearly increasing electric field profile and to a position-dependent dust charge. This results in a nonparabolic effective potential energy well that the particle experiences. In our analysis it is assumed that the electric field and the charge are described by polynomial functions

$$\begin{aligned} Q(x)&=Q_0+Q_1x+Q_2x^2+Q_3x^3\\ &=\tilde{Q}_0+\tilde{Q}_1X+\tilde{Q}_2X^2+\tilde{Q}_3X^3, \end{aligned} \tag{4}$$

$$\begin{aligned} E(x)&=E_0+E_1x+E_2x^2+E_3x^3\\ &=\tilde{E}_0+\tilde{E}_1X+\tilde{E}_2X^2+\tilde{E}_3X^3. \end{aligned} \tag{5}$$

[$\tilde{E}_0=0$ since $E(X)=0$ at the sheath edge $X=0$.] The equation of motion then becomes nonlinear, including higher order terms

$$\ddot{x}+\beta\dot{x}+C_1x+C_2x^2+C_3x^3+\cdots=\frac{F_{exc}}{M}\cos(\omega t). \tag{6}$$

The coefficients C_1, C_2, and C_3 are combinations of electric field and charge coefficients.

$$C_1=\frac{1}{M}(Q_0E_1+Q_1E_0), \tag{7}$$

$$C_2=\frac{1}{M}(Q_0E_2+Q_1E_1+Q_2E_0), \tag{8}$$

$$C_3=\frac{1}{M}(Q_0E_3+Q_1E_2+Q_2E_1+Q_3E_0). \tag{9}$$

C_2 and C_3 describe the nonlinear terms giving the deviation of the effective potential energy well from the simple parabolic shape. If C_2 and C_3 are zero, then the simple damped harmonic oscillation is obtained, with the frequency determined by C_1. C_2 determines the up/down asymmetry of the potential in the sheath and C_3 determines the weakening or strengthening of the potential energy well for higher oscillation amplitudes.

Higher orders that could be taken into account in the equation of motion would add new unknown coefficients. Here we restrict ourselves to the three coefficients holding the main information, i.e., resonance frequency (C_1), oscillation/potential asymmetry (C_2), and weakening/strengthening of the potential (C_3).

III. CHARGING AND SHEATH MODEL

The experiments are compared with a model of particle charging in the sheath of an rf discharge to give a more detailed insight into the problem.

Here, the particle charging is described by the commonly used OML model. Because of their large size compared to the plasma components (ions and electrons) the dust particles act like small probes collecting ionic and electronic currents on their surface. In the special situation of the sheath, a modified expression for the ion current, that accounts for the supersonic ion flow in the sheath is adopted [13]

$$I_i(\Phi_p,x_p)=n_se\pi R^2\left(\frac{k_BT_e}{m_i}\right)^{1/2}\left[1-2\frac{e\Phi_p}{k_BT_e}\left(\frac{v_B}{v_i(x_p)}\right)^2\right], \tag{10}$$

$$I_e(\Phi_p,x_p)=-n_e(x_p)e\pi R^2\left(\frac{8k_BT_e}{\pi m_e}\right)^{1/2}\exp\left(\frac{e\Phi_p}{k_BT_e}\right). \tag{11}$$

Here R is the particle radius, k_B is the Boltzmann constant, m_i and m_e are the ion and electron mass respectively, T_e is the electron temperature, and Φ_p the surface potential of the particle relative to the local plasma potential at the particle position. In the sheath, the reduced electron density is taken into account for the electron current. Therefore n_e is the electron density at the particle position x_p. The ions are assumed to be accelerated to the velocity v_i by the sheath

electric field without collisions. The ion density at the particle position can then be determined, according to the equation of continuity

$$n_i(x_p)v_i(x_p)=n_s v_B, \tag{12}$$

where n_s is the ion/electron density at the sheath edge and v_B is the Bohm velocity. The electron and ion currents are therefore position dependent due to the reduction of the electron density and increase of ion velocity in the sheath, respectively. n_e and v_i are taken as position dependent but time averaged values over the rf period because the rf period is much smaller than the charging time or the oscillation period of the dust particle.

The equilibrium floating potential and thus the equilibrium charge are derived from the balance of the electron and ion currents. The charge on the particulate is related to the floating potential, assuming the particle as a spherical capacitor [5]

$$C=4\pi\varepsilon_0 R, \tag{13}$$

$$Q=C\Phi_p. \tag{14}$$

The sheath model of Lieberman [14] is applied here to calculate the electron and ion densities, velocities, and electric field in the sheath.

The sheath model of Lieberman [14] presents a self-consistent solution for the ion and electron densities and the electric potential in the sheath, obtained under the assumptions of time independent, collisionless ion motion, and inertialess electrons. Using the model of Lieberman, the electric field, ion and electron densities, and floating potential on the grain surface have been calculated and plotted in the absolute coordinate system in Fig. 2.

Multiplying the calculated charge $Q(x)$ with the electric field $E(x)$, the potential energy curve is obtained after integration. This calculated potential curve was compared with the potential determined from the experimental values using C_1, C_2, and C_3 [see Sec. V and Fig. 3(b)].

Figure 2(c) represents the calculated electric field in the sheath, together with a linear fit. As it can be observed, the electric field is almost linear over the whole plasma sheath, in agreement with recent results [15]. Only in the vicinity of the plasma edge, the electric field starts with a smaller slope. To simplify the analysis of the experiment, we assumed the following approximation for the electric field: at the sheath edge ($X=0$), it starts as zero until the ''turning point'' (at $X=x_s$) from which on the field continues as a linearly increasing function [see Fig. 2(b), dotted curve].

Considering this, Eq. (5) becomes

$$E(X)=\begin{cases}0, & X\leqslant x_s\\ \tilde{E}_1(X-x_s)=E_0+E_1x, & X>x_s.\end{cases} \tag{15}$$

If this expression is replaced in the equations for C_1, C_2, and C_3, Eqs. (7), (8), and (9) become

$$C_1=\frac{1}{M}(Q_0E_1+Q_1E_0), \tag{16}$$

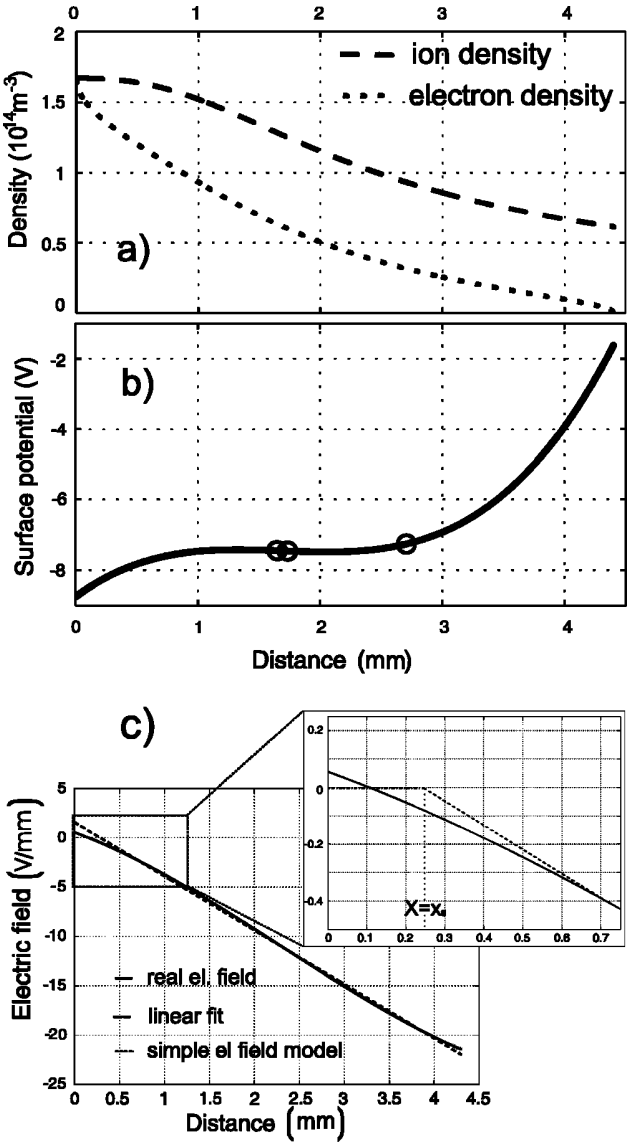

FIG. 2. Lieberman and Lichtenberg model; electron and ion densities (a), floating potential (b), and electric field (c). The symbols mark the positions where the the force balance is fulfilled for each particle.

$$C_2=\frac{1}{M}(Q_1E_1+Q_2E_0), \tag{17}$$

$$C_3=\frac{1}{M}(Q_2E_1+Q_3E_0), \tag{18}$$

where $E_0=E_1(x_0-x_s)$ with x_0 the equilibrium position of the particle. C_1, C_2, and C_3 are zero for $X\leqslant x_s$.

Assuming that the charging process is the same for all three particles, it is reasonable to introduce a ''charging function'' $\Phi_p(X)$. Under the assumption of the spherical capacitor charging model for the dust grains, this charging function is the floating potential. Therefore we split the

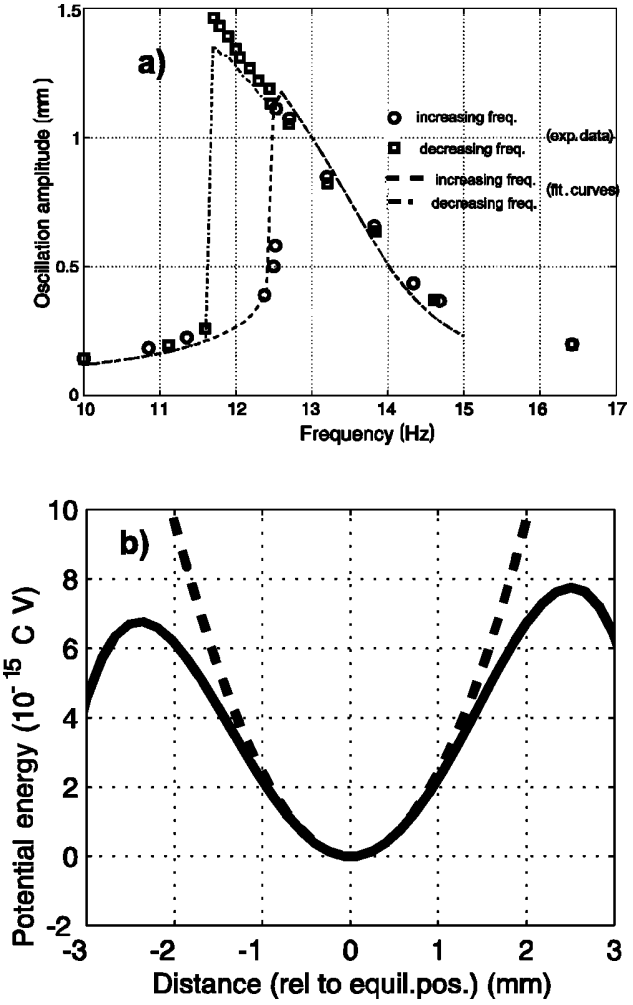

FIG. 3. Best-fit results of the nonlinear resonance curve (a) and effective potential well (b) for 9.47 μm particle. The dashed line in plot (b) represents the ideal parabolic potential well.

charge of the grain into the geometrical factor $4\pi\epsilon_0 R$ and assume the charging function as the ''universal'' floating potential $\Phi_p(X)$

$$Q(X) = \Phi_p(X) 4\pi\epsilon_0 R. \tag{19}$$

The charging function is also assumed to be a third-order polynomial function of position, like the particle charge (see Eq. 4).

$$\Phi_p(X) = \tilde{\Phi}_0 + \tilde{\Phi}_1 X + \tilde{\Phi}_2 X^2 + \tilde{\Phi}_3 X^3 \tag{20}$$

Figure 2(b) shows the floating potential computed from balancing the electron and ion currents on the particle surface, according to Eqs. (10) and (11) and introducing the ion and electron average densities [plotted in Fig. 2(a)]. The open circles indicate the equilibrium positions for the three different particles with diameters of 9.47 μm, 12.07 μm, and 20.02 μm used in the experiments.

IV. EXPERIMENT

The experiments have been performed in a parallel plate rf discharge in helium at low pressure (5.8 Pa) and rf power of 13 W [see Fig. 1(a)]. Monodisperse, spherical plastic particles of 9.47 μm and 12.07 μm diameter, made of melamine formaldehyde, and of 20.02 μm diameter, made of polymethylmethacrylate are immersed into the plasma. The lower electrode is powered while the rest of the discharge chamber is grounded. The particles are trapped in the sheath above the lower electrode. Here, an electrode with a shallow parabolic trough is used to impose a very weak horizontal confinement on the particle. Two 690-nm laser diodes were used to illuminate the particles trapped in the sheath. One beam is expanded horizontally and the other vertically.

Two video cameras were used for observation from top and from side. The vertical laser sheet together with the side view camera are used to record images of the oscillating particle. The side view high speed camera allows recording at up to 200 frames/s.

Low frequency modulation of the rf voltage was used for excitation of large amplitude particle oscillation. By comparison with laser excitation, this voltage modulation technique has been shown not to affect the plasma environment [6]. The excitation signal is applied to the electrode through a low pass filter [see Fig. 1(b)]. The excitation amplitudes were: 5 V_{pp} (d=9.47 μm), 10V $_{pp}$ (d=12.07 μm), and 23 V_{pp} (d=20.02 μm). The oscillations are recorded over several oscillation periods, with up to 100 frames/s.

The three different particle sizes were used to inspect a large region of the sheath.

Very small particles of 0.93 μm were introduced to mark the position of the sheath edge ($X=0$). Because of their small mass, we assumed that they need a very small electric field to levitate them and, thus, we consider them lying at the sheath edge.

V. DATA PROCESSING TECHNIQUE AND RESULTS

The nonlinear resonance curves are measured in the following way. A single particle of one of the three different sizes is introduced into the chamber. The particle is trapped in the sheath of the lower electrode and then the low-frequency modulation is applied with various frequencies. The resulting oscillation amplitudes are measured upwards and downwards relative to the equilibrium position. The resulting resonance curves are shown in Fig. 4 for the smallest (9.47 μm) and the largest (20.02 μm) particle [12]. In our experiments, hysteretic resonance curves were obtained, that bend towards lower frequencies and yield jumps or drops in amplitude for increasing or decreasing frequency, respectively (see Fig. 4). The observed hysteresis is a general feature of nonlinear resonances [16]. From this overall behavior, it can already be deduced that the effective potential becomes softer with increasing the amplitude, that means that C_3 must be negative.

It is also easily observed that the oscillation is asymmetric and that the asymmetry depends on the position in the sheath. For the lighter particle (that oscillates close to the

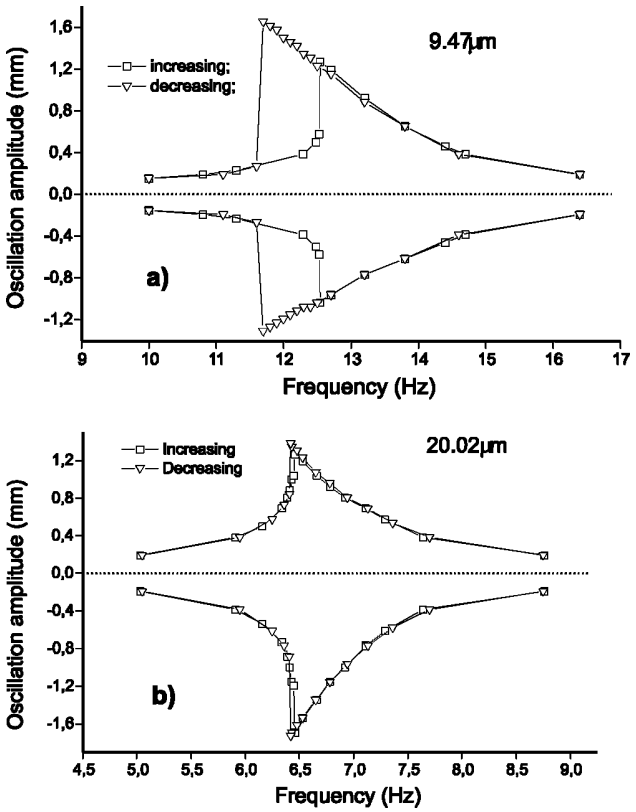

FIG. 4. Measured upwards and downwards amplitude curves for a 9.47 μm (a) and a 20.02 μm (b) particle, for increasing and decreasing frequency, relative to the equilibrium position.

sheath edge), the oscillation asymmetry is towards the plasma edge, which means a positive C_2. In the case of heavier particles (that oscillate deeper in the sheath), the oscillation asymmetry changes, showing a potential asymmetry towards the electrode, which means that C_2 is now negative.

The coefficients of nonlinearity C_1, C_2, and C_3 have been determined in two ways from the resonance curves. First, the equation of motion (6) is solved approximately, using the following trial solution [16]

$$x(t) = B_0 + A_1 \sin(\omega t) + B_1 \cos(\omega t). \tag{21}$$

where B_0 is the term that defines the asymmetry (offset) of the oscillation. Considering that $A_1^2 + B_1^2 = D^2$, where D is the amplitude of oscillation, the general equation of motion can be solved, neglecting terms of higher harmonics ($\geqslant \omega$). The amplitude and the asymmetry of the oscillation are then obtained from the system

$$\left(\frac{F_{exc}}{M}\right)^2 = \left[\omega^2 - C_1 - 2C_2B_0 - \frac{3}{2}C_3(2B_0^2 + D^2)\right]^2 D^2 + \beta^2\omega^2 D^2,$$

$$0 = C_1B_0 + \frac{1}{2}C_2(2B_0^2 + D^2) + \frac{1}{4}C_3B_0(4B_0^2 + 3D^2) + g. \tag{22}$$

TABLE I. Best-fit values for coefficients C_1, C_2, and C_3.

d (μm)	C_1 (s^{-2})	C_2 ($m^{-1}s^{-2}$)	C_3 ($m^{-2}s^{-2}$)
9.47	7200	1.5×10^5	-1.2×10^9
12.07	6200	1×10^5	-1.1×10^9
20.02	1900	-5.1×10^5	-6×10^7

Solving this system for given C_1, C_2, and C_3, the nonlinear resonance curve can be calculated (D as a function of frequency). The damping constants, β were computed for each particle size used in the experiment [12]. They were found to be $\beta = 1.64\,s^{-1}$ (9.47 μm), $1.28\,s^{-1}$ (12.07 μm), and $0.78\,s^{-1}$ (20.02 μm).

The second way of finding the values for C_1, C_2, and C_3 is by numerically solving the general equation of motion. This method is more general since we can take into account that the particle might be pushed into the plasma region where only the gravitation and friction forces act on it. Again, the values for the coefficients governing the equation of motion are obtained by fitting the computed resonance curve to the experimental one. The values found in this way are very close to those computed using the previous method. The differences are within 5% of each value.

Here, the numerical solution of the general equation of motion is used to find the best-fit values for C_1, C_2, and C_3. Figure 3(a) presents the best-fit result for the 9.47 μm particle (the averaged amplitude between the upwards and downwards excursions). Table I shows the best-fit values for the three coefficients for all three particle sizes.

As expected, the change of sign for C_2 (that defines the asymmetry of the effective potential well, see Fig. 3(b) in the case of 20.02 μm particle reflects the change of oscillation asymmetry experimentally observed. Also negative values of C_3 (related to the softening of the effective potential well) for all particle sizes were obtained, in agreement with the model.

At this point the coefficients in the equation governing the nonlinear oscillations of the particles have been derived. The aim is furthermore to see how the charging process and the electric field structure influence the effective potential, leading to the nonlinear features of the resonance curves that were discussed above (bending and asymmetry) and which are the nonlinear individual contributions either of the electric field and charge to the nonparabolic potential well.

Considering that the small particles of 0.93 μm lie just at the sheath edge, the electric field is chosen to be of the form described by Eq. (15) and the particle charge is defined by

$$\begin{aligned} Q(X) &= \tilde{Q}_0 + \tilde{Q}_1 X + \tilde{Q}_2 X^2 + \tilde{Q}_3 X^3 \\ &= \tilde{Q}_0 + \tilde{Q}_1(x + x_0) + \tilde{Q}_2(x + x_0)^2 + \tilde{Q}_3(x + x_0)^3. \end{aligned} \tag{23}$$

x_0 is the position of the particle for which the resonance curve is recorded relative to the sheath edge, x_s is the distance from the sheath edge to the ''turning point'' where the electric field becomes linear and x is the ''local coordinate.''

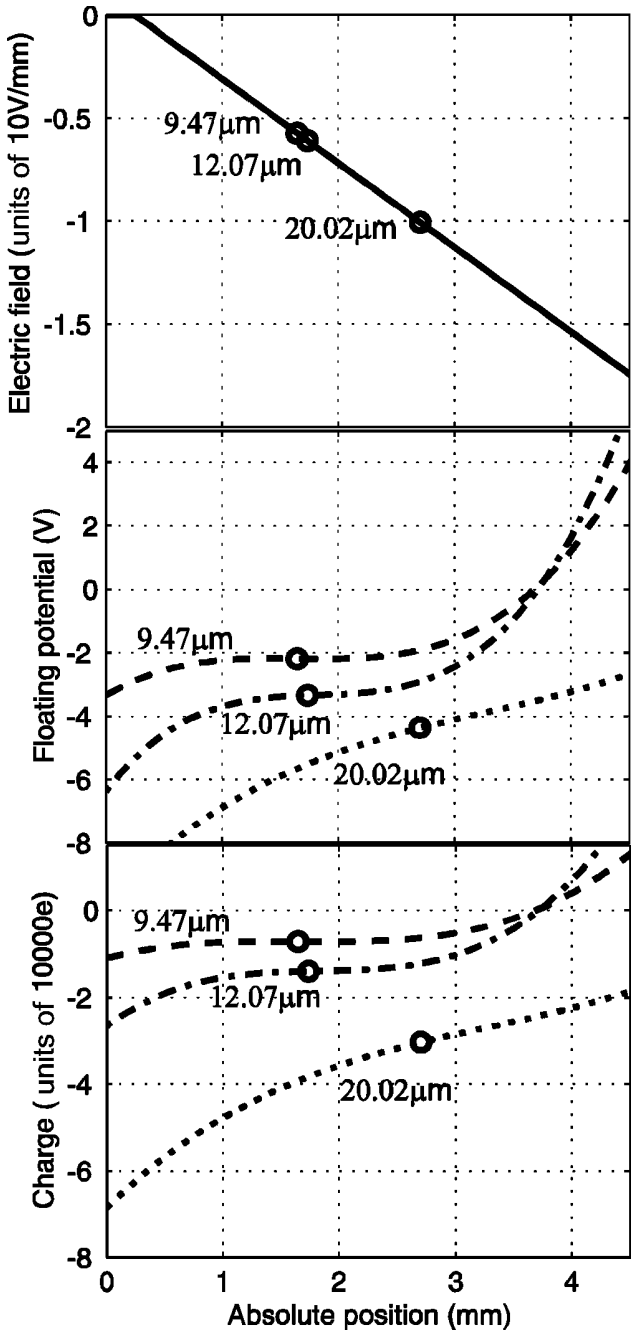

FIG. 5. Electric field, floating potential and charge components in the ''absolute coordinate system'' and particle equilibrium positions. The symbols mark the positions where the force balance is fulfilled for each particle.

The depth x_s was chosen in order to obtain the best agreement of the floating potential curves for all three particles. It was found to be $x_s = 0.25$ mm, in good agreement with Lieberman model, as can be observed in Fig. 2.

Assuming a linearly increasing electric field with a small plateau at the plasma edge and a polynomial-like variation of the charge on the particulate, the charge, and the floating potential are computed, using the values for C_1, C_2, and C_3 obtained above. They are plotted in Fig. 5.

TABLE II. Charge components in the ''absolute coordinate system.''

d (μm)	$\tilde{Q}_0$ (e)	$\tilde{Q}_1$ (e/m)	$\tilde{Q}_2$ (e/m^2)	$\tilde{Q}_3$ (e/m^3)
9.47	1.10×10^4	-7.18×10^6	4.42×10^9	-8.92×10^{11}
12.07	2.67×10^4	-1.98×10^7	1.06×10^{10}	-1.93×10^{12}
20.02	6.86×10^4	-2.64×10^7	6.24×10^9	-6.34×10^{11}

The values for the charge components are given in Table II. The electric field slope is defined by $\tilde{E}_1 = 4.10 \times 10^6$ V/m^2. It was obtained from the potential drop between the quasineutral plasma ($V_{plasma} = 32.5$ V) and the electrode self-bias ($V_{bias} = -45.7$ V)

$$\int_{x_s}^{x_{max}} E(X)\,dX = V_{plasma} - V_{bias}. \tag{24}$$

Figure 6 shows the particle charge at the equilibrium position as a function of particle radius. It can be easily observed that the charge is not a linear function of the radius.

Recently, in similar experiments, Ivlev *et al.* [10] have studied experimentally nonlinear oscillations of microspheres. They determined the coefficients of nonlinearity from super-harmonic and subharmonic resonances that do not occur under our experimental conditions. They attributed the nonlinearity completely to the electric field, treating the dust charge as constant. Applying this model to our data, the electric field components E_1, E_2, E_3 were computed. The so determined electric field is shown in Fig. 7. The curves show that the electric field is extremely nonlinear. Furthermore, the electric field computed for the 9.47 μm and 12.07 μm becomes positive deeper in the sheath. This is in contradiction with the statements of Lieberman model. Thus, a model of spatially constant dust charge is not in agreement with our experimental data.

Therefore in following step, a spatially variable charge of the particle and a nonlinear electric field were taken into account. The electric charge on the grain surface is still considered to be described by a third order polynomial whereas the electric field is considered to be parabolic.

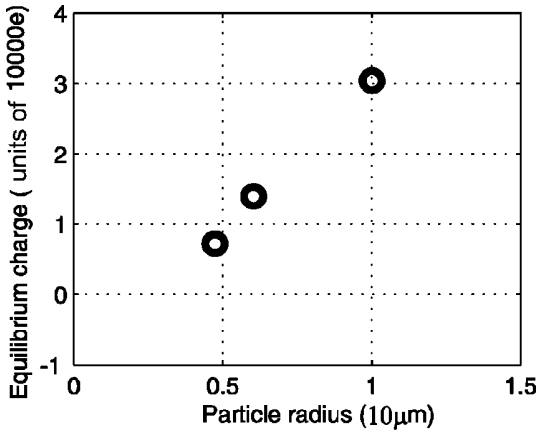

FIG. 6. Particle charge at the equilibrium position.

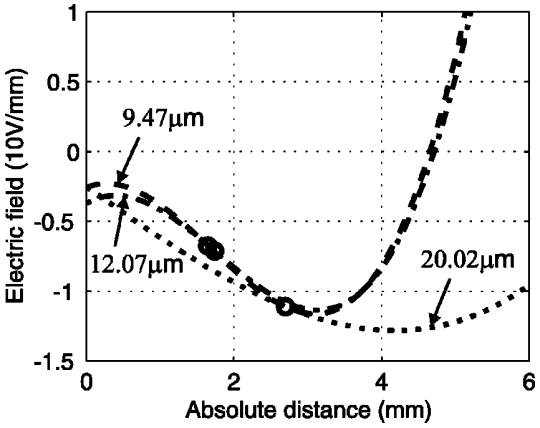

FIG. 7. Electric field components assuming a constant charge of the particle over the whole sheath. The symbols mark the positions where the force balance is fulfilled for each particle.

$$E(X)=\begin{cases}0, & X\leqslant x_s\\ \tilde{E}_1(X-x_s)+\tilde{E}_2(X-x_s)^2, & X>x_s\,.\end{cases} \tag{25}$$

Again the values for $\tilde{E}_1$ and $\tilde{E}_2$ have to satisfy the potential drop condition according to Eq. (24). The electric field and floating potential for all three particle sizes are plotted in Fig. 8 for three representative sets of values for the electric field components $\tilde{E}_1$ and $\tilde{E}_2$. $\tilde{E}_1$ is chosen as arbitrarily between 0 and 4×10^6 V/m^2 and $\tilde{E}_2$ is computed using Eq. (24). For larger values of E_1, E_2 would become negative, resulting in an unphysical concave curvature of the electric field. As it can be observed, the floating potential curves corresponding to the largest particle are still shifted from the curves corresponding to the smaller particles, for each set of electric field components. Figure 8(c) with $\tilde{E}_1=4\times10^6$ V/m^2 nearly corresponds to the case of linear electric field discussed above.

VI. DISCUSSION

All three curves representing the electric charge of the particles show the same general trend of the negative charge to decrease with increasing depth in the plasma sheath. This is mainly due to the reduction of electron density in the sheath that leads to a less effective charging of the particle [see Fig. 2(a) and Eq. (11)]. The experiments support this finding. The change of the asymmetry coefficient C_2 can be related to the change of slope of the floating potential curve. The weakening of the potential curves, as seen in the experimental resonance curves, can be traced back to a negative C_3 and thus to the curvature of the floating potential curve, as found in the model.

A quite good mutual overlapping of floating potential curves was obtained for 9.47 μm and 12.07 μm, either assuming a linearly increasing or for a nonlinear electric field, but, in both cases, the curve corresponding to the 20.02 μm particle is somewhat shifted.

This leaves some question marks on the capacitive charging model assumed for the particle. According to Tomme *et al.* [8], the charge is not a simple linear function of the particle radius, but has a more complicated, nonlinear dependence. This is the reason why we consider that the simple capacitive model is not able to totally explain the charging process for all particle sizes and/or for all regions of the plasma sheath.

The comparison with results of Ref. [8] shows a good agreement for the light particles (9.47 and 12.07 μm), while for the heavier particle (20.02 μm), the agreement is worse.

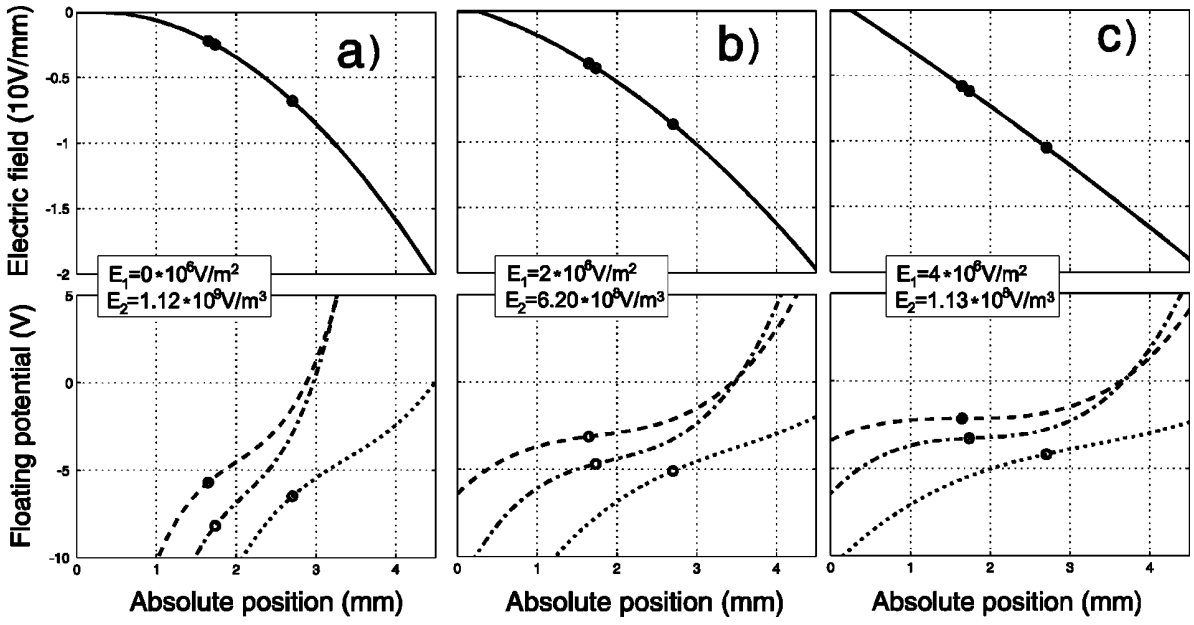

FIG. 8. Electric field and floating potential, assuming a nonlinear charge of the particle and a parabolic electric field in the sheath. The symbols mark the positions where the force balance is fulfilled for each particle.

The main reason is that this model starts with different assumptions (a constant charge of the particle over the whole oscillation amplitude and another kind of oscillation studied there, i.e. damped oscillations of dropped particles).

On the other hand, another effect can influence the charging of the particle. As it was shown in Sec. V, the heaviest particles float about 3 mm deep in the sheath. If we compare this depth with the mean free path of ion-neutral collisions computed at the experimental pressure and ion drift velocity, the values are quite close (the mean free path is about 3.8 mm). Considering this, an altered ion current at the particle position, due to the charge transfer and elastic collisions in the sheath, is to be taken into account. This alters the ionic current given in the OML model, leading to a less efficient ion decharging of the particle and to a higher negative charge on the dust grain than predicted by the OML model.

Another source of uncertainty is that the largest particles are made of a different material than the smaller ones. Since at the microscopic scale, the way that charges stick to the polymer chains of the material is not known in detail, a different charging might occur for different materials.

VII. CONCLUSIONS

Here, experimental results on particle oscillations in a capacitive rf plasma have been presented. Previous experiments relied on a constant charge of the particle and a linearly increasing electric field in the plasma sheath. Here we extended the model to a position dependent charge and a nonlinearly increasing electric field to explain the nonlinear resonances by introducing higher order terms into the general equation of motion. The nonlinear resonances have been attributed to an anharmonic potential energy well with up-down asymmetry and weakening at higher oscillation amplitudes.

The charging function components corresponding to one set of experimental conditions were computed, for three different particle sizes, putting the charging model in agreement with the experimental data.

Both linearly increasing and nonlinear electric fields were taken into account for computing the charge components and the floating potential. Thus it was demonstrated that the simple capacitance model cannot explain the charging behavior of all three particles. Overall good agreement with the experimental data and with the theoretical model of the plasma sheath is found for the linearly increasing electric field.

ACKNOWLEDGMENT

This work was supported by DFG Grant Nos. Pi185-17/1 and INTAS 97-0775.

[1] H. Ikezi, Phys. Fluids **29**, 1764 (1986).
[2] H. Thomas, G. E. Morfill, V. Demmel, J. Goree, B. Feuerbacher, and D. Möhlmann, Phys. Rev. Lett. **73**, 652 (1994).
[3] J. H. Chu and I. Lin, Phys. Rev. Lett. **72**, 4009 (1994).
[4] Y. Hayashi and K. Tachibana, Jpn. J. Appl. Phys., Part 2 **33**, L804 (1994).
[5] A. Melzer, T. Trottenberg, and A. Piel, Phys. Lett. A **191**, 301 (1994).
[6] A. Homann, A. Melzer, and A. Piel, Phys. Rev. E **59**, 3835 (1999).
[7] H. Schollmeyer, A. Melzer, A. Homann, and A. Piel, Phys. Plasmas **6**, 2693 (1999).
[8] E. B. Tomme, B. M. Annaratone, and J. E. Allen, Plasma Sources Sci. Technol. **9**, 87 (2000).
[9] T. Trottenberg, A. Melzer, and A. Piel, Plasma Sources Sci. Technol. **4**, 450 (1995).
[10] A. V. Ivlev, R. Stterlin, V. Steinberg, M. Zuzic, and G. Morfill, Phys. Rev. Lett. **85**, 4060 (2000).
[11] S. Nunomura, T. Misawa, N. Ohno, and S. Takamura, Phys. Rev. Lett. **83**, 1970 (1999).
[12] P. S. Epstein, Phys. Rev. **23**, 710 (1924).
[13] T. Nitter, Plasma Sources Sci. Technol. **5**, 93 (1996). In this reference the ion current equation (27) has a misprint. Here the correct equation is used.
[14] M. A. Lieberman, IEEE Trans. Plasma Sci. **PS-16**, 638 (1988).
[15] E. B. Tomme, D. A. Law, B. M. Annaratone, and J. E. Allen, Phys. Rev. Lett. **85**, 2518 (2000).
[16] C. Hayashi, *Nonlinear Oscillations in Physical Systems* (Princeton University Press, Princeton, NJ, 1985).

A.2

ION DRAG AND THERMOPHORESIS FORCES ACTING ON FREE FALLING PARTICLES IN AN RF-DRIVEN PLASMA SHEATH

C. Zafiu, A. Melzer and A. Piel

PHYSICS OF PLASMAS
Vol. 9, Number 11 (November 2002), Pages 4794–4803

Ion drag and thermophoretic forces acting on free falling charged particles in an rf-driven complex plasma

C. Zafiu,[a] A. Melzer, and A. Piel
Institut für Experimentelle und Angewandte Physik, Christian-Albrechts-Universität Kiel, 24098 Kiel, Germany

(Received 19 July 2002; accepted 29 August 2002)

Monodisperse plastic microspheres have been dropped through a long radio-frequency discharge column. The trajectories of the falling particles have been measured. It was observed that the particles are driven out of the plasma. From the trajectory analysis and plasma measurements the forces on the particles have been derived. Special attention has been paid to the thermophoresis and ion drag forces which are also considered to be responsible for the void formation in microgravity experiments. Two experimental situations have been considered here: first a plasma characterized by its natural symmetric electric potential and temperature distribution and second, a plasma with an asymmetric temperature and electric potential profile. For both cases a good agreement has been found between the measured ''trajectory force'' obtained from the particle trajectory analysis and the sum of the ion drag, thermophoretic and electric field force. © *2002 American Institute of Physics.* [DOI: 10.1063/1.1516598]

I. INTRODUCTION

In the last few years dusty plasmas have attained a large interest because of their importance in astrophysical and upper atmosphere phenomena (planetary rings, comets, nebulae, and noctilucent clouds, respectively) and for their application in plasma processing technologies. For example, they play a very important role in industrial devices for microchip processing, where particle formation poses a serious problem of contamination. Among other technological applications, manufacturing of nanopowders, solar cells, and new materials are to be mentioned, as well as discharges in reactive gases for particle growth and deposition.[1]

It is well known that under the influence of gravity large particles ($a>1\ \mu$m) in complex plasmas tend to sediment to the bottom of the discharge, into the plasma sheath of an electrode or of the vessel wall, where sufficiently strong electric fields prevail to levitate the particles.[2] In contrast, fine grains ($a<1\ \mu$m) can be trapped in local plasma potential maxima within the discharge volume.[3]

The conditions in the plasma sheath are suitable for the formation of flat, almost 2D plasma crystals.[4–7] These systems have been extensively studied, e.g., with respect to the melting phase transition,[8,9] the excitation of lattice waves,[10–12] and Mach cones.[13–17]

The nonequilibrium conditions of the plasma sheath are responsible for a number of unexpected features of the 2D plasma crystals. The supersonic ion flow in the sheath leads to positive charge accumulation in the particle wakes,[18–20] which causes attractive forces[21–23] and leads to vertical alignment and a novel type of instability.[18,24,25] For this reason, in complex plasmas under gravity conditions the formation of proper 3D plasma crystals is limited.

The generation of 3D extended plasma crystals is still an important goal for the complex plasma research. In laboratory devices, the nonequilibrium effects can be reduced by using high gas pressures, which leads to the destruction of the directed ion flow and quenches the Schweigert instability. In this way crystals with typically 5–10 layers can be generated.[26,27] Under special conditions, up to 19 layers have been obtained.[28] An alternative approach is the search for plasma crystallization under microgravity conditions.

In microgravity experiments, particle confinement is determined by the weaker forces like ion drag, neutral drag, thermophoresis, and electric field force in the bulk plasma, which are generally negligible in the laboratory plasmas when compared to the gravitation force. First investigations under microgravity[29,30] have shown an unexpected feature. Rather than accumulating the microparticles in the positive potential well of the discharge, the plasma center was found particle-free and a large ''void,'' with a sharp boundary formed. In a similar manner, submicron particles fill the plasma volume and also show void formation.[31,32] Although this effect gives a hint that the confining electric force on the particles may be smaller than the outward oriented ion drag and/or thermophoretic forces, the behavior of this system is still little understood. Recent models of the void phenomena[33,34] and simulations[35] raised some doubt on the validity of expressions describing ion drag force.[36] The simulation results,[35] for example, have shown that an enhancement of the theoretically predicted magnitude of the ion drag by a factor of 10 is necessary for a void formation.

This situation motivated us to conceive a laboratory experiment for the study of the ion drag and thermophoretic forces. The principle of these investigations is to study free falling particles for which gravity is balanced by gas friction. The vertical dynamic equilibrium is fulfilled as long as the particles are falling, and thus, the influence of the gravitation does not play a dominant role here in addition. Ion drag and

[a]Electronic mail: zafiu@physik.uni-kiel.de

thermophoresis act perpendicular to the direction of gravity which allows us to decouple the gravitational vertical motion from the interesting horizontal one.

The ion drag and the thermophoretic force acting on the particles are measured here under two experimental conditions: in a symmetric plasma where the neutral gas temperature and potential profiles are almost parabolic, and in a plasma where the temperature profile has been modified by a heat source.

The outline of the paper is as follows: In Sec. II we summarize the theoretical background, the experimental setup is described in Sec. III, the data processing and experimental results are presented in Sec. IV, and then discussed in Sec. V.

II. FORCES ACTING ON FREE-FALLING PARTICLES

When dust particles are dropped through a long gas column, depending on the pressure and friction constant, a steady-state falling regime is reached, when the gravitation force is balanced by the neutral gas friction force, which acts in the opposite direction,

$$\mathbf{G}+\mathbf{F}_{\text{frict\_}y}=0, \tag{1}$$

$$mg-m\beta\dot{y}=0, \tag{2}$$

where y denotes the vertical direction, and β is the friction constant derived from the Epstein friction law[37] normalized to the particle mass

$$\beta=\delta n_n \frac{m_n v_{\text{th},n}}{a\rho}. \tag{3}$$

Here, m_n, $v_{\text{th},n}$, and n_n are the mass, thermal velocity, and number density of the neutral gas, a and ρ are the radius and mass density of the particle material and δ is the Millikan reflection coefficient which can take values between 1 and 1.444.

The balance of gravity by the friction force is valid throughout the gas volume, whereas levitation of particles by the inhomogeneous electric field in the sheath regions is generally localized to a plane. This allows the study of acting forces by evaluating particle trajectories. The argument also holds for the horizontal force balance.

When the particles are falling through the plasma, in the horizontal direction important forces like friction, electric force, ion drag, and thermophoresis are dominant and their influence will be described here.

In a cylindrical plasma, the positive ions are generally accelerated from the center of the discharge toward the walls due to the higher plasma potential on the discharge axis. This results in an outwards oriented ''ion wind'' dragging the negatively charged particle towards the wall. The ion drag force F_{ion} consists of two components[35,36,38] describing how momentum is transferred from the drifting ions to the particle: the collection force, resulting from direct momentum transfer of the drifting ions which are collected on the particle surface, and the Coulomb force resulting from the momentum transfer of the ions deflected in the electrostatic field of the negatively charged dust grain, thus

$$F_{\text{ion}}=F_{\text{collect}}+F_{\text{Coulomb}}. \tag{4}$$

Since the dust particle velocity is negligible compared to the ion drift velocity, the relative dust-ion velocity is in fact the ion velocity. In the usually adopted derivation of the ion drag force by Barnes *et al.*[36] it is supposed that no interaction of the ions with the particle occurs outside the Debye sphere, and the ion mean free path is larger than the Debye radius.[36] The last assumption is justified only for relatively low gas pressures.

The collection force is given by[36]

$$F_{\text{collect}}=n_i m_i v_i v_s \pi b_c^2, \tag{5}$$

with

$$v_s=\left(\frac{8k_B T_i}{\pi m_i}+u_i^2\right)^{1/2} \tag{6}$$

being the mean speed of ions approaching the particle. The floating potential of the dust particle is denoted by ϕ_f, and

$$b_c=a\left(1-\frac{2q_i\phi_f}{m_i v_s^2}\right)^{1/2}, \tag{7}$$

is the maximum impact parameter for dust-ion collision from the orbital motion limited probe theory (OML).

Further, the orbital force can be written as

$$F_{\text{Coulomb}}=4\pi n_i m_i u_i v_s b_{\pi/2}^2 \Gamma, \tag{8}$$

where

$$b_{\pi/2}=\frac{eQ_p}{4\pi\epsilon_0 m_i v_s^2} \tag{9}$$

is the impact parameter for 90° deflection, and

$$\Gamma=\frac{1}{2}\ln\left(\frac{\lambda_D^2+b_{\pi/2}^2}{b_c^2+b_{\pi/2}^2}\right) \tag{10}$$

is the Coulomb logarithm integrated over the interval (b_c,λ_D). Here, n_i, m_i, T_i, q_i, and u_i are the number density, mass, temperature, charge and drift velocity of the ions, k_B is Boltzmann's constant, λ_D is the Debye length, and ϕ_f is the floating potential of the dust particle relative to the local plasma potential.

For usual particle dimensions of a few micrometers, thermophoresis produces a measurable effect when the temperature gradient is of the order of a few Kelvin per centimeter. The microscopic mechanism of this force lies in the fact that on the side of the particle oriented towards the hotter gas regions, the gas molecules hit the particle with a higher thermal velocity than on the side facing the colder regions. This results in an effective momentum transport opposite to the temperature gradient. The force then reads[39,40]

$$\mathbf{F}_{\text{thermo}}=-\frac{16}{15}\sqrt{\pi}\frac{a^2\lambda}{v_{\text{th}}}\nabla T_n, \tag{11}$$

where λ is the translational part of heat conductivity of the gas.

Usually, the particles charge negatively in plasma in the absence of other processes like electron photoemission. In an unperturbed plasma the walls are (time averaged) negatively

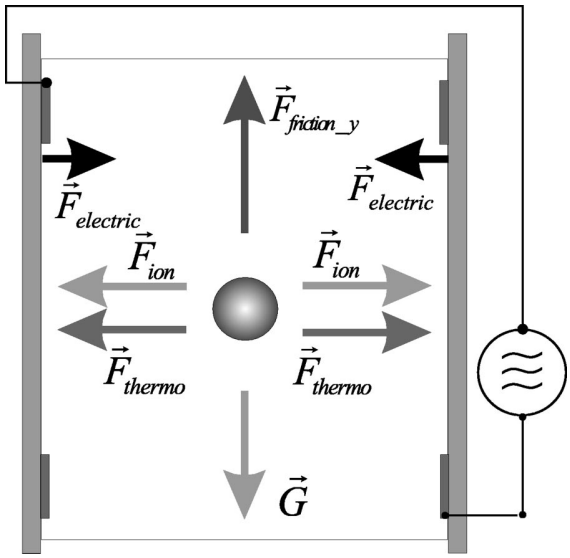

FIG. 1. Scheme of the forces acting radially on the dust particles. Their balance determines the particle trajectory.

polarized with respect to the bulk plasma. Also within the bulk plasma small electric fields prevail due to ambipolar diffusion. This results in a confining electric field force on the negative particles,

$$\mathbf{F}_{\text{electric}} = -Q_p \mathbf{E}; \quad \mathbf{E} = -\nabla \phi_{\text{pl}}, \tag{12}$$

where ϕ_{pl} is the plasma potential and $Q_p = 4\pi\epsilon_0 a \phi_f$ is the particle charge.

Finally, the horizontal friction force is analogous to the vertical one

$$\mathbf{F}_{\text{frict}\_x} = -m\beta \dot{\mathbf{x}}. \tag{13}$$

Considering all the forces which act on the horizontal direction, the dynamic equilibrium is described by the balance of these forces,

$$F_{\text{ion}} + F_{\text{thermo}} - F_{\text{electric}} = F_{\text{frict}\_x} + m\ddot{x}, \tag{14}$$

where on the RHS the forces determined from the particle trajectories and neutral gas friction are given and on the LHS the forces obtained from the analysis of the plasma parameters and the neutral gas temperature (see Fig. 1). In the following we will call the sum of ion drag, thermophoresis and electric field force ''plasma force'' because they are determined by the presence of plasma and the sum of inertia and friction force ''trajectory force,'' which is obtained from the particle trajectory analysis. The electric field force is a confining force, whereas the ion drag and thermophoresis point outwards.

III. EXPERIMENTAL SETUP

The experiments have been performed in a long tube [see Fig. 2(a)] with a total length of 120 cm and a internal

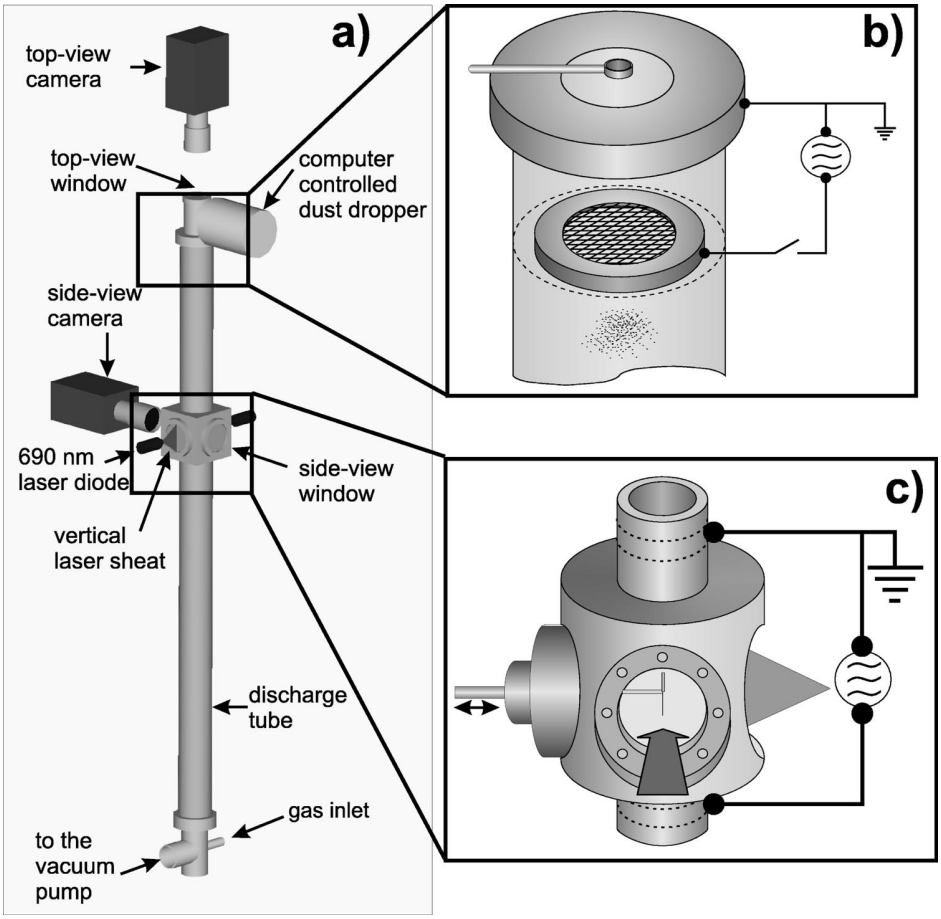

FIG. 2. (a) General scheme of the experimental setup; (b) setup of the auxiliary discharge for particle separation; (c) detailed view of the observation level with the Langmuir/temperature probe.

diameter of 50 mm. Monodisperse spherical particles made of melamine formaldehyde (MF) ($a=9.55\ \mu$m diam) are dropped from the top of the tube, using an automatic dust dropper. The dust cloud is observed about 30 cm below the injection to ensure the vertical constant drift regime of the dust. The observation level [see Fig. 2(c)] is a plastic box between two glass tubes, providing optimal image recording conditions due to the flat windows. The discharge is operated in helium at pressures of 100, 150, and 200 Pa using two internal copper ring electrodes positioned in the glass tubes at upper and lower ends of the observation level. The lower electrode is powered with 0.8, 1.6, 2.0, 2.3, and 2.6 W at 13.56 MHz while the upper one, as well as the metallic flanges positioned at the top and bottom of the experiment are grounded. The falling particles are illuminated through the side windows using a thin vertical laser sheath with a power density of about 10 mW/mm^2. The laser power has been modulated by a periodic rectangle waveform at 400 Hz, providing a stroboscopic illumination. A camera with tunable frame rate has been used for image recording perpendicular to the laser sheath. This enables the observation of vertical cross sections of the dust cloud. The dust images have been recorded and processed on a PC. The stroboscopic illumination increases the time resolution of the image recording and it is suitable even in combination with normal video cameras. A long exposure regime of the camera (about 20 frames per second) has been used here, so that the particle trajectories look like dotted lines on the recorded images [see Fig. 4(a)].

A. Determination of the plasma parameters

The plasma parameters have been evaluated from Langmuir probe measurements. For each set of experimental conditions, probe measurements have been performed without dust, assuming that the presence of a small number of particles does not influence the plasma parameters significantly. In Sec. V the consistency of such an assumption will be analyzed. Radial profiles of the plasma parameters are recorded with a resolution of 30–35 points/profile. A compensated cylindrical probe, 6.90 mm long and 0.05 mm in diameter, with the compensation electrode 10 mm long and 0.8 mm diameter has been used here.

Plasma parameters have been determined from probe measurements using standard procedures. The electron temperature has been found analyzing the ionic part of the probe characteristic, from the slope near the floating potential V_{float} (see Ref. 41),

$$T_e = eI_{if}\left(\frac{dI_e}{dV}\right)^{-1} = eI_{if}\left(\frac{dI_p}{dV}-\frac{dI_i}{dV}\right)^{-1} \tag{15}$$

evaluated at $V=V_{\text{float}}$, where I_{if} is the linear extrapolation of the ion current to the floating potential, dI_p/dV, dI_e/dV, and dI_i/dV are the plasma, electron, and ion current slope at the floating potential. The electron temperature has been found to be almost radially constant at 6 eV. The plasma density has been deduced using the Langmuir formula.[41] It has been found to be almost parabolic with the maximum of 4.1×10^{15} m^{-3} in the center of the discharge and 1.3×10^{15} m^{-3} at about 40 mm from center.

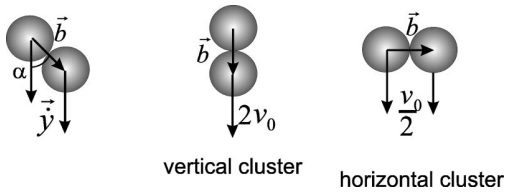

FIG. 3. The falling velocity of a two-particle cluster strongly depends on its orientation.

B. Temperature measurements

The radial neutral gas temperature profile has been measured in order to determine the temperature gradient and thus the thermophoretic force. A temperature probe consisting of a thermoresistor has been used here for horizontal profile measurements with a spatial resolution of 1 mm. Due to the long recording time of a temperature profile, an additional thermoresistor has been placed in thermal contact with the chamber wall in order to measure and to extract the temperature drift of the whole experiment. For our plasma conditions, the ion density is about 10^{-5} of the neutral gas density and the ion drift velocity has a maximum value of about 10% of the ion thermal velocity, so that drift ion currents that reach the thermoresistor should have a negligible contribution to the temperature measurements. This gives us confidence that the temperature measurements are accurate enough and no drift ion contribution has to be taken into account in the temperature analysis.

C. Particle cluster separation

It is known that small dust particles have the tendency to form clusters due to adhesion. Since the forces acting on a cluster of several particles are different from those acting on a single particle, it has to be ensured that only single grains are analyzed. To show this, the behavior of a free-falling two-particle cluster will be analyzed. The dynamic vertical equilibrium is approximatively described by

$$2mg-\kappa\tilde{\beta}m\pi a^2\dot{y}=0, \tag{16}$$

with the orientation coefficient (see Fig. 3)

$$\kappa=1+|\sin\alpha|. \tag{17}$$

Here, $\tilde{\beta}=\beta/(\pi a^2)$, α is the angle between the distance vector of the two particles **b** and the vertical velocity vector $\dot{\mathbf{y}}$, and β is the friction coefficient for a single grain. It is evident that, if **b** is parallel to the velocity vector $\dot{\mathbf{y}}$, the cluster will fall with a constant velocity twice as high as the velocity of a single particle. If the distance vector is perpendicular to the velocity, the cluster velocity is the same as the velocity of a single particle. Between these two extreme situations, depending on the cluster orientation, the constant falling velocity continuously varies between once and twice the one-particle velocity. In reality, the high complexity of clusters and their eventual rotation involves a broad distribution of measured velocities, so it is considered as a source of experimental errors. The higher the particle number in a cluster, the faster the cluster will fall, so that single particles will have

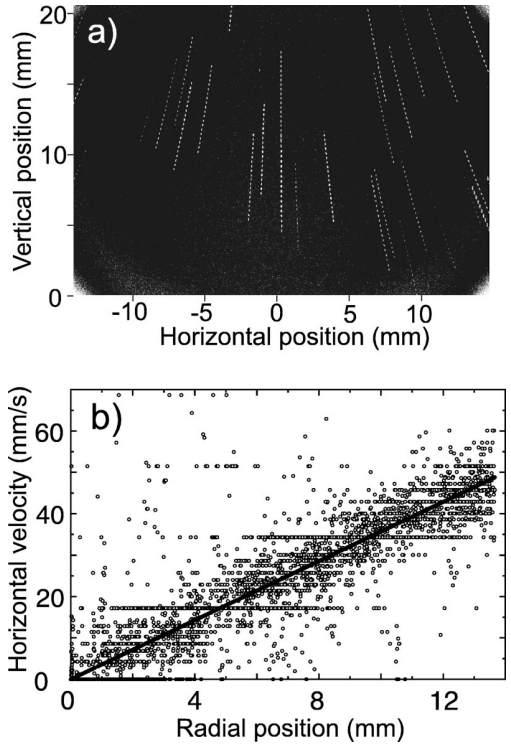

FIG. 4. (a) Single video image of the falling particles and (b) radial velocity distribution of the falling particles in a plasma driven at a pressure of 150 Pa and a power of 2.6 W, as a function of the radial particle position.

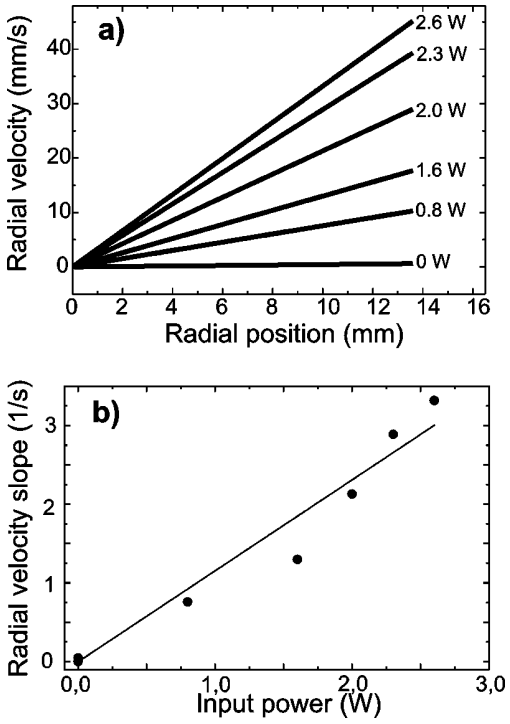

FIG. 5. (a) Radial velocities for various input powers (0–2.6 W) as a function of radial position. The radial velocity increases with increasing power. (b) The slope of the radial velocity increases almost linearly with the input power. Pressure: 150 Pa, particle diameter $d=9.55\ \mu$m.

the lowest velocity. This kind of error affects not only the vertical, but also the horizontal velocity measurements. Therefore, it is desirable to have most of the particle cluster separated.

For this aim, an additional rf funnel-shaped electrode with a grid bottom is positioned about 50 mm below the grounded vacuum flange [see Fig. 2(b)]. The clusters, as well as the single particles are trapped for several seconds above the grid in order to ''Coulomb explode'' the clusters due to their high negative charge. When this auxiliary discharge is turned off, the trapped particles are released and fall towards the main discharge. It has been observed that not all the clusters are separated due to various reasons. Additionally, as long as the dust is trapped, a vertical separation between the lighter single particles and the heavier still unexploded clusters occurs, which increases when the discharge is switched off and particles are released. At the observation level, the particle cloud consists of a fast moving cluster group followed after a few tenths of a second by a cloud formed of single particles. All the measurements have been done on this second group which consists mainly of single grains.

IV. MEASUREMENT: DETERMINATION OF THE FORCES ACTING ON THE PARTICLES

A. Analysis of the particle trajectories

Figure 4(a) shows the recorded image of falling dust for a pressure of 150 Pa and an input power of 2.6 W. For a high enough rf input power, the recorded images show that the particles are pushed out of the plasma. It has been shown in Sec. II how the force balance defines the particle trajectories. A detailed analysis on a large number of pictures of dust particles falling through the plasma shows that the radial velocity increases almost linearly with increasing radial coordinate [Fig. 4(b)]. The scattered values of the radial velocity with an error range of about 10% are caused by the pixel resolution of the recorded images. The slope of the radial velocity increases almost linearly [see Fig. 5(a)] with the power of the discharge [see Fig. 5(b)]. This overall behavior shows that the confining electric force is outrun by other outwards-pointing forces, like thermophoresis or/and ion drag, and that this unbalance increases with increasing power.

The horizontal acceleration of the particles is

$$\ddot{\mathbf{x}}=\frac{d\dot{\mathbf{x}}}{dt}, \tag{18}$$

where $\dot{x}=\dot{x}(x(t),t)$. Inserting this, yields

$$\ddot{\mathbf{x}}=\frac{\partial\dot{\mathbf{x}}}{\partial\mathbf{x}}\frac{d\mathbf{x}}{dt}+\frac{\partial\dot{\mathbf{x}}}{\partial t}. \tag{19}$$

Considering the accelerated horizontal motion as a global motion characteristic for all the particles [see Fig. 5(a)], with the radial velocity dependent only on radial position, and not on time, then $\partial\dot{x}/\partial t=0$. The horizontal acceleration then becomes

$$\ddot{\mathbf{x}}=\frac{\partial\dot{\mathbf{x}}}{\partial\mathbf{x}}\frac{d\mathbf{x}}{dt}=\dot{\mathbf{x}}\frac{\partial\dot{\mathbf{x}}}{\partial\mathbf{x}}, \tag{20}$$

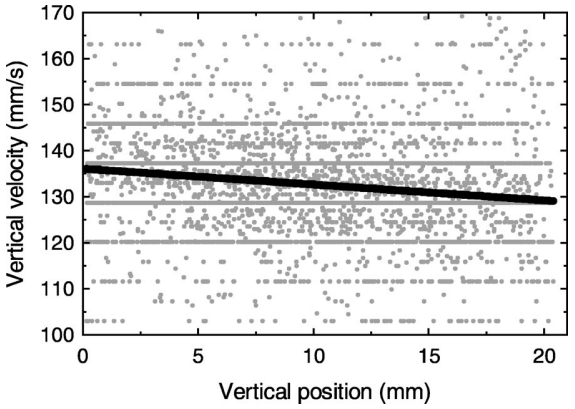

FIG. 6. Vertical velocity distribution; the particles are falling with a constant speed.

which can be precisely measured from the radial velocity distribution of the particles for each experimental condition. This is in fact the convective derivative applied to the velocity vector. It is usually applied in the study of fluid mechanics for a stationary flow pattern.

The analysis of particle trajectories in the vertical direction shows that the particles fall with a nearly constant vertical velocity, as it can be seen in Fig. 6, giving us confidence that no additional inhomogeneous force acts on the vertical direction. This leads to the idea that the plasma is vertically almost homogeneous in the observation region. Again, the measured vertical velocities are spread within an error of about 7%. A typical indication for the pixel-limited resolution is the clear tendency of the vertical velocity to take preferred equidistant values. Equating the mean vertical velocity in the equation of dynamical vertical equilibrium [Eq. (2)], the neutral friction constant has been determined and has been further used in the horizontal motion analysis. A certain mismatch between the measured and the theoretical velocity [see Eq. (2)] has been observed, which increases with decreasing gas pressure. For the worst case at 100 Pa the mismatch reaches 50%. Here, the drag coefficient computed using the measured vertical velocity has been used for the whole analysis.

The "trajectory forces" in the equation of dynamic horizontal equilibrium (friction and inertia force) are then given by

$$\mathbf{F}_{\text{traject}} = m\left[\frac{d\dot{\mathbf{x}}}{d\mathbf{x}} + \beta\right]\dot{\mathbf{x}}. \tag{21}$$

These trajectory forces have to be balanced by the sum of the plasma forces F_{plasma}, namely, thermophoresis, ion drag, and electric field force.

B. Electric field force

The particle charge is needed for equating the electric force equation. As usual, it is determined by the floating potential of a spherical probe assuming a spherical capacitor model for the particle. The floating potential has been obtained solving the equation of ion and electron current balance from OML theory using the electron temperature determined from the probe measurements, yielding

$$1 - \frac{e\phi_f}{k_B T_e}\frac{T_e}{T_i} = \sqrt{\frac{m_i}{m_e}\frac{T_e}{T_i}}\exp\left(\frac{e\phi_f}{k_B T_e}\right), \tag{22}$$

where the ion temperature T_i has been considered to be equal to room temperature. These equations are justified for the case of plasmas where the charge carriers do not exhibit any drift motion. When the drift velocity u_i of the ions is taken into account, the ion current is defined by[42]

$$I_i = \pi a^2 n_i e u_i \left\{\left(1 + \frac{v_{\text{th}}^2}{2u_i^2} - \frac{U^2}{u_i^2}\right)\cdot \text{erf}\left(\frac{u_i}{v_{\text{th}}}\right) + \frac{v_{\text{th}}}{\pi^{1/2}u_i}\exp\left[-\left(\frac{u_i}{v_{\text{th}}}\right)^2\right]\right\}, \tag{23}$$

where $U = \sqrt{2q\phi_f/m_i}$ and $v_{\text{th}} = \sqrt{2k_B T/m_i}$ the ion thermal velocity. Balancing this by the electron current

$$I_e = \pi a^2 n_e e \sqrt{\frac{8k_B T_e}{\pi m_e}}\exp\left(\frac{e\phi_f}{k_B T_e}\right), \tag{24}$$

the floating potential ϕ_f can be numerically obtained. It was observed that for our case where $u_i < 0.2\, v_{\text{th}}$, the difference between the OML and the drifting ion current is insignificant.

The electric field profile has been determined from the Langmuir probe measurements. The electric field force then is

$$F_{\text{electric}} = 4\pi\varepsilon_0 a\phi_f \frac{d\phi_{\text{pl}}}{dx}, \tag{25}$$

where ϕ_f has been obtained from Eqs. (22) and (23), and ϕ_{pl} from the probe measurements.

C. Ion drag force

The ion drift velocity has been computed from the radial electric field of the plasma column by $\mathbf{u}_i = \mu\mathbf{E}$. μ is the mobility of singly ionized ions in the neutral environment of their parent gas and is given for helium by $\mu = 0.143\ \text{kg m s}^{-3}\,\text{K}^{-1}$.[43]

Figure 7(a) shows that a nearly parabolic radial potential profile of the plasma column is observed, which produces a radially symmetric ion drag force.

The ion drag has been computed using Eqs. (5) and (8), which are justified for the collisionless situation (low gas pressure), which is not exactly our case. Our experiments have been performed at higher pressures, where the mean free path of charge exchange collisions is smaller than the Debye length. We are not aware of any ion drag model where charge exchange collisions are taken into account, so the collisionless model has been implemented here.

D. Thermophoretic force

The temperature distribution has been measured, as presented in Sec. III. Figure 7(b) shows the nearly parabolic horizontal temperature distribution, which is responsible for a linearly increasing radial thermophoretic force. The mea-

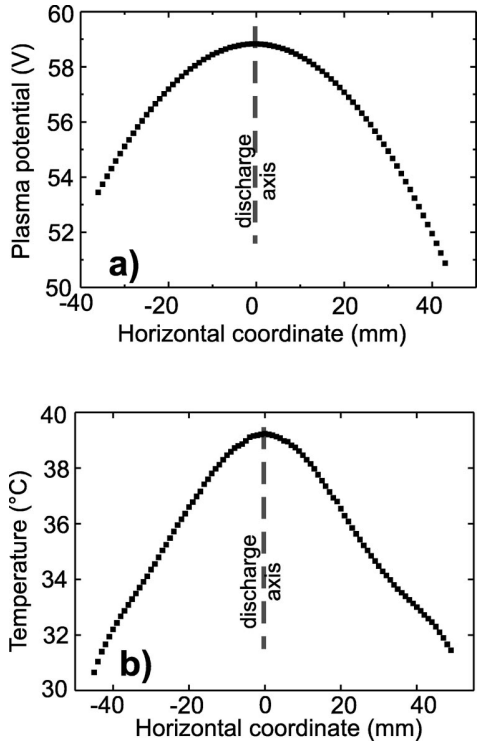

FIG. 7. (a) Radially symmetric electric potential distribution and (b) nearly parabolic radial temperature distribution of an unperturbed plasma, for a power of 2.6 W.

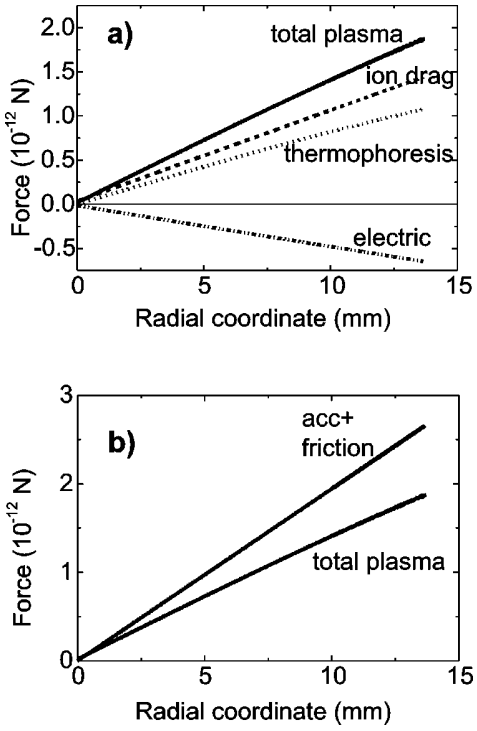

FIG. 8. (a) Plasma forces (thermophoresis+ion drag+electric field force), for the symmetrical temperature and potential distribution case and (b) comparison of the measured "trajectory force" obtained from the particle trajectory analysis taking into account the friction with the total plasma force.

sured profile can be compared to the solution of the heat diffusion equation with homogeneous energy input for the cylindrical geometry of the experiment,

$$\nabla T = -\frac{P\mathbf{r}}{2\pi R_{\text{tube}}^2 L\lambda}, \tag{26}$$

where P is the input power, R_{tube} and L the radius and the length of the plasma tube, and r is the radial coordinate. For this estimation, it is assumed that the whole rf power is transformed into heat in the plasma column. However, this leads to a systematic overestimation of the temperature gradient and thus of the thermophoretic force with up to 50% as compared to the experimental results. This might result from the fact that a considerable part of the input power is used by the plasma itself for ionization, or from the energy losses at the upper and lower ends of the plasma, which have not been taken into account. For the analysis of the thermophoretic force the measured temperatures are taken.

E. Results for the symmetric case

Finally, the results of of the force measurements for the radially symmetric plasma profiles are presented here. The observed symmetry of the potential and temperature profiles allows us a radial analysis of the problem.

The comparison between the total trajectory force and the sum of the plasma forces (thermophoresis, ion drag, and electric field force) is represented in Fig. 8. The electric field force acts as a confining force, so it has been represented as negative, whereas the ion drag and thermophoresis point outwards. Trajectory and plasma forces agree within an error of 30%. The measured trajectory forces are slightly larger than the sum of outward thermophoresis and ion drag forces and the inward electric field force. A detailed analysis will be presented in Sec. V.

It is important to state here that the confining electric force is much smaller than the sum of thermophoretic force and ion drag. The situation is the same for other gas pressures or input powers. This shows that, at least for helium, in this experimental configuration, no confinement can be expected.

F. Modified temperature profile

In order to extend our studies on thermophoresis and ion drag forces, experiments under modified temperature conditions have been performed in order to establish regions in the plasma where ion drag and thermophoresis have opposite directions. Therefore an external heat source has been added at the observation level. This heat source consists of a Peltier element of 18.7 W. The hot plate has been set in thermal contact with one of the side windows (the left side in the recorded particle images), while the cold plate has been kept at room temperature. The maximum temperature difference between the cold and the hot plate supplied by this model of Peltier element can be up to 60 °C, which is enough to change the direction of the thermophoresis.

Polymethyl methacrylate (PMMA) particles ($a = 20.02$ μm diam) are dropped through the same experimental setup using the same technique. The particle trajectories

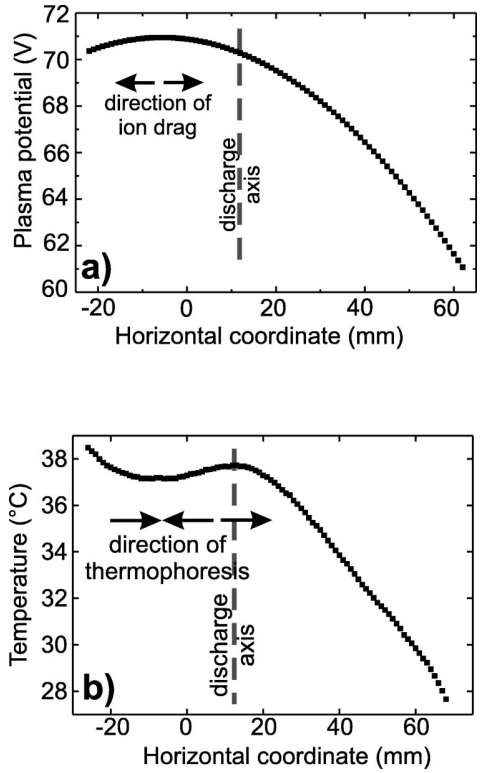

FIG. 9. (a) Horizontal electric potential distribution and (b) modified horizontal temperature distribution in the case of the plasma with the external heat source. The heat source is mounted to the left side window (horizontal position $x=-28$ mm).

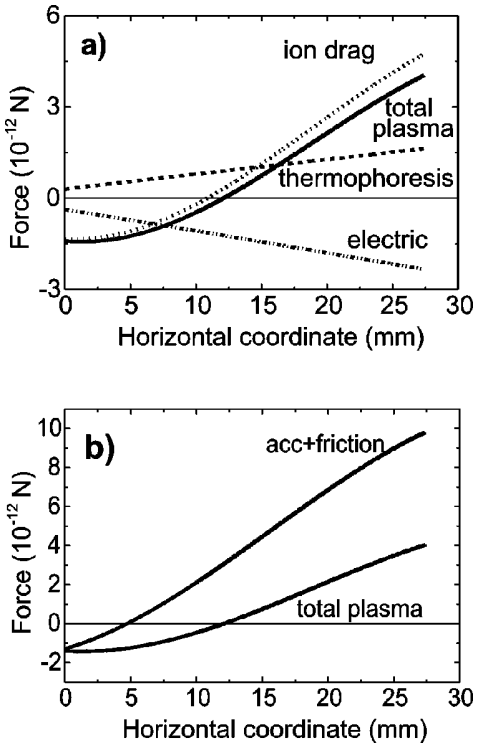

FIG. 10. (a) Plasma forces (thermophoresis+ion drag+electric field force) for the asymmetrical temperature and potential distribution case and (b) comparison of the measured trajectory force from the particle trajectories analysis taking into account the friction with the total plasma force.

are again analyzed and the horizontal and vertical velocities are extracted. Temperature and Langmuir probe measurements have been performed, as in the symmetric case. The electron temperature is again found to be almost constant at 6.5 eV. Figures 9(a) and 9(b) show the temperature profile and the plasma potential distribution. For this case the temperature profile is visibly modified due to the heat source. The plasma potential is also modified due to the use of quite large metallic pieces of the heat source in the vicinity of the plasma. The profile is still parabolic, but shifted towards the heat source [see Fig. 9(a)]. The same occurs for the plasma density profile. It has the maximum density of 5.9×10^{15} m^{-3} shifted towards the heated window. For these modified condition, the arrows indicate the direction of drift for the positive ions accelerated in the plasma electric field, and thus of the ion drag, and the direction of thermophoresis.

For this modified asymmetric temperature case, horizontal Cartesian coordinates are used, with the origin corresponding to the left side of the recorded images of the falling particles. They must not be confused with the radial coordinate used in the symmetric case.

In Figs. 10(a) and 10(b), both the trajectory force measured from the particle trajectories, taking into account the neutral gas friction, and the plasma forces (ion drag, thermophoresis, and electric force) have been plotted. Again, the confining electric force is much smaller than the sum of thermophoresis and ion drag. In this case the difference between the total trajectory and plasma forces is measured to be about 50%.

V. RESULTS AND DISCUSSIONS

The measured trajectory force, which is the total force computed from the accelerated outward motion taking into account the friction force has been compared with the sum of the plasma forces (ion drag, thermophoresis, and electric field force). A reasonable agreement between trajectory and plasma forces can be observed in both cases. For the radially symmetric plasma the forces agree within 30% while for the asymmetric case within 50%

Figure 11 shows the relative difference $(F_{\text{traject}}-F_{\text{plasma}})/F_{\text{traject}}$ between the outward and inward force for two different pressures and for various input powers. It can be observed that for very low powers, the difference is negative, which means that the measured sum between ion drag, thermophoresis and electric field force is slightly larger than the trajectory force on the falling particles. For 150 Pa, 2.3 W the highest mismatch occurs. This can be correlated to the fact that for these experimental conditions the dust dropper has been freshly refilled, so that a huge number of particles were injected into the plasma column. A high number of particles which simultaneously fall through the plasma column can have two effects which have been not discussed so far.

A high dust particle density considerably perturbs the electron and ion densities. When a huge amount of particles is dropped into the plasma it can be observed with the naked

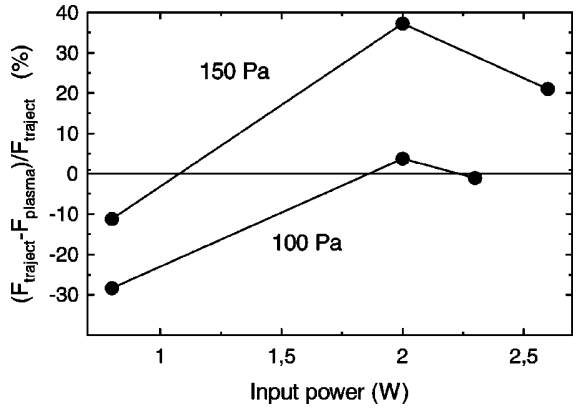

FIG. 11. The relative difference between the "trajectory force," which is the total force computed from the particle trajectory analysis taking into account the friction, and the "total plasma force," which is the sum between the ion drag, thermophoresis, and electric field force.

eye that the discharge tends to extinguish. When dust is introduced, the free electron density decreases due to the negative charge attached to the particles. The unbalance between free electrons and ions increases with the number of particles, affecting both the charging process and the electric field distribution inside the plasma. It is very difficult to measure this effect *in situ* due to the time-variable number of particles. The probe measurement has been performed in a particle-free plasma because it is practically impossible to record a complete plasma parameter profile within the few fractions of second when the particles fall. Therefore the plasma parameters recorded in a particle-free plasma have to be corrected. A decrease of the electron density can be introduced into our analysis in order to check its influence on the force balance. Figure 12 shows the change of the ion drag, thermophoresis and electric force on the particles with variation of the n_e to n_i ratio. As expected, this ratio has no effect on the thermophoretic force, but the electric and ion drag show some variation. The ion drag is described by a function which is not injective. This complex behavior results from the complicated dependency of the various quantities in the ion drag equation on the electron and ion densities. For increasing n_e/n_i, up to the maximum value at $n_e/n_i \approx 0.3$, the increase of the particle charge is dominant, whereas for $n_e/n_i > 0.3$ the decrease of the Coulomb logarithm predominates. Also the electric field force is seen to increase with n_e/n_i. This increase is the result of two competing effects: with increasing n_e/n_i, the electric field $E=\nabla\phi_{\mathrm{pl}}$ in the plasma decreases, but simultaneously, it can be related to an increase of the particle charge due to the higher electron density. The curve shown in Fig. 12 shows that the variation of charge is dominant.

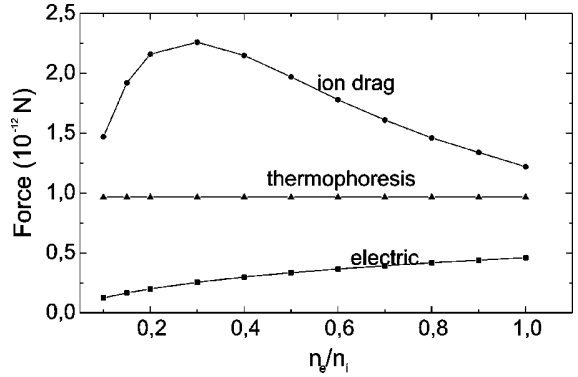

FIG. 12. Behavior of the ion drag, thermophoresis, and electric force with the ratio n_e/n_i as an effect of electro density reduction due to the high number of particulates. As expected, thermophoresis is not affected, whereas the ion drag is characterized by a nonmonotonous function.

With the ratio n_e/n_i a considerable change of the general match of the trajectory and plasma forces can be observed. For 150 Pa and 2.6 W, a perfect match can be obtained for two different values $n_e/n_i=0.6$ and $n_e/n_i=0.15$. A reduction of 40% of the electron density might be reasonable (a reduction by 85% seems to be out of range). However, a quantitative analysis of n_e/n_i from this results would be speculative.

For a plasma containing very few dust, the interparticle distance is usually much larger than the screening length, so the mutual repulsion between neighboring grains is not important. With the increase of the dust density, the interparticle distance correspondingly decreases to values close and below the screening length. In this case, the mutual repulsion can have a considerable contribution to the total force, which pushes the particles out of the discharge. Again this effect is quite difficult to be estimated because of the time-variable number of grains, and due to the space-variation of particle density inside the dust cloud.

For the lowest input power, the sum of measured values of thermophoresis, ion drag, and electric field exceed the trajectory forces. This can be related to measurement errors. For low power the outwards bending of the particle trajectories is quite small, also the probe measurements are much more noisy, so that quite large errors are expected.

For the case where the temperature field has been modified, the match is within 50% mainly as a result of the fact that in this special case of asymmetric temperature and potential profile, systematic errors in the Langmuir probe and temperature analysis could not be compensated as in the symmetric case. The Langmuir probe measurement is mainly affected by the presence of the probe holder being more or less inside the plasma. If at the beginning of a profile recording the holder is completely outside the plasma, at the end it is completely in contact with the plasma. The result is an increased asymmetry of the profile. For the symmetric case this error could be compensated by averaging both ascendent and descendent arm of the horizontal profile. Also the temperature measurements are affected by heat transport to the probe holder. When the probe is in contact with colder temperature regions than the holder, then a heat flow occurs from the holder to the probe. When the probe is hotter than the holder, the heat flows vice versa. In the symmetrical case this problem can again be compensated by averaging. Therefore, it is reasonable to expect that the asymmetric case is affected by higher measurement errors, thus the match is slightly worse.

After all the experimental problems listed here, a short overview of the reliability of the measured forces is neces-

sary. In the inward direction, the dominant force is the acceleration and friction forces measured from the outward particle motion. A large number of particle trajectories has been analyzed here, so the measurement accuracy is very high. Thus, an eventual lack of precision in measurement of the electric field force, derived from probe measurements, has only a small influence on the total inward pointing force. For the outward direction, the ion drag and thermophoresis have comparable magnitudes. Thermophoresis has been quite accurately estimated using the measured temperature profiles. The ion drag however, due to the complicated dependency on plasma parameters is susceptible to larger errors. The underlying ion drag equations[36] are suitable for our experimental conditions with limitations.

Until now, enhancements of 10 times[35] or of 40 times[44] of the ion drag have been stated. From our results, only moderate enhancements of up to 50% might be neccesary, depending on the experimental conditions.

ACKNOWLEDGMENTS

This work was supported by DFG under Grant No. Pi 185-17/1,2.

[1] A. Bouchoule, *Dusty Plasmas: Physics, Chemistry, and Technological Impacts in Plasma Processing* (Wiley, New York, 1999).
[2] A. Piel and A. Melzer, Plasma Phys. Controlled Fusion **44**, R1 (2002).
[3] G. S. Selwyn, J. E. Heidenreich, and K. L. Haller, J. Vac. Sci. Technol. A **9**, 2817 (1991).
[4] J. H. Chu and L. I, Phys. Rev. Lett. **72**, 4009 (1994).
[5] H. Thomas, G. E. Morfill, V. Demmel, J. Goree, B. Feuerbacher, and D. Mhlmann, Phys. Rev. Lett. **73**, 652 (1994).
[6] Y. Hayashi and K. Tachibana, Jpn. J. Appl. Phys., Part 1 **33**, L804 (1994).
[7] A. Melzer, T. Trottenberg, and A. Piel, Phys. Lett. A **191**, 301 (1994).
[8] A. Melzer, A. Homann, and A. Piel, Phys. Rev. E **53**, 2757 (1996).
[9] H. Thomas and G. E. Morfill, Nature (London) **379**, 806 (1996).
[10] A. Homann, A. Melzer, S. Peters, and A. Piel, Phys. Rev. E **56**, 7138 (1997).
[11] A. Homann, A. Melzer, S. Peters, R. Madani, and A. Piel, Phys. Lett. A **242**, 173 (1998).
[12] S. Nunomura, J. Goree, S. Hu, X. Wang, and A. Bhattacharjee, Phys. Rev. E **65**, 066402 (2002).
[13] D. Samsonov, J. Goree, Z. W. Ma, and A. Bhattacharjee, Phys. Rev. Lett. **83**, 3649 (1999).
[14] D. Samsonov, J. Goree, H. M. Thomas, and G. E. Morfill, Phys. Rev. E **61**, 5557 (2000).
[15] A. Melzer, S. Nunomura, D. Samsonov, and J. Goree, Phys. Rev. E **62**, 4162 (2000).
[16] O. Havnes, T. W. Hartquist, A. Brattli, G. M. W. Kroesen, and G. Morfill, Phys. Rev. E **65**, 045403 (2002).
[17] V. Nosenko, J. Goree, Z. W. Ma, and A. Piel, Phys. Rev. Lett. **88**, 135001 (2002).
[18] V. A. Schweigert, I. V. Schweigert, A. Melzer, A. Homann, and A. Piel, Phys. Rev. E **54**, 4155 (1996).
[19] F. Melandsø and J. Goree, Phys. Rev. E **52**, 5312 (1995).
[20] M. Nambu, S. V. Vladimirov, and P. K. Shukla, Phys. Lett. A **203**, 40 (1995).
[21] A. Melzer, V. Schweigert, and A. Piel, *Advances in Dusty Plasmas—Proc. 2nd ICPDP* (Elsevier, Amsterdam, 2000), p. 115.
[22] A. Melzer, V. A. Schweigert, and A. Piel, Phys. Scr. **61**, 494 (2000).
[23] K. Takahashi, T. Oishi, K. Shimomai, Y. Hayashi, and S. Nishino, Phys. Rev. E **58**, 7805 (1998).
[24] V. A. Schweigert, I. V. Schweigert, A. Melzer, A. Homann, and A. Piel, Phys. Rev. Lett. **80**, 5345 (1998).
[25] I. V. Schweigert, V. A. Schweigert, A. Melzer, and A. Piel, Phys. Rev. E **62**, 1238 (2000).
[26] T. Trottenberg, A. Melzer, and A. Piel, Plasma Sources Sci. Technol. **4**, 450 (1995).
[27] J. Pieper, J. Goree, and R. Quinn, Phys. Rev. E **54**, 5636 (1996).
[28] M. Zuzic, A. V. Ivlev, J. Goree, G. E. Morfill, H. M. Thomas, H. Rothermel, U. Konopka, R. Stterlin, and D. D. Goldbeck, Phys. Rev. Lett. **85**, 4064 (2000).
[29] G. E. Morfill, H. M. Thomas, U. Konopka, H. Rothermel, M. Zuzic, A. Ivlev, and J. Goree, Phys. Rev. Lett. **83**, 1598 (1999).
[30] H. M. Thomas, D. D. Goldbeck, T. Hagl, A. V. Ivlev, U. Konopka, G. E. Morfill, H. Rothermel, R. Sütterlin, and M. Zuzic, Phys. Scr. **89**, 16 (2001).
[31] G. S. Selwyn, J. Vac. Sci. Technol. A **9**, 3487 (1991).
[32] J. L. Dorier, C. Hollenstein, and A. A. Howling, J. Vac. Sci. Technol. A **13**, 918 (1995).
[33] J. Goree, G. E. Morfill, V. N. Tsytovich, and S. V. Vladimirov, Phys. Rev. E **59**, 7055 (1999).
[34] V. N. Tsytovich, S. V. Vladimirov, G. E. Morfill, and J. Goree, Phys. Rev. E **63**, 056609 (2001).
[35] M. R. Akdim and W. J. Goedheer, Phys. Rev. E **65**, 015401 (2002).
[36] M. S. Barnes, J. H. Keller, J. C. Forster, J. A. O'Neill, and D. K. Coultas, Phys. Rev. Lett. **68**, 313 (1992).
[37] P. S. Epstein, Phys. Rev. **23**, 710 (1924).
[38] J. Perrin, P. Molinás-Mata, and P. Belenguer, J. Phys. D **27**, 2499 (1994).
[39] O. Havnes, T. Nitter, V. Tsytovich, G. E. Morfill, and T. Hartquist, Plasma Sources Sci. Technol. **3**, 448 (1994).
[40] T. Nitter, Plasma Sources Sci. Technol. **5**, 93 (1996).
[41] V. A. Godyak, R. B. Piejak, and B. M. Alexandrovich, J. Appl. Phys. **73**, 3657 (1993).
[42] E. C. Whipple, Rep. Prog. Phys. **44**, 1197 (1981).
[43] U. Grigull and H. Sandner, *Wärmeleitung* (Springer-Verlag, Berlin, 1979).
[44] S. A. Khrapak, A. I. Ivlev, G. E. Morfill, and H. M. Thomas (unpublished).

B Reprints of Selected Conference Papers

B.1

NONLINEAR OSCILLATIONS OF PARTICLES IN THE SHEATH OF DUSTY PLASMAS

C. Zafiu, A. Melzer and A. Piel

XVth Europhysics Conference on Atomic
and Molecular Physics of ionized Gases
ESCAMPIG-2000 Miskolc-Lillafüred, Hungary
Abstracts of Invited Lectures and Contributed Papers
European Physics Society 2000, Pages 132-133

Nonlinear Oscillations of Particles in the Sheath of Dusty Plasmas

C.Zafiu, A. Melzer, A.Piel

Institut für Experimentelle und Angewandte Physik, Christian-Albrechts-Universität Kiel, 24098 Kiel, Germany

Introduction

Dusty plasma have attained an enormous interest in the last few years because of their widespread applications in astrophysical phenomena and new plasma processing technologies. Plasmas containing small (nanometer to micrometer) dust grains could be found in planetary rings, comets, nebulae, and noctilucent clouds observed in the polar summer mesosphere. Even more important, dusty plasmas play a crucial role in laboratory devices such as microchip processing plasmas where particle formation poses a serious problem of contamination, or in low temperature discharges using reactive gases for particle growth and manufacturing of nano-powders and new materials. Because of their large size and mass compared to the plasma ions and electrons the dust particles act as small probes, collecting ion and electron currents and and thus attaining a high negative charge due to the higher mobility of electrons. Because of the high charges, the particles strongly interact by repulsive Coulomb forces, so that the charged dust particles can form regular structures, like crystals (the so-called dust crystals).
In typical experiments, micrometer sized particles are trapped in the ionic space charge sheath of an RF capacitive discharge. There, an electric field levitates the charged dust particles against gravity. Earlier investigations treated the electric field as linearly increasing from the plasma edge to the lower electrode. This defines a parabolic shape for the effective potential well acting on the particle. This well also determines the equilibrium position for the dust particle where the electric force balances the gravity (see Fig.1b). Using a low amplitude modulation of the RF voltage, the linear resonance curve of an oscillating particle in this potential well has been measured in order to determine the particle charge [1].
In the experiment presented here, the particle trapping in the space charge sheath is investigated, taking into account non-linear effects. This allows to study non-linear contributions of the sheath electric field and space-dependent dust charges.

Experiment

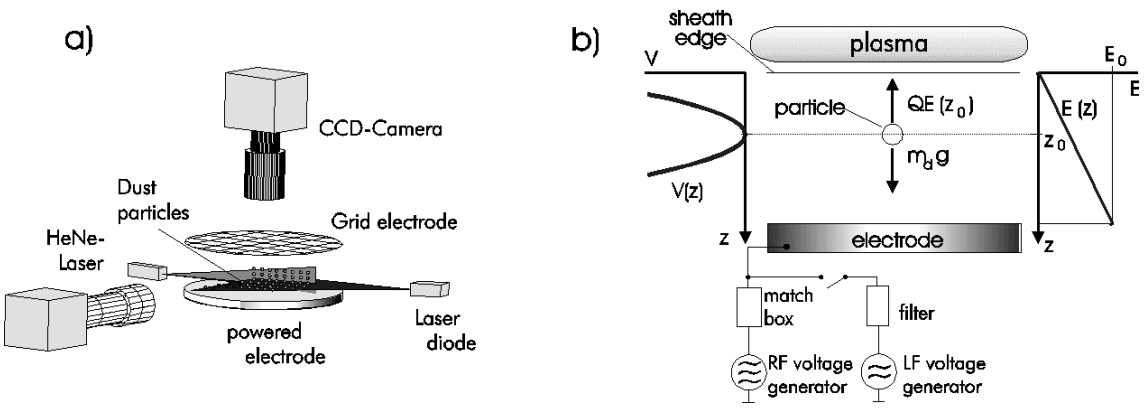

Figure 1: *Experimental setup(a) and equilibrium in the sheath(b)*

For the experiments, a parallel plate RF discharge in helium at low pressure $(3 \div 6)$Pa and RF power in the range $15 \div 25$ W was used. Monodisperse, spherical plastic particles of 9.47 and 6.17μm are immersed into the plasma. A 690nm laser diode was used to illuminate the particles trapped in the sheath. The beam was vertically expanded into a narrow sheet and the scattered light is viewed by video cameras from top and from the side. Low amplitude modulation of the RF voltage was used for exciting the particle oscillation (see Fig.1a).

Model

Variation of the electron and ion densities and currents in the sheath lead to a deviation from the linear electric field profile and to a position-dependent dust charge. This results in a non-linear effective potential well for the particle. The general equation of motion for a particle then has the form:

$$\ddot{x} + \beta\dot{x} + C_1 x + C_2 x^2 + C_3 x^3 + \ldots = F\cos(\omega t) \tag{1}$$

where β is the damping constant due to the particle friction with the neutral gas, $F\cos(\omega t)$ is the excitation force due to the RF voltage modulation. C_2 and C_3 are the nonlinear terms describing the deviation of the effective potential well from the simple parabolic form. If one sets C_2 and C_3 to zero, then the simple damped harmonic oscillation is obtained, with the frequency determined by C_1. C_2 gives the up-down assymetry of the oscillation with respect to the equilibrium position, while C_3 causes a weaker or stronger potential well compared to the parabolic one for high oscillation amplitude
Values for these nonlinear coefficients are obtained by fitting our model to the experimental data: $C_1 = 4980s^{-2}$, $C_2 = -1.5 \cdot 10^5 m^{-1}s^{-2}$ and $C_3 = -3.3 \cdot 10^8 m^{-2}s^{-2}$

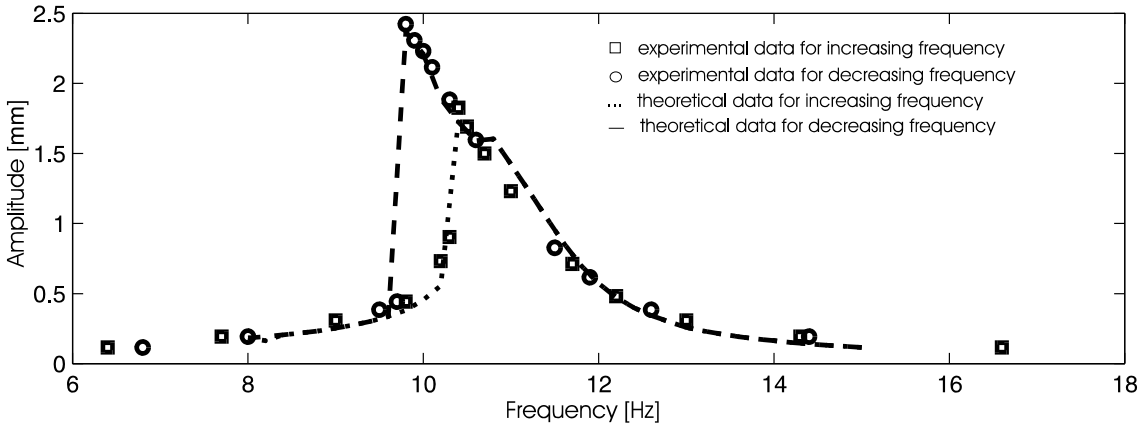

Figure 2: *Experimental data and numerical solution for the resonance curve*

Our experiments performed with particles of different size oscillating in the plasma sheath clearly yield non-linear resonance curves (see fig.2). This demonstrates that the effective potential well is not parabolic. This effect is easily observable for high oscillation amplitudes. The excitation amplitudes here used are high enough to allow the particle to reach the non-parabolic regions of the potential well. From this the electric field and the dust charge profile can be derived.

References

1. T. Trottenberg, A. Melzer, A. Piel, Plasma Sources Sci. Technol. 450 (1995)
2. Michael A. Lieberman, IEEE Transactions on Plasma Sci. Vol 16 No. 8 638 (1988)

B.2

THERMOPHORETIC AND ION DRAG FORCES ACTING ON FREE-FALLING CHARGED PARTICLES IN AN RF-DRIVEN PLASMA

C. Zafiu, A. Melzer and A. Piel

3rd International Conference on the
PHYSICS OF DUSTY PLASMAS
ICPDP-2002 Durban, South Africa

Thermophoretic and Ion Drag Forces Acting on Free-Falling Charged Particles in an RF-Driven Plasma

C. Zafiu, A. Melzer, A. Piel

Institut für Experimentelle und Angewandte Physik, Christian-Albrechts-Universität Kiel, 24098 Kiel, Germany

Abstract. The thermophoretic force and ion-drag acting on micro-particles falling through a long RF plasma has been measured here under two different experimental situations: either an unperturbed plasma characterized by its symmetric potential and temperature distribution or a plasma with an asymmetric temperature and potential profile. The dominant effect of the gravitation force is reduced here due to the dynamic equilibrium with the friction force of the particles with the neutral gas.

The reduction or even suppression of the dominant influence of the gravitation force on the complex plasma systems has allowed the study of "hidden" effects like voids in three-dimensional dust structures [1, 2, 3, 4], which occur due to smaller forces like thermophoretic force and ion drag. For typical particle diameters of $1\ldots10\mu$m, these forces are about one order of magnitude smaller than the gravitation force.

Simulation of experiments under micro-gravity [2] show that an ad-hoc enhancement of the ion drag force of at least a factor of 10 is necessary to simulate voids like those observed in experiments [1]. Therefore, quantitative measurements of these two forces are necessary in order to check or improve the theoretical calculations and simulations.

Here, experiments to measure the ion drag and thermophoresis under laboratory conditions are presented.

In our experiment, the micro-particles are dropped through a long plasma discharge. Within several centimeters, the particles reach a regime of constant vertical velocity due to the balance of the gravitation force by the friction force of the falling particles with the neutral gas.

$$m\vec{g} - m\beta\vec{y} = 0, \tag{1}$$

Thus, this experiment provides a dynamic equilibrium, thereby effectively reducing the influence of gravity.

In the following, the forces acting on the particles on the horizontal direction (see Fig. 1d) are summarized. In a discharge tube, the electric field structure is determined by the positive polarization of plasma with respect to the walls. This typically provides a linearly increasing radial electric field $E(x)$. The electric force on a particle of charge Q is then defined by

$$\vec{F}_{electric} = Q\vec{E}(x). \tag{2}$$

For the particles with a horizontal velocity, the friction force is

$$\vec{F}_{frict\_x} = m\beta\vec{x}. \tag{3}$$

The ions are accelerated towards the walls due to the same electric field $E(x)$ in the plasma and act on the negatively charged particles by the so-called ion drag [2, 5, 6]. It has two components: a direct one, which is due to the momentum transport of the ions which hit the particle surface

$$\vec{F}_{collect} = n_i m_i \vec{v}_i v_s \pi b_c^2, \tag{4}$$

and a second one, the Coulomb component,which is produced by exchange of momentum of the ions whose trajectories are bent in the electric field of the particles

$$\vec{F}_{Coulomb} = 4\pi n_i m_i \vec{v}_i v_s b_{\frac{\pi}{2}}^2 \Gamma. \tag{5}$$

Here, v_s is the mean speed of ions approaching the particle, b_c is the maximal collection impact parameter, $b_{\frac{\pi}{2}}$ is the impact parameter corresponding to a deflection angle of $\pi/2$, Γ is the Coulomb logarithm. n_i, m_i, T_i, q_i and v_i are the number density, mass, temperature, charge and drift velocity of ions, and λ_D is the Debye length.

The thermophoretic force due to a temperature gradient of the neutral gas pushes the particle to colder regions of the plasma and is given by [6]

$$\vec{F}_{thermo} = -\frac{32}{15}\frac{r_p^2}{v_{th}}\lambda\vec{\nabla}T_n, \tag{6}$$

where λ is the translation part of heat conductivity of the gas, and v_{th} is the thermal velocity of the neutral gas.

In summary, the horizontal equation of motion of the falling particles is described by

$$m\vec{\ddot{x}} = \vec{F}_{electric} + \vec{F}_{frict} + \vec{F}_{collect} + \vec{F}_{Coulomb} + \vec{F}_{thermo} \tag{7}$$

The influence of the ion drag and thermophoresis have been studied here both for a symmetric and an asymmetric temperature and potential distribution in the plasma. This has been done to establish plasma regions with opposing ion drag and thermophoretic forces .

The experiments have been performed in a long RF discharge tube (see Fig. 1a) in He at a gas pressure between 100 and 200 Pa, for plasma power between 0.8 and 2.8 W. The particles are observed at a certain level in the middle of the plasma column in the scattered light of a thin vertical laser sheet, using a high frame rate video camera. The laser stroboscopically illuminates the particles at 400 Hz. This method provides a high time resolution, even when using a low speed camera.

The particles used here are of 9.55 μm and 20.02 μm diameter and are made of Melamine Formaldehyde (MF) and Polymethylmethacrylate (PMMA) respectively.

The forces on the particles are measured here in the following way: From the particle trajectories, the acceleration and friction force (in horizontal direction) are directly

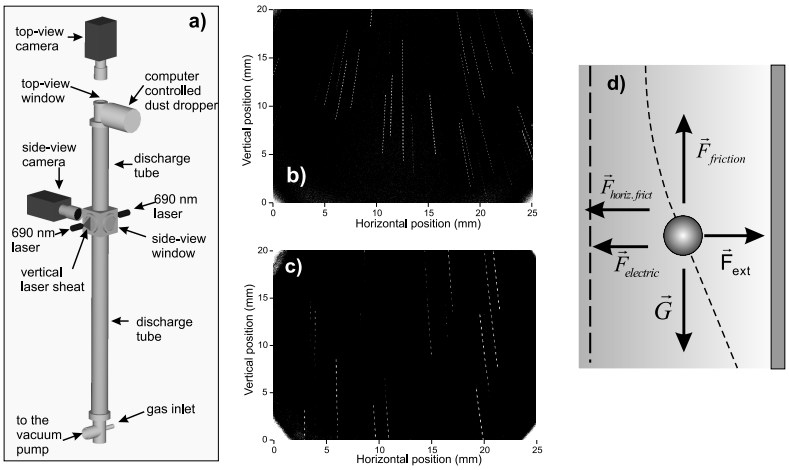

FIGURE 1. a) Scheme of the experimental setup, b) video image (symmetric temperature and potential distribution), c) video image (asymmetric temperature and potential distribution), and d) horizontal and vertical forces acting on the falling particles.

obtained. The plasma potential profile and thus the electric field distribution have been derived from probe measurements. Therefore the electric force on the particles could be determined. To measure the thermophoretic force, the temperature profiles of the neutral gas have been measured with a thermo-resistor. To evaluate the ion drag, the ion velocity has been calculated employing their mobility μ_i and the electric field structure in the plasma $v_i = \mu_i E(x)$. It must be mentioned here that the equations describing the ion drag (Eq. 4, 5) are applicable under the assumption that no ion collisions occur inside the Debye sphere, which is the case of low pressure plasmas. In our case, however, the ion mean free path is small comparable to the Debye length.

Two different experimental situations have been studied here. First, the behavior of falling particles through an unperturbed plasma, characterized by its natural radially symmetric electric potential and temperature distribution, has been analyzed. In the experiment, it can be seen that the particles move radially outward with increasing velocity (see Fig. 1b). This effect becomes stronger with increasing plasma power.

In the second case, the temperature distribution has been altered using a heat source on one of the observation windows (left side of the Fig. 1c). The probe measurements revealed that also the electric potential distribution has been perturbed in this case due to the use of large metallic parts very close to the discharge.

Fig. 2 shows the forces acting on the dust particles in the symmetric case. Therefore, we have chosen radial coordinates with the origin on the discharge axis. The radial acceleration and friction force from the radially outward moving particles are shown in Fig. 3a. Additionally, the inward electric field force is shown together with the total inward force. This total force in Fig. 3a is supposed to be balanced by the ion drag and the thermophoresis. It is seen that the sum of the measured thermophoresis and ion drag is slightly smaller than the total measured inward force. The small discrepancy between these two total forces might lie in the applicability of the ion drag equations (Eq.4,5) for our experimental conditions. For these measurements, a ten-fold increased ion drag is not compatible with our results. The same analysis has been done for the asymmetric

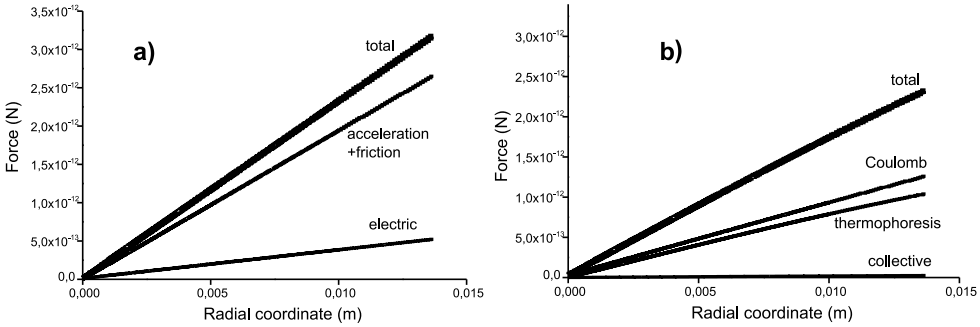

FIGURE 2. Symmetrical temperature and potential distribution case; a) measured force, from the particle trajectories analysis, taking into account the friction and the electric force, and b) theoretical force (thermophoresis and ion drag).

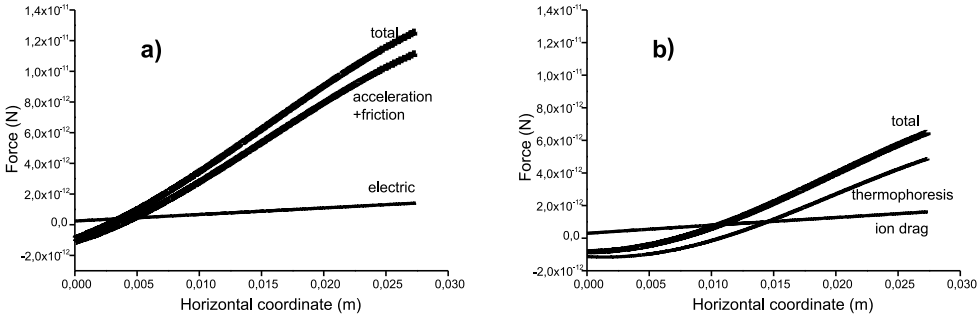

FIGURE 3. Asymmetrical temperature and potential distribution case; a) measured force, from the particle trajectories analysis, taking into account the friction and the electric force, and b) theoretical force (thermophoresis and ion drag).

experimental case. Here, also plasma regions have been observed with opposing ion drag and thermophoresis. Again, the total measured force summarizing the inward acting forces is slightly larger than the sum between the measured thermophoretic force and the ion drag. Concluding, for both cases analyzed here, the ion drag and thermophoresis have been experimentally measured, showing a quite good agreement with the theoretical predictions, and emphasizing the applicability limits of the actual models describing these two forces for our experimental conditions.

Financial assistance from INTAS (97-755) is gratefully acknowledged.

REFERENCES

1. Morfill, G. E., Thomas, H. M., Konopka, U., Rothermel, H., Zuzic, M., Ivlev, A., and Goree, J., *Phys. Rev. Lett.*, **83**, 1598–1601 (1999).
2. Akdim, M. R., and Goedheer, W. J., *Phys. Rev. E*, **65**, 015401 (2002).
3. Morfill, G., and Tsytovich, V. N., *Phys. Plasmas*, **9**, 4–16 (2002).
4. Goree, J., Morfill, G. E., Tsytovich, V. N., and Vladimirov, S. V., *Phys. Rev. E*, **59**, 7055–7067 (1999).
5. Barnes, M. S., Keller, J. H., Forster, J. C., O'Neill, J. A., and Coultas, D. K., *Phys. Rev. Lett.*, **68**, 313–316 (1992).
6. Perrin, J., Molinás-Mata, P., and Belenguer, P., *J. Phys. D: Appl. Phys.*, **27**, 2499–2507 (1994).

Acknowledgements

Prof. Dr. Alexander Piel is gratefully acknowledged for his professional and human support during all phases of this project and my stay in Kiel.

I want to bring special thanks to Dr. André Melzer who supported me in both finalizing this project and integrating me in the big "plasma family" from the Kiel University. During numerous discussions, he lead my work toward optimal results and initiated me in the research world of complex plasmas grace to his perfectionist but, at the same time, friendly style.

Prof. Dr. Urlich Stroth is gratefully acknowledged for accepting to be referee of this work.

I am very thankful to Markus Klindwoth who patiently helped me both in technical details concerning laboratory equipment or computers, and with interesting discussions. Most of all I thank him for his friendship.

My colleagues and friends from the plasma group: Nils Krause, Dr. Dietmar Block, Markus Hirt, Oliver Arp, Björn Brede, Dr. Franko Greiner, Rohwer Volker, Dr. Yoshifumi Saitou, Berndt Hipp, Thomas Trottenberg and Dr. Christian Steigies are specially acknowledged for their help, fruitful discussions and friendship. I am thankful to Mirko Ramisch for his always friendly support that gave me in managing various programming problems in LabView. Mr. W. Krüger is acknowledged for his help concerning the glass technique, filters and film deposition.

Ing. M. Brix is acknowledged for his professional contribution in designing and production of all devices and components needed for the experimental setup.

Mrs. K. Hinz, our formes secretary is gratefully acknowledged for helping me in the jungle of bureaucratic problems that I had to deal with during the first months of my stay in Kiel. For further help in similar problems, I am thankful to Mrs. M. Seeger and Mrs. S. Thiedemann.

The author acknowledges the financial support of this project by DFG under contract number Pi 185-17/1,2.

Finally I want to thank to my family, to my parents Maria and Mircea who have been always the fundamental support, even though, sometimes from far away... Most of all, I am deeply indebted to my wife Adriana who gave me the love and motivation which made possible this work.